

Institute of Mathematics with Computing Centre
UFRC RAS

As a manuscript

Lebedev Mikhail Evgenievich

**Stationary States of Bose–Einstein
Condensate in Nonlinear Lattices:
Mathematical and Numerical Study**

THESIS

submitted for academic degree of
Doctor of Philosophy in Applied Mathematics
at HSE

Academic supervisor
Alfimov Georgy Leonidovich, Ph. D.

Moscow – 2022

Contents

Introduction	3
Chapter 1. General Propositions on Regular and Singular Solutions for Stationary States Equation $u_{xx} + Q(x)u + P(x)u^3 = 0$	4
1.1. Objectives	4
1.2. Non-existence of Singular Solutions: $P(x) \geq P_0 > 0$	4
1.3. Asymptotic Behaviour at a Collapse Point: $P(x_0) < 0$	7
1.4. All Solutions Are Singular: $P(x) \leq P_0 < 0, Q(x) \leq Q_0 < 0$	11
1.5. Summary	13
Chapter 2. Stationary States Classification Within Symbolic Dynamics Framework	15
2.1. Objectives	15
2.2. Geometry of the Poincaré Map	16
2.3. Poincaré Map Domains for Piecewise Periodic Pseudopotential	24
2.4. Symbolic Dynamics: Coding of Solutions	38
2.5. Numerical Test of Existence of Coding Homeomorphism	49
2.6. Stationary Solutions of GPE with Piecewise Pseudopotential	55
2.7. Summary	58
Chapter 3. Localized Solutions of Gross-Pitaevskii Equation with Periodic Pseudopotential	59
3.1. Objectives	59
3.2. Coding of Solutions	60
3.3. Analysis of Stability	67
3.4. Summary	73
Chapter 4. Localized Solutions of Nonlinear Harmonic Oscillator	

with Periodic Pseudopotential	75
4.1. Objectives	75
4.2. Small-Amplitude Localized Solutions with Linear Counterpart . . .	80
4.3. Branches of Nonlinear Localized Solutions for Periodic Pseudopotential, $P(x) = P_0 + P_1 \cos(\Omega x)$	82
4.4. Summary	95
Appendix A. Lemma on Bounded Solutions	96
Appendix B. Solutions of Duffing Equations	100
B.1. Equation with Positive Nonlinearity	100
B.2. Equation with Negative Nonlinearity	100
Appendix C. Strips Mapping Theorems	103
Bibliography	112

Itroduction

One dimensional Gross–Pitaevskii equation (describes “cigar-shaped” condensate) takes form:

$$i\Psi_t + \Psi_{xx} + U(x)\Psi + P(x)|\Psi|^2\Psi = 0. \quad (1)$$

Here $\Psi(t, x)$ is the macroscopic wave function of the condensate, $U(x)$ corresponds to the potential of the trap holding the condensate, and $P(x)$ describes characteristic length of the atomic interactions. Function $P(x)$ is called as *pseudopotential* which is induced by spatial periodic modulation. This can be achieved in BEC by means of the Feshbach resonance controlled by magnetic or optical field [1, 2, 3]. In the nonlinear optics spatial modulation of the Kerr coefficient can be induced by inhomogeneous density of resonant nonlinearity-enhancing dopants implanted into the waveguide [4].

...

Chapter 1

General Propositions on Regular and Singular Solutions for Stationary States Equation

$$u_{xx} + Q(x)u + P(x)u^3 = 0$$

1.1. Objectives

In this chapter we formulate general statements about singular and regular solutions for the equation

$$u_{xx} + Q(x)u + P(x)u^3 = 0. \quad (1.1)$$

In general, we suppose that $Q(x), P(x) \in C^1(\mathbb{R})$ and will impose additional restrictions further when it's needed. Mainly we address two questions: (A) when do exist regular solutions of (1.1); (B) what are the conditions for the functions $Q(x)$ and $P(x)$ which can guarantee the existence of the singular solutions for equation (1.1); and (C) what is the behaviour of the collapsing solutions near the collapse point. In this chapter partial answer to the question (A) is given by the Proposition 1. On other hand Propositions 2 and 3 give a partial answer to the question (B). In particular Proposition 2 states that if the function $P(x)$ is negative at a point $x = x_0$ then there exist two one-parametric families of solutions collapsing at x_0 . Proposition 2 determines an asymptotic behaviour of these singular solutions families, which gives an answer to the question (C) for these families.

1.2. Non-existence of Singular Solutions: $P(x) \geq P_0 > 0$

This section contains a sufficient condition for non-existence of singular solutions for equation (1.1). It's given by the following proposition.

Proposition 1. *Let functions $Q(x), P(x) \in C^1(\mathbb{R})$, moreover:*

(a) $P(x) \geq P_0 > 0$, $|P'(x)| \leq \tilde{P}$;

(b) $Q(x) \geq Q_0$, $|Q'(x)| \leq \tilde{Q}$;

then solution of the Cauchy problem for equation (1.1) with arbitrary initial conditions $u(x_0) = u_0$, $u_x(x_0) = u'_0$ can be continued to the whole real axis \mathbb{R} .

Proof. By the existence and uniqueness theorem for ODE there exists an interval $[x_0; x_1)$ such that the solution of the Cauchy problem $u(x)$ for equation (1.1) with initial conditions $u(x_0) = u_0$, $u_x(x_0) = u'_0$ exists and is unique on this interval, and $u(x) \in C^2[x_0; x_1)$. Suppose that $[x_0; x_1)$ is the maximum interval for existence of $u(x)$. It means that solution of the Cauchy problem $u(x)$ cannot be continued beyond the point x_1 . Multiplying the original equation by $4u_x(x)$ and integrating it over $[x_0, x)$, $x < x_1$, we have the following relation:

$$\begin{aligned} 2u_x^2(x)) + 2Q(x)u^2(x) - 2 \int_{x_0}^x Q'(\xi)u^2(\xi)d\xi + P(x)u^4(x) - \int_{x_0}^x P'(\xi)u^4(\xi)d\xi = \\ = 2(u'_0)^2 + 2Q(x_0)u_0^2 + P(x_0)u_0^4 \equiv C. \end{aligned} \tag{1.2}$$

Omit the term $u_x^2(x) \geq 0$ in the left-hand side of the equality, and take into account the lower limits for $Q(x)$, $P(x)$ given by conditions (a), (b). Then we arrive at the following inequality:

$$2Q_0u^2(x) + P_0u^4(x) \leq C + 2 \int_{x_0}^x Q'(\xi)u^2(\xi)d\xi + \int_{x_0}^x P'(\xi)u^4(\xi)d\xi. \tag{1.3}$$

Replace the derivatives $Q'(\xi)$ and $P'(\xi)$ with their upper bounds: $Q'(\xi) \leq \tilde{Q}$, $P'(\xi) \leq \tilde{P}$, where $\tilde{Q} \geq 0$, $\tilde{P} \geq 0$. Multiplying both sides of the inequality by P_0 , we have

$$2Q_0P_0u^2(x) + P_0^2u^4(x) \leq P_0C + 2P_0\tilde{Q} \int_{x_0}^x u^2(\xi)d\xi + P_0\tilde{P} \int_{x_0}^x u^4(\xi)d\xi. \tag{1.4}$$

Let $v(x) = (P_0 u^2(x) + Q_0)^2$, $v(x) \geq 0$, substituting this into (1.4) gives

$$v(x) \leq \tilde{C} + \frac{\tilde{P}}{P_0} \int_{x_0}^x w(v(\xi)) d\xi. \quad (1.5)$$

Here $\tilde{C} = P_0 C + Q_0^2 \geq 0$, $\alpha = 2\tilde{Q}P_0/\tilde{P} \geq 0$, and $w(v)$ is defined by

$$w(v) \equiv \alpha(\sqrt{v} - Q_0) + (\sqrt{v} - Q_0)^2. \quad (1.6)$$

Consider the function

$$G(s) = \int_{s_0}^s \frac{dv}{w(v)}. \quad (1.7)$$

Here $s_0 > Q_0^2$ is an arbitrary constant, $s \geq s_0$. Since $w(v)$ is a positive and monotonically decreasing function, and the integral

$$\int_{s_0}^{+\infty} \frac{dv}{w(v)} \quad (1.8)$$

diverges, one can conclude that $G(s)$ is a positive, monotonically increasing, and unbounded function. It means that inverse function $G^{-1}(r)$ is well-defined for $r \geq 0$, increases monotonically, and is unbounded. The above-mentioned statements allow as to apply *Bihary* inequality [5, theorem 2.3.1] to (1.5). This results in the inequality

$$v(x) \leq G^{-1} \left(G(\tilde{C}) + \frac{\tilde{P}}{P_0} \int_{x_0}^x d\xi \right) = G^{-1} \left(G(\tilde{C}) \frac{\tilde{P}}{P_0} (x - x_0) \right) < \infty. \quad (1.9)$$

Inequality (1.9) is valid for all $x \in [x_0; x_1]$. It follows from (1.9) that function $v(x)$ is bounded on the whole interval $[x_0; x_1]$:

$$v(x) \leq M = G^{-1} \left(G(\tilde{C}) + \frac{\tilde{P}}{P_0} (x_1 - x_0) \right). \quad (1.10)$$

We observe that $\tilde{C} \geq Q_0^2$, moreover $\tilde{C} = Q_0^2$ only if $u_0 = u'_0 = 0$. It means that $G(s)$ is well-defined for each constant \tilde{C} corresponding to any non-zero solution

$u(x)$. The boundedness of $v(x)$ yields that solution $u(x)$ is also bounded on the segment $[x_0; x_1]$:

$$|u(x)| \leq \sqrt{\frac{\sqrt{M} - Q_0}{P_0}}, \quad x \in [x_0; x_1]. \quad (1.11)$$

Substitution of (1.11) into (1.2) gives the upper bound for the derivative $u_x(x)$ on the interval $x \in [x_0; x_1]$. Since functions $u(x)$ and $u_x(x)$ are continuous and bounded on $[x_0; x_1]$, the values $u(x_1) = u_1$ and $u_x(x_1) = u'_1$ are finite. Hence there exists a continuation of the solution to the Cauchy problem with the initial conditions $u(x_0) = u_0$, $u_x(x_0) = u'_0$ on a larger interval beyond the initial $[x_0; x_1]$. It contradicts the original assumption.

Thus we have proved that the solution can be continued for $x > x_0$. In order to prove the same statement for $x < x_0$, one can make a substitution $x \rightarrow -x$ and employ the same reasoning. \square

Corollary 1. *If the conditions (a) and (b) are satisfied not on the whole real axis \mathbb{R} , but only on some interval $[x_1; x_2]$, then a solution of the Cauchy problem for equation (1.1) with arbitrary initial conditions does not collapse at any point of the segment $[x_1; x_2]$.*

1.3. Asymptotic Behaviour at a Collapse Point: $P(x_0) < 0$

1.3.1. Asymptotic Expansions

If $P(x)$ is negative at least at one point $x_0 \in \mathbb{R}$, formal asymptotic expansions predict existence of two one-parametric families of the solutions for the equation (1.1) collapsing at this point.

Let us construct these asymptotic expansions. We suppose that $P(x_0) = -1$ (this condition can be achieved by a simple renormalisation of the independent variable), denote $\eta = x - x_0$, and assume that in the vicinity of the point $x = x_0$, the following expansions are valid:

$$Q(x) = Q_0 + Q_1\eta + Q_2\eta^2 \dots, \quad P(x) = -1 + P_1\eta + P_2\eta^2 + \dots \quad (1.12)$$

Substituting these expansions into (1.1), we have

$$u_{\eta\eta} + (Q_0 + Q_1\eta + Q_2\eta^2 \dots)u + (-1 + P_1\eta + P_2\eta^2 + \dots)u^3 = 0. \quad (1.13)$$

If a solution $u(\eta)$ of equation (1.13) collapses at the point $\eta = 0$ then $u(\eta) \rightarrow \pm\infty$, when $\eta \rightarrow 0$. Let η approach zero *from the right*, $\eta > 0$. The change $v(\eta) = \eta u(\eta)$, $\eta = e^{-t}$ gives

$$v_{tt} + 3v_t + 2v + e^{-2t}Q(t)v + P(t)v^3 = 0. \quad (1.14)$$

Determine the main term of the expansion by balancing $2v$ and $-v^3$ terms. We have

$$V_0(t) = \pm\sqrt{2}. \quad (1.15)$$

Now let's define the first order term $V_1(t)$, $v(t) = \pm\sqrt{2} + V_1(t) + o(V_1(t))$. Substituting the last expression into (1.14), taking into account the expansions for the functions $Q(t)$, $P(t)$, and omitting the terms of order higher than e^{-t} , we obtain

$$V_{1,tt} + 3V_{1,t} - 4V_1 = \mp 2\sqrt{2}e^{-t}, \quad (1.16)$$

that gives $V_1(t) = \pm\frac{\sqrt{2}}{3}e^{-t}$. Second, third, and forth order terms V_n , $n = 2, 3, 4$, can be found in a similar manner. For each term the corresponding equation takes form:

$$V_{n,tt} + 3V_{n,t} - 4V_n = C_n e^{-nt}. \quad (1.17)$$

For $n = 2, 3$ solutions of equation (1.17) are of the form $V_n \sim e^{-nt}$. However in the case $n = 4$ the exponent degree in the right hand side coincides with one of the roots of the characteristic polynomial for the differential operator in the left-hand side. In this case solution of equation (1.17) must be chosen in the form $Ce^{-4t} - A_3te^{-4t}$. Here C is an arbitrary constant, while A_3 can be determined uniquely from the coefficients of the series expansions for $Q(t)$, $P(t)$. If constant C is fixed, at the further steps of this procedure the corresponding equations are uniquely solvable. One can note that switching of $+$ to $-$ in the expression (1.15) leads to the corresponding change

of signs for all coefficients A_n , $n = 0, 1, \dots$, that is natural due to the invariance of equation (1.1) with respect to the change $u \rightarrow -u$. We have

$$\pm v(t) = \sqrt{2} + A_0 e^{-t} + A_1 e^{-2t} + A_2 e^{-3t} + A_3 \cdot (-t) \cdot e^{-4t} + C e^{-4t} + \dots \quad (1.18)$$

Explicit expressions for A_0, \dots, A_3 are:

$$A_0 = \frac{\sqrt{2}}{3} P_1; \quad (1.19)$$

$$A_1 = \frac{\sqrt{2}}{3} P_2 + \frac{\sqrt{2}}{6} Q_0 + \frac{2\sqrt{2}}{9} P_1^2; \quad (1.20)$$

$$A_2 = \frac{2\sqrt{2}}{3} P_2 P_1 + \frac{7\sqrt{2}}{27} P_1^3 + \frac{\sqrt{2}}{6} Q_0 P_1 + \frac{\sqrt{2}}{4} Q_1 + \frac{\sqrt{2}}{2} P_3; \quad (1.21)$$

$$A_3 = -\frac{\sqrt{2}}{6} Q_1 P_1 - \frac{\sqrt{2}}{5} Q_2 - \frac{32\sqrt{2}}{45} P_2 P_1^2 - \frac{3\sqrt{2}}{5} P_3 P_1 - \quad (1.22)$$

$$-\frac{2\sqrt{2}}{15} P_2 Q_0 - \frac{2\sqrt{2}}{15} Q_0 P_1^2 - \frac{2\sqrt{2}}{5} P_4 - \frac{28\sqrt{2}}{135} P_1^4 - \frac{4\sqrt{2}}{15} P_2^2. \quad (1.23)$$

In the other case when $\eta \rightarrow 0$ from the left, $\eta < 0$, similar expansions can be constructed by mean of changes of variables $v(\eta) = \eta u(\eta)$, $\eta = -e^{-t}$. Expressions for the coefficient A_n remain the same as for $\eta > 0$.

Finally we get an asymptotic expansion for the original solution $u(x)$ for $x \rightarrow x_0 \pm 0$:

$$\pm u(x) = \frac{\sqrt{2}}{\eta} + A_0 + A_1 \eta + A_2 \eta^2 + A_3 \eta^3 \ln |\eta| + C \eta^3 + A_4 \eta^4 \ln |\eta| + \dots \quad (1.24)$$

Here $\eta = x - x_0$, A_0, \dots, A_3 are determined by equations (1.19)-(1.23), and all other coefficients A_n , $n > 3$ can be expressed through Q_n , P_n and arbitrary constant C .

Summarizing all the above mentioned, one can say that asymptotic expansion (1.24) *predicts the existence* of two one-parametric families of solutions collapsing at the point x_0 . These families are connected by the symmetry $u \rightarrow -u$. When $x \rightarrow x_0$, the solutions from one of these families tend to $+\infty$, while the solutions from another family tend to $-\infty$ correspondingly.

1.3.2. Existence of One-Parametric Families of Collapsing Solutions

Strictly speaking, formal asymptotic expansions (1.24) do not imply the existence of one-parametric families of solutions collapsing at point x_0 . However, the following rigorous statement holds.

Proposition 2. *Let Ω be a neighbourhood of the point x_0 , $Q(x) \in C^2(\Omega)$ and $P(x) \in C^4(\Omega)$. Then there exist two C^1 -smooth one-parametric families of solutions for equation (1.1) corresponding to expansions (1.24), collapsing at the point $x = x_0$ (while approaching from the left, $x < x_0$), and connected by a symmetry $u \rightarrow -u$. Each of these families can be parametrized by a free variable $C \in \mathbb{R}$ from the expansions (1.24).*

Proof. Due to the condition of proposition the following expansions are valid:

$$Q(x) = Q_0 + Q_1\eta + Q_2\eta^2 + \tilde{Q}(\eta)\eta^3; \quad (1.25)$$

$$P(x) = -1 + P_1\eta + P_2\eta^2 + P_3\eta^3 + P_4\eta^4 + \tilde{P}(\eta)\eta^5. \quad (1.26)$$

Here $\eta = x - x_0$, and $\tilde{Q}, \tilde{P} \in C(\Omega)$. To prove existence of the family that corresponds to the + sign in (1.24) we introduce the function $z(\eta)$ as follows:

$$u(x) = \frac{\sqrt{2}}{\eta} + A_0 + A_1\eta + A_2\eta^2 + A_3\eta^3 \ln(-\eta) + z(\eta)\eta^3, \quad (1.27)$$

($z(\eta)$ is a new unknown function). Coefficients A_0, \dots, A_3 are chosen accordingly to the expressions (1.19)-(1.23), so the coefficients at the terms η^{-2} , η^{-1} , η^0 , and η vanish. It's easy to check that direct substitution of the (1.27) into (1.1) yields

$$z_{\eta\eta} + \frac{6}{\eta}z_\eta + g(\eta, z) = 0, \quad (1.28)$$

where $g(\eta, z)$ is a third order polynomial with respect to z , and $g(\eta, z) \sim \frac{\ln(-\eta)}{\eta}$ when $\eta \rightarrow -0$ and z is fixed. The change of variable $\eta = -e^{-t}$ maps the point $\eta = 0$ into $t = +\infty$, and transforms equation (1.28) into

$$z_{tt} - 5z_t - f(t, z) = 0. \quad (1.29)$$

Here $f(t, z) \sim te^{-t}$ while $t \rightarrow +\infty$. Properties of the function $f(t, z)$ allows us to apply *Lemma on Bounded Solutions* from Appendix A to equation (1.29). This lemma states that for $t \rightarrow +\infty$ all bounded solutions of equation (1.29) tend to some constant C when $t \rightarrow +\infty$, moreover for each $C \in \mathbb{R}$ there exists a unique solution that approaches to that constant asymptotically while $t \rightarrow +\infty$. Furthermore these solutions form a C^1 -smooth family. Finally, we can return to previous equation (1.28), and then to (1.1) to get the initial statement of the proposition. The existence of the second family of solutions corresponding to the sign “ $-$ ” in (1.24) follows from the invariance of equation (1.1) under the symmetry $u \rightarrow -u$. \square

Similar one-parametric families of collapsing solutions exist from the right side of the point $x = x_0$. The corresponding proof can be performed in the same way.

1.4. All Solutions Are Singular: $P(x) \leq P_0 < 0, Q(x) \leq Q_0 < 0$

It turns out that under some assumptions all non-trivial solutions of the equation (1.1) are singular.

Proposition 3. *Let for $x \in \mathbb{R}$ the conditions $P(x) \leq P_0 < 0, Q(x) \leq Q_0 < 0$ take place. Then all solutions of equation (1.1) are singular except for the zero one.*

To prove this proposition we prove the following auxiliary lemma first.

Lemma 1. *Let $p, q > 0$ are real constants, then all solutions of equation*

$$v_{xx} - qv - pv^3 = 0, \quad (1.30)$$

are singular except for the zero one.

Proof. The solution of the Cauchy problem for equation (1.30) with initial conditions $v(x_0) = v_0, v_x(x_0) = v'_0$ can be written in an implicit form as follows:

$$\pm \int_{v_0}^v \frac{d\xi}{\sqrt{C + q\xi^2 + \frac{p}{2}\xi^4}} = x - x_0; \quad C \equiv (v'_0)^2 - qv_0^2 - \frac{p}{2}v_0^4. \quad (1.31)$$

Choice of the sign in the left hand-side depends on the initial conditions and the value of x . Integral in the left hand-side of the equality (1.31) converges when $v \rightarrow \infty$, and hence there exist a value x^* ,

$$x^* = x_0 \int_{v_0}^{\infty} \frac{d\xi}{\sqrt{C + q\xi^2 + \frac{p}{2}\xi^4}}, \quad (1.32)$$

such that $v(x)$ goes to infinity while x approaches to the x^* . So a solution $v(x)$ with arbitrary non-zero initial conditions is singular, lemma is proved. \square

Now we can prove the Proposition 3.

Proof of the Proposition 3. We use a so-called *Comparison Lemma* from [6, Appendix C]. Consider the equation

$$v_{xx} + Q_0 v + P_0 v^3 = 0. \quad (1.33)$$

We introduce the notations

$$g(x, \xi) = -Q(x)\xi - P(x)\xi^3; \quad (1.34)$$

$$f(x, \xi) = f(\xi) = -Q_0\xi - P_0\xi^3. \quad (1.35)$$

Now we apply Comparison Lemma to the following pair of equations:

$$u_{xx} = g(x, u); \quad (1.36)$$

$$v_{xx} = f(x, v). \quad (1.37)$$

In the domain $D_+ = \{x \in \mathbb{R}, \xi \in (0; +\infty)\}$ we have $f(x, \xi) \leq g(x, \xi)$. Let $\tilde{u}(x)$ be a solution of the Cauchy problem for equation (1.36) with initial conditions $u(x_0) = u_0$, $u_x(x_0) = u'_0$. Chose the initial conditions for the Cauchy problem for equation (1.37) as follows: $v(x_0) = u(x_0) = u_0$, $v_x(x_0) = u_x(x_0) = u'_0$; let $\tilde{v}(x)$ be a solution for that problem. Let $u_0 > 0$, then one of the two cases takes place.

- (i) $u'_0 \geq 0$. Function $\tilde{v}(x)$ increases monotonically; this fact can be easily established from the phase portrait of equation (1.37). Solution $\tilde{u}(x)$ bounds

the solution $\tilde{v}(x)$ from above. But $\tilde{v}(x)$ is singular. Then it follows from Comparison Lemma that solution $\tilde{u}(x)$ is also singular.

- (ii) $u'_0 < 0$. We make a change of variable $\tilde{x} = -x$. In that case solution $\tilde{v}(\tilde{x})$ also increases monotonically, and since $\tilde{u}(\tilde{x})$ limits $\tilde{v}(\tilde{x})$ from above, $\tilde{u}(\tilde{x})$ is singular by Comparison Lemma, hence $\tilde{u}(x)$ is also singular.

Similarly in the domain $D_- = \{x \in \mathbb{R}, \xi \in (-\infty; 0)\}$, the inequality $f(x, \xi) \geq g(x, \xi)$ holds. One can prove in the same manner that in the domain D_- solution $u(x)$ is also singular. \square

1.5. Summary

Our main findings on regular and singular solutions for the stationary states equation (1.1) are summarised in Table 1.1. Our further findings are focused on the case when $P(x)$ changes its sign. In the next chapter we describe a so-called *method of excluding of singular solutions* which allows us to classify all regular solutions of equation (1.1) within the symbolic dynamics framework.

$P(x)$	$Q(x)$	
$P(x) > 0$	—	All the solutions can be continued to the whole real line, singular solutions do not exist (Proposition 1).
$P(x) < 0$ at least at one point $x = x_0$	—	There exists a pair of one-parametrical families of solutions collapsing at point $x = x_0$ and related by the symmetry $u \rightarrow -u$ (Proposition 2).
$P(x) < 0$	$Q(x) < 0$	All solutions are singular except for the zero one (Proposition 3).
$P(x)$ changes sign along \mathbb{R}	—	Singular solutions are generic. That fact allows to apply the so-called <i>method of excluding of singular solutions</i> and classify all regular solutions in terms of symbolic dynamics. We describe this method and its application in Chapter 2.

Table 1.1. Summary of the results for the Chapter 1. The results of this Chapter were published in [7].

Chapter 2

Stationary States Classification Within Symbolic Dynamics Framework

2.1. Objectives

In this chapter we describe an approach that will be used in what follows to classify the stationary states of one-dimensional GPE that are described by the equation,

$$u_{xx} + Q(x)u + P(x)u^3 = 0. \quad (2.1)$$

Here and in what follows we assume $Q(x)$, $P(x)$ to be periodic functions of the same period L : $Q(x+L) = Q(x)$, $P(x+L) = P(x)$. We also assume functions $Q(x)$, $P(x)$ to be piecewise continuously differentiable. That allows us to split the whole real axis \mathbb{R} into separate intervals where the corresponding Cauchy problem is correctly defined and a solution exists and is unique for any initial conditions within each such interval.

Our classification approach is based on the technique proposed in the paper [8]. In [8] authors show that presence of a large number of families of singular solutions allows to classify all remaining bounded (i.e. non-singular) solutions within a symbolic dynamics framework. That leads us to another important requirement: function $P(x)$ must *changes its sign along the period L* . As we saw in the previous chapter such fact guarantees the existence of singular solution families that in its turn is a base of the technique and makes the announced approach even possible.

The goal of this chapter is to provide a framework for stationary states classification and point out restrictions for its application. The main idea is the following. We define a Poincaré map \mathcal{P} for equation (2.1). Since function $P(x)$ changes its sing, Poincaré map \mathcal{P} and an inverse map \mathcal{P}^{-1} cannot be defined on the whole plane of initial data, instead they are defined on some subset of initial data plane. Studying

the domains of maps \mathcal{P} , \mathcal{P}^{-1} is crucial for the proposed approach. We determine conditions which allow to conclude that Poincaré map is a kind of the *horseshoe map* [9, Chapter 5]. If these conditions are met we can conclude that there exists one-to-one correspondence between all bounded solution of equation (2.1) and the points of fractal set that is invariant with respect to action of \mathcal{P} . That is what we call *singular solution elimination method*.

The presence of the horseshoe map structure allows us to relate uniquely each bounded solution with a bi-infinite sequence of symbols of some alphabet (finite or even infinite). This correspondence is bijective. We refer to the resulting bi-infinite sequence as a *solution code* and the overall process as the *coding of solutions*. Such coding, if possible, may provide a complete picture of the bounded solutions for equation (2.1) that can be highly demanded in different physical applications which involve Gross–Pitaevskii equation with both periodic potential and periodic pseudopotential. During this part of the study we follow the approach that goes back to 60-70-es, the prominent works of L. P. Shilnikov [10] and V. M. Alekseev [11]. In the seminal papers the symbolic dynamics approach was applied for description of behaviour of trajectories near a homoclinic loop and for three-body problem. In this chapter, the horseshoe dynamics approach is used for the mapping of Poincaré map domains that is a new application of this theory.

2.2. Geometry of the Poincaré Map

First of all let's introduce several definitions.

2.2.1. Poincaré Map

Since we consider functions $Q(x)$, $P(x)$ to be L -periodic let's introduce the Poincaré map associated with the period L of the equation (2.1). Define the Poincaré

map $\mathcal{P} : \mathbb{R}^2 \rightarrow \mathbb{R}^2$ in the following manner:

$$\mathcal{P} \begin{pmatrix} u_0 \\ u'_0 \end{pmatrix} = \begin{pmatrix} u_L \\ u'_L \end{pmatrix}, \quad (2.2)$$

where $u_L = u(L)$, $u'_L = u'(L)$, and $u(x)$ is a solution of equation (2.1) with initial conditions $u(0) = u_0$, $u'(0) = u'_0$. In the plane (u, u') Poincaré map is an *area-preserving diffeomorphism*. Due to presence of singular solutions, Poincaré map \mathcal{P} and its inverse \mathcal{P}^{-1} may be defined not on the whole plane (u, u') . Denote by \mathcal{U}_L^+ the domain of the map \mathcal{P} , and denote by \mathcal{U}_L^- the domain of the map \mathcal{P}^{-1} correspondingly. Also define a set \mathcal{U}_L as an intersection of the two above mentioned sets: $\mathcal{U}_L = \mathcal{U}_L^+ \cap \mathcal{U}_L^-$.

It follows from the definitions of \mathcal{U}_L^\pm that $\mathcal{P}(\mathcal{U}_L^+) = \mathcal{U}_L^-$. Indeed any point $\mathbf{p} \in \mathcal{U}_L^+$ has \mathcal{P} -image \mathbf{q} . Then \mathbf{q} has \mathcal{P} -pre-image, therefore $\mathbf{q} \in \mathcal{U}_L^-$. On the other hand if $\mathbf{q} \in \mathcal{U}_L^-$ then \mathbf{q} has \mathcal{P} -pre-image \mathbf{p} . Therefore \mathbf{p} has \mathcal{P} -image and hence $\mathbf{p} \in \mathcal{U}_L^+$. Inverse statement $\mathcal{P}^{-1}(\mathcal{U}_L^-) = \mathcal{U}_L^+$ is also valid.

We also note here that symmetry in equation (2.1) naturally produces symmetry in \mathcal{U}_L^\pm sets. For example we can prove the following important statement.

Proposition 4. *Let functions $Q(x)$, $P(x)$ are even, then*

$$\mathcal{P}(\mathcal{U}_L^+) = I(\mathcal{U}_L^+); \quad (2.3)$$

$$\mathcal{P}^{-1}(\mathcal{U}_L^-) = I(\mathcal{U}_L^-), \quad (2.4)$$

where map I is a reflection with respect to the u' axis.

Proof. Let's prove statement (2.3). Consider a point $\mathbf{q} \in \mathcal{P}(\mathcal{U}_L^+)$. By definition of \mathcal{U}_L^+ , there is a point $\mathbf{p} = (u_0, u'_0) \in \mathcal{U}_L^+$, such that there exists a solution $u(x)$ of (2.1) with initial conditions $u(0) = u_0$, $u'(0) = u'_0$, and $\mathbf{q} = (u(L), u'(L))$. Denote by $\tilde{\mathbf{p}}$ a reflection $I(\mathbf{p})$, $\tilde{\mathbf{p}} = (-u_0, u'_0)$. Since functions $Q(x)$, $P(x)$ are even, Eq. (2.1) is invariant with respect to the transformation $\tilde{u} = -u$, $\tilde{x} = -x$. It means that $\tilde{u}(\tilde{x}) = -u(-x)$ is also a solution of (2.1) with initial conditions $\tilde{u}(0) = -u_0$,

$\tilde{u}'(0) = u'_0$. Then $\tilde{u}(-L) = -u(L) = -u_L$ and $\tilde{u}'(-L) = u'(L) = u'_L$. Denote $\tilde{\mathbf{q}} = (\tilde{u}(-L), \tilde{u}'(-L))$. By definition of \mathcal{P} map, $\tilde{\mathbf{q}} = \mathcal{P}^{-1}(\tilde{\mathbf{p}})$ and hence $\tilde{\mathbf{q}} \in \mathcal{U}_L^+$. On the other hand $\tilde{\mathbf{q}} = (-u_L, u'_L) = I(\mathbf{q})$. Finally from $I(\mathbf{q}) \in \mathcal{U}_L^+$ we get $\mathbf{q} \in I(\mathcal{U}_L^+)$. It's also straightforward to check the inverse statement $\mathbf{q} \in I(\mathcal{U}_L^+) \Rightarrow \mathbf{q} \in \mathcal{P}(\mathcal{U}_L^+)$ and prove the equality (2.3). Statement (2.4) can be proven in an identical manner. \square

If the conditions of Proposition 4 are met one can conclude that $I(\mathcal{U}_L^+) = \mathcal{U}_L^-$ and $I(\mathcal{U}_L^-) = \mathcal{U}_L^+$, so the above mentioned sets are connected with each other with a reflection with respect to the u' axis.

Definition 1. Define an **orbit** as a sequence of points $\{\mathbf{p}_n\}$, $\mathbf{p}_n \in \mathbb{R}^2$ such that $\mathcal{P}(\mathbf{p}_n) = \mathbf{p}_{n+1}$.

Let \mathbf{p}_0 be a starting point. Since \mathcal{P} is defined only on the \mathcal{U}_L^+ set, the next point \mathbf{p}_1 of the orbit exists only if $\mathbf{p}_0 \in \mathcal{U}_L^+$. Moreover for $n > 0$ points \mathbf{p}_n are consecutive \mathcal{P} -iterations of the initial point \mathbf{p}_0 . If at k -th iteration $\mathcal{P}^k(\mathbf{p}_0)$ leaves \mathcal{U}_L^+ then the orbit cannot be defined for $n > k$. Similarly for $n < 0$ points \mathbf{p}_n are consecutive \mathcal{P}^{-1} -iterations of \mathbf{p}_0 . Since the \mathcal{P}^{-1} map defined only on \mathcal{U}_L^- the iterations may stop after a finite number of steps. As a consequence not all orbits are bi-infinite. But bi-infinite orbits exist. For example one can easily specify the bi-infinite orbit of zero points that trivially satisfies the equation (2.1) and corresponds to its zero solution $u(x) \equiv 0$.

Another interesting observation comes from Proposition 1. If the function $P(x) > 0$ for all $x \in \mathbb{R}$ then all the orbits for the equation (2.1) are bi-infinite. From that point of view the case when $P(x)$ changes its sign becomes interesting. According to Proposition 2 points x where $P(x) < 0$ originate families of collapsing solutions. Such families at their turn sift the set of bi-infinite orbits.

2.2.2. Island Set

Definition 2. Let $\gamma > 0$ be fixed. A continuous function $f(x) : \Delta \rightarrow \mathbb{R}^2$, $\Delta = [a, b]$ is called a **γ -Lipschitz function** if $\forall x_1, x_2 \in \Delta$ the following inequality holds:

$$|f(x_1) - f(x_2)| \leq \gamma|x_1 - x_2|. \quad (2.5)$$

Definition 3. We call **island** an open curvilinear quadrangle $D \subset \mathbb{R}^2$ on the plane (u, u') formed by two pairs of nonintersecting monotonic curves α^\pm, β^\pm , moreover:

- curves α^\pm are graphs of monotonic γ -Lipschitz functions $u' = h_\pm(u)$, and a solution of equation (2.1) with initial conditions $(u_0, u'_0) \in \alpha^\pm$ collapses at the point $x = -L$;
- curves β^\pm are graphs of monotonic γ -Lipschitz functions $u = v_\pm(u')$, and a solution of equation (2.1) with initial conditions $(u_0, u'_0) \in \beta^\pm$ collapses at the point $x = +L$;
- if the functions $h_\pm(u)$ are increasing then $v_\pm(u')$ are decreasing, and vice versa, if functions $h_\pm(u)$ are decreasing then $v_\pm(u')$ are increasing respectively.

Remark 1. For convenience hereinafter by monotonically increasing / decreasing function we mean a function that satisfy non-strict inequalities. We call function $f(x)$ monotonically increasing if for $x_1 < x_2$, $f(x_1) \leq f(x_2)$, and monotonically decreasing if $f(x_1) \geq f(x_2)$. We also say that monotonicity type coincides for functions $f(x)$ and $g(x)$ if both $f(x)$ and $g(x)$ are increasing or decreasing functions simultaneously.

To emphasise the fact that Lipschitz constant γ must be predefined we also refer to the island as **γ -island**. We also say that points from the island boundaries are mapped to infinity by \mathcal{P} (β^\pm boundaries) or \mathcal{P}^{-1} (α^\pm boundaries), since the corresponding solution to the Cauchy problem with initial conditions in that points collapse exactly in the points $x = \pm L$.

Remark 2. If D is a γ_1 -island and $\gamma_2 > \gamma_1$ then D also is a γ_2 -island.

In our definition of island we explicitly specify its connection with initial equation (2.1) and collapses of its solutions. Further we'll see that such connection naturally comes from the dynamics of the \mathcal{P} map for equation of such type.

Remark 3. Solution of Cauchy problem for the initial conditions at the intersections of the α^\pm, β^\pm curves collapse both at $x = +L$ and $x = -L$ points.

Definition 4. Let S be a finite or a countable set of indices. Define **island set** as a set $\mathcal{D} = \bigcup_{i \in S} D_i$ that is finite or countable union of disjoint islands.

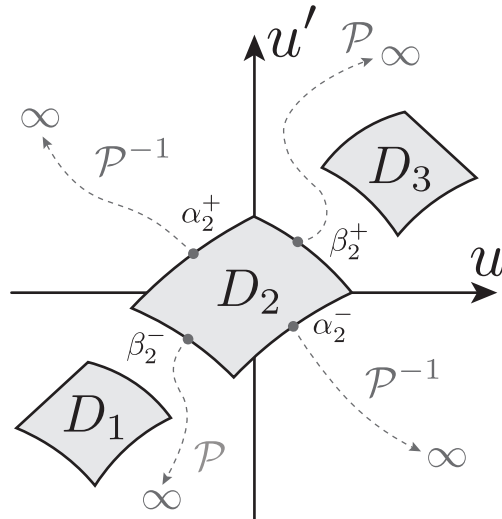


Figure 2.1. Hypothetical example of an island set $\mathcal{D} = \bigcup_{i \in \{1,2,3\}} D_i$ on a plane of initial conditions for equation (2.1). Boundaries of each component are mapped to the infinity by the \mathcal{P} and \mathcal{P}^{-1} maps (i.e. the corresponding solution of Cauchy problem collapses at $x = L$ and $x = -L$ respectively).

2.2.3. Curves and Strips

Move on to the definition of h,v-curves and h,v-strips.

Definition 5. Let D be an island bounded by curves α^\pm, β^\pm . Consider a curve α that connects the opposite sides β^\pm of the island D . We call such curve as **h-curve** (or h_γ -curve) if it represents a graph of a monotonic γ -Lipschitz function $u' = h(u)$

and its monotonicity type coincides with the functions $u' = h_{\pm}(u)$ that correspond to the α^{\pm} boundaries of the island D . We also call **h-strip** (or h_{γ} -strip) an open subset of the island D bounded by two h_{γ} -curves.

Remark 4. We say that h -curve α is increasing / decreasing if it's a graph of increasing / decreasing function $u' = f(u)$.

Definition 6. Similarly consider a curve β that connects opposite sides α^{\pm} of an island D . We call it as **v-curve** (or v_{γ} -curve) if it represents a graph of a monotonic γ -Lipschitz function $u = v(u')$ and its monotonicity type coincide with the functions $u = v_{\pm}(u')$ that correspond to the β^{\pm} boundaries of the island D . Also we call **v-strip** (or v_{γ} -strip) an open subset of the island D bounded by two v_{γ} -curves.

Remark 5. We say that a v -curve β is increasing / decreasing if it's a graph of increasing / decreasing function $u = f(u')$.

Remark 6. Island by itself represents a limit case of the h and v strips simultaneously.

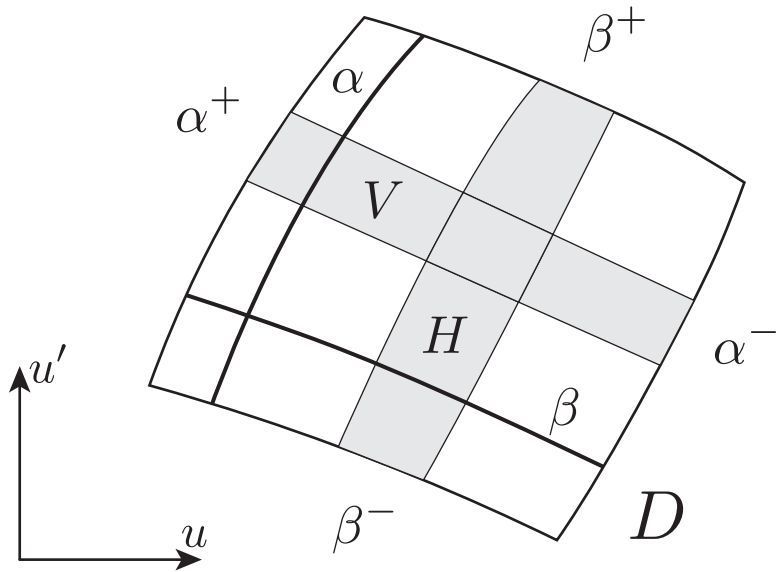


Figure 2.2. An island D bounded by curves $\alpha^{\pm}, \beta^{\pm}$; h-curve α , v-curve β , and two strips: h-strip H and v-strip V .

All the above introduced definitions are illustrated in Figures 2.1 and 2.2. At last let's define one additional property of island set along with \mathcal{P} , \mathcal{P}^{-1} maps.

Definition 7. Let \mathcal{D} be an island set that is a domain for both \mathcal{P} and \mathcal{P}^{-1} maps. Consider two islands $D_1, D_2 \in \mathcal{D}$. We call the island D_2 **forward-reachable** from the island D_1 if for any h-curve $\alpha \in D_1$ with endpoints lying on the opposite boundaries β_1^\pm of the island D_1 the intersection $\mathcal{P}(\alpha) \cap D_2$ is not empty. On the other hand we call the island D_2 **backward-reachable** from the island D_1 if for any v-curve $\beta \in D_1$ with endpoints lying on the opposite boundaries α_1^\pm of the island D_1 the intersection $\mathcal{P}^{-1}(\beta) \cap D_2$ is not empty. Finally we call the island D_2 **reachable** from the D_1 if it satisfies both forward and backward reachability.

Remark 7. If an island D_2 is forward-reachable from D_1 then D_1 is backward-reachable from D_2 and vice versa.

Definition 8. We call an island set $\mathcal{D} = \bigcup_{i \in S} D_i$ **complete** if for any i, j island D_i is reachable from D_j .

2.2.4. Thickness of Strips

Next we'll also need a definition of the strips thickness. Let an h-strip H lie inside an island D and is bounded by h-curves α^+ and α^- . Consider graphs of these curves as functions of u : $u' = h_\pm(u)$. By definition, $h_\pm(u)$ are γ -Lipschitz functions. Denote their domains by Δ^\pm . Due to the geometric properties of an island, domains Δ^\pm do not coincide except the case when the opposite boundaries of the island D are vertical straight lines. Let $\Delta^+ = [u_0^+; u_1^+]$, $\Delta^- = [u_0^-; u_1^-]$, consider new domain $\Delta = \Delta^+ \cup \Delta^-$ and define functions $\tilde{h}_\pm(u)$ on Δ as follows:

$$\tilde{h}_\pm(u) = \begin{cases} h_\pm(u_0^\pm) & u < u_0^\pm; \\ h_\pm(u) & u \in \Delta^\pm; \\ h_\pm(u_1^\pm) & u > u_1^\pm. \end{cases} \quad (2.6)$$

Since h_\pm are γ -Lipschitz functions the new functions \tilde{h}_\pm are also γ -Lipschitz on the whole domain Δ . Denote by $\tilde{\alpha}^\pm$ the curves that are the graphs of $\tilde{h}_\pm(u)$.

Definition 9. By **thickness** of an h-strip H , denoted $d_h(H)$, we mean the distance between curves $\tilde{\alpha}^\pm$ in C-norm, i.e.

$$d_h(H) = d(\tilde{\alpha}^+, \tilde{\alpha}^-) = \max_{u \in \Delta} |\tilde{h}_+(u) - \tilde{h}_-(u)|. \quad (2.7)$$

Remark 8. For two h-strips H_1, H_2 the following statement is valid: $H_2 \subseteq H_1 \Rightarrow \Delta_2 \subseteq \Delta_1$ and $d_h(H_2) \leq d_h(H_1)$.

Definition 10. Let maximum of the expression (2.7) be reached at point u_* , i.e.

$$u_* = \arg \max_{u \in \Delta} |\tilde{h}_+(u) - \tilde{h}_-(u)|. \quad (2.8)$$

We call h-strip H **well-measurable** if $u_* \in \Delta^+ \cap \Delta^-$.

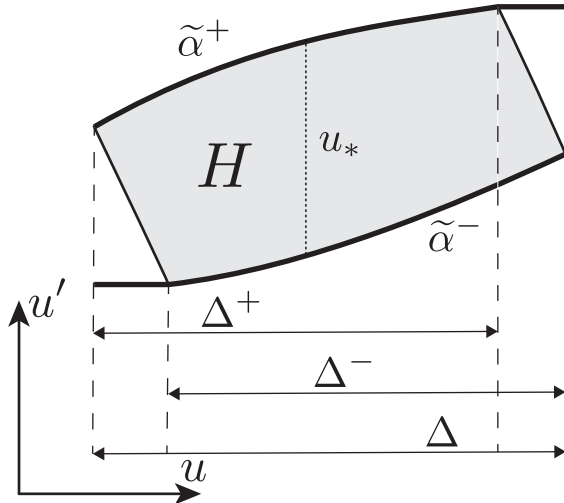


Figure 2.3. An illustration to the definition of an h-strip thickness. Strip H is *well-measurable* in a sense of Definition 10. Curves $\tilde{\alpha}^\pm$ are continuations of the initial h-strip borders to the whole Δ ; u_* is a point of maximum of the expression (2.7).

Proposition 5. For h-strip H the following statement is valid:

$$\Delta^+ \cap \Delta^- \neq \emptyset \Rightarrow u_* \in \Delta^+ \cap \Delta^-, \quad (2.9)$$

i.e. h-strip is well-measurable if domains of its border functions have at least one common point.

Proof. The statement immediately follows from the monotonicity of the h-strip borders α^+ and α^- . □

In a similar way we define thickness of v-strips. Let an v-strip V lie inside an island D and is bounded by v-curves β^+ and β^- . Consider this curves as a functions of u' : $u = v_{\pm}(u')$. Denote domains of these functions by Δ^{\pm} . Continue functions $v_{\pm}(u')$ to the whole interval $\Delta = \Delta^+ \cap \Delta^-$ in the same way as for h-strips, see (2.6), and introduce new functions $\tilde{v}_{\pm}(u')$ and curves $\tilde{\beta}^{\pm}$.

Definition 11. *By **thickness** of an v-strip V , denoted $d_v(V)$, we mean the distance between curves $\tilde{\beta}^{\pm}$ in C-norm, i.e.*

$$d_v(V) = d(\tilde{\beta}^+, \tilde{\beta}^-) = \max_{u' \in \Delta} |\tilde{v}_+(u') - \tilde{v}_-(u')|. \quad (2.10)$$

The definition of *well-measurable* v-strip is introduced in a same way. Remark 8 and Proposition 5 can be also written for v-strips. Note that thickness of h-strip is measured in vertical direction, and thickness of v-strip is measured in horizontal direction. If a strip is well-measurable then its thickness is measured in a direction along the straight line that connects points from the opposite side of the strip.

2.3. Poincaré Map Domains for Piecewise Periodic Pseudopotential

Let's demonstrate how the definitions introduced above work all together. For that purpose consider equation (2.1) with $Q(x) \equiv -1$ and periodic piecewise constant pseudopotential $P(x) = \eta(x)$, where $\eta(x)$ is a function of the period $L = L_* + L_0$, defined as

$$\eta(x) = \begin{cases} -1, & x \in [0; L_*); \\ +1, & x \in [L_*; L_* + L_0), \end{cases} \quad (2.11)$$

Function (2.11) is represented in Figure 2.4. Equation (2.1) takes form

$$u_{xx} - u + \eta(x)u^3 = 0. \quad (2.12)$$

Since pseudopotential is a piecewise constant function that has only two different

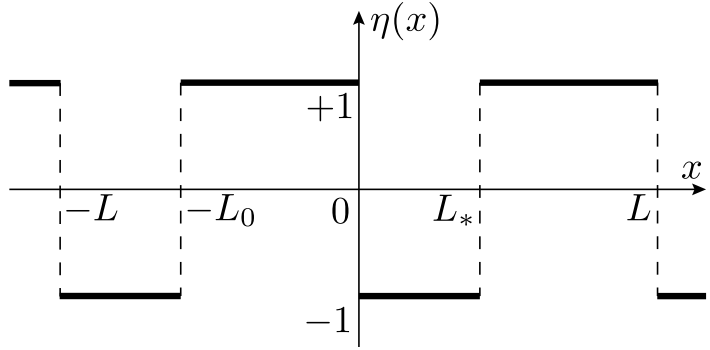


Figure 2.4. Plot of function $\eta(x)$ defined in (2.11).

values on the period L we can split the period into two intervals and consider two different cases for equation (2.12). In each region Eq. (2.12) has a form of conservative Duffing equation:

$$u_{xx} - u - u^3 = 0, \quad x \in [0; L_*]; \quad (2.13)$$

$$u_{xx} - u + u^3 = 0, \quad x \in [L_*; L_* + L_0]. \quad (2.14)$$

Each of equations (2.13), (2.14) can be solved explicitly through Jacobi elliptic functions. Exact solutions are given in Appendix B.

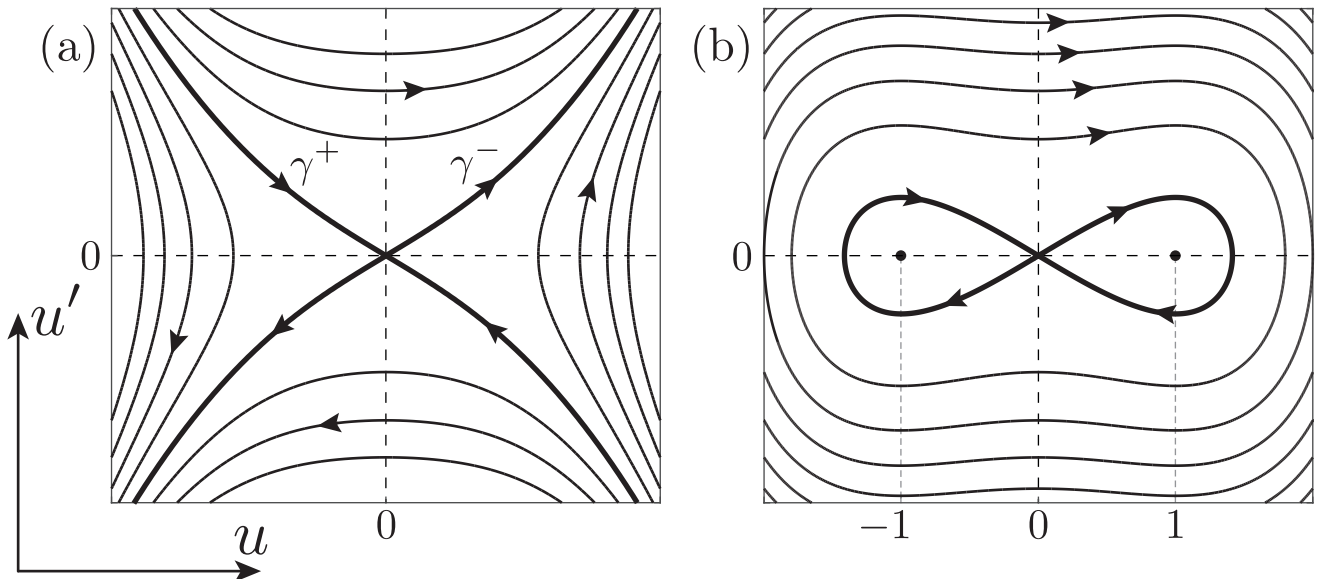


Figure 2.5. Phase portraits for different cases of equation (2.12) with piecewise pseudopotential (2.11). Panel (a) represents the phase portrait for equation (2.13), curves γ^\pm correspond to the separatrices which enter the equilibrium point $(0, 0)$ as x approaches $\pm\infty$. Panel (b) depicts the phase portrait for equation (2.14).

Equation (2.13) has a first integral of the form:

$$H_* = u_x^2 - u^2 - \frac{1}{2}u^4. \quad (2.15)$$

The phase portrait for equation (2.13) is presented in Figure 2.5 (a). Any trajectory on the phase plane corresponds to some value of H_* . Level $H_* = 0$ corresponds to the equilibrium state $(0, 0)$, and four separatrices related to it. Two of the separatrices $\gamma_{1,2}^+$ enter the zero equilibrium as x approaches $+\infty$. We denote them by curve γ^+ . Another two separatrices $\gamma_{1,2}^-$ enter the zero equilibrium as x approaches $-\infty$. We denote them by curve γ^- correspondingly. Resulting curves γ^\pm satisfy the equations

$$u' = \pm \frac{u}{\sqrt{2}} \sqrt{2 + u^2}. \quad (2.16)$$

It follows from the exact form of the solutions of equation (2.13) that all of them, except the zero one, are singular. It means that a solution for a Cauchy problem with initial conditions $u(0) = u_0$, $u'(0) = u'_0$ (u_0 and u'_0 not equals zero simultaneously) tends to infinity while x approaches some finite point both to the left and to the right of $x = 0$. It means that a solution for equation (2.13) has a *finite domain* if $H_* \neq 0$.

The first integral of equation (2.14) is

$$H_0 = u_x^2 - u^2 + \frac{1}{2}u^4. \quad (2.17)$$

Phase portrait for equation (2.14) is given in Figure 2.5 (b). It has two center equilibrium points $(\pm 1, 0)$ and one hyperbolic equilibrium point $(0, 0)$. Separatrix loops correspond to the localized solutions

$$u(x) = \pm \frac{\sqrt{2}}{\cosh x}. \quad (2.18)$$

The area inside the separatrix loops is filled by closed orbits of periodic solutions with nonzero mean. All other orbits turn around the origin and correspond to solutions with zero mean. That's why we mark a corresponding period part L_0 with a symbol “0”, since it looks like a little curve circle.

2.3.1. General Propositions on the \mathcal{U}_L^\pm Sets for Piecewise Pseudopotential

Let's move on to the consideration of the \mathcal{U}_L^\pm sets for equation (2.12). We consider a decomposition of the Poincaré map $\mathcal{P} = \mathcal{P}_0 \mathcal{P}_*$, where maps associated with corresponding parts of the overall period L are defined in a similar manner as the initial Poincaré map \mathcal{P} itself (2.2). Map \mathcal{P}_* maps a point (u_0, u'_0) to $(u(L_*), u'(L_*))$ where $u(x)$, $x \in [0; L_*]$ is a solution of Eq. (2.13) with initial conditions $u(0) = u_0$, $u'(0) = u'_0$. Similarly map \mathcal{P}_0 maps a point (u_0, u'_0) to $(u(L), u'(L))$ where $u(x)$, $x \in [L_*; L]$ is a solution of Eq. (2.14) with initial conditions $u(L_*) = u_0$, $u'(L_*) = u'_0$.

Note that \mathcal{P}_* is not defined in the whole \mathbb{R}^2 . We denote by $\mathcal{U}_{L_*}^+$ a domain of the map \mathcal{P}_* . Due to the fact that all solutions of equation (2.14) are regular, domain of the map \mathcal{P} coincide with the domain of \mathcal{P}_* map, i.e.

$$\mathcal{U}_L^+ = \text{dom}(\mathcal{P}) = \text{dom}(\mathcal{P}_0 \mathcal{P}_*) = \text{dom}(\mathcal{P}_*) \equiv \mathcal{U}_{L_*}^+. \quad (2.19)$$

Since the phase portrait for Eq. (2.13) is symmetric with respect to the origin, $\mathcal{U}_{L_*}^+$ is also symmetric with respect to the origin (see how its computed in Figure 2.8). Two separatrices $\gamma_{1,2+}$ that correspond to the curve γ^+ enter zero equilibrium as $x \rightarrow +\infty$. It means that for any initial data posed at γ^+ and for any L_* the map \mathcal{P}_* is correctly defined, i.e. $\gamma^+ \in \mathcal{U}_{L_*}^+$. Another property of $\mathcal{U}_{L_*}^+$ directly follows from Proposition 4:

$$\mathcal{P}_*(\mathcal{U}_{L_*}^+) = I(\mathcal{U}_{L_*}^+) = \mathcal{U}_{L_*}^-. \quad (2.20)$$

Move on to the $\mathcal{U}_{L_*}^-$ set for equation (2.13). Since $\mathcal{U}_{L_*}^-$ is a reflection of $\mathcal{U}_{L_*}^+$ with respect to the u' axis, it inherits its symmetry properties. Set $\mathcal{U}_{L_*}^-$ also contains curve γ^- that corresponds to another two separatrices $\gamma_{1,2}^-$ of equation (2.13). Consider the second map \mathcal{P}_0 of the decomposition. As we mentioned above \mathcal{P}_0 is correctly defined on the whole $\mathcal{U}_{L_*}^-$. It turns out that the image $\mathcal{P}_0(\gamma^-)$ has a spiral-like structure and intersects the curve γ^+ infinitely many times. The following proposition is valid.

Proposition 6. \mathcal{P}_0 -image of the curve γ^- intersects γ^+ infinitely many times at the points $\{0\} \cup u_{\pm n}$,

$$u_{\pm n} = \pm \frac{2x_{n-1}}{\sqrt[4]{2}L_0} + \mathcal{O}\left(H_0^{-1/4}\right), \quad n \in \mathbb{N}, \quad (2.21)$$

as $H_0 \rightarrow \infty$, where

$$x_n = \operatorname{cn}^{-1}\left(2^{-1/4}, k_0\right) + K(k_0)n. \quad (2.22)$$

Here $K(k)$ is the complete elliptic integral of the first kind, and $k_0 = 1/\sqrt{2}$.

Proof. First of all, the point $(0, 0)$ belongs to the intersection $\mathcal{P}_0(\gamma^-) \cap \gamma^+$ since it's a stable fixed point of equation (2.14) and the \mathcal{P}_0 map.

Next we note that all the intersections $\mathcal{P}_0(\gamma^-) \cap \gamma^+$ occur outside of the separatrix loops of (2.14) and correspond to zero mean solutions of (2.14). This obviously follows from that fact that γ^+ lies outside of the loops both from left and right of u' axis (depicted in Fig. 2.6 (a)).

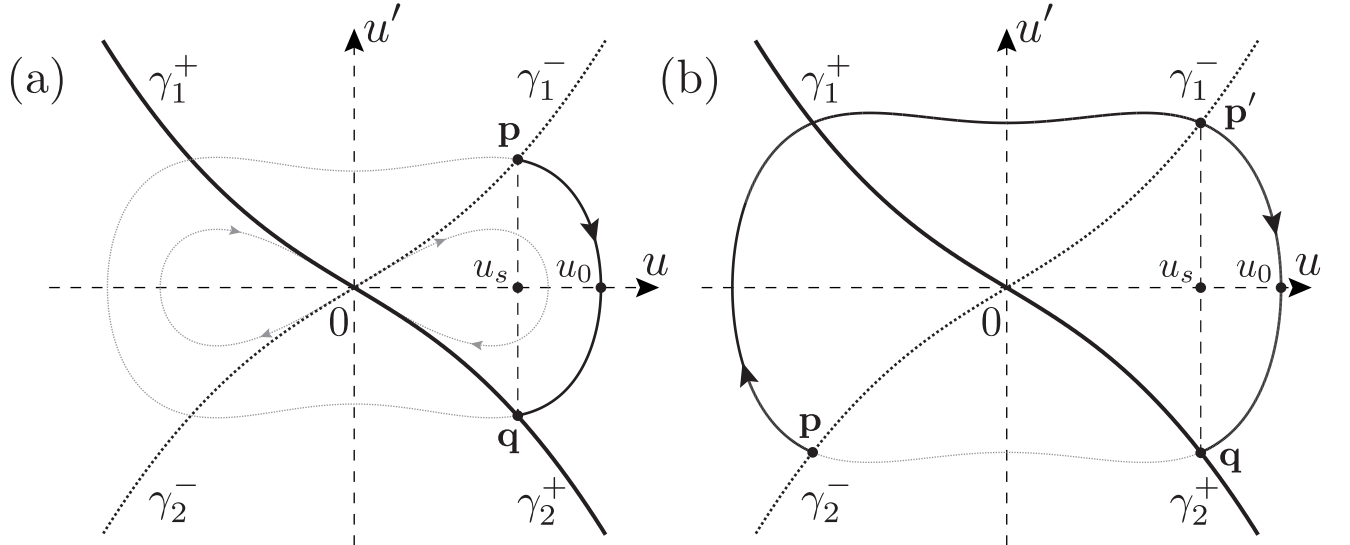


Figure 2.6. Illustration to the proof of Proposition 6.

Prove the formula for the points from the right side of u' axis, u_{+n} . Such points corresponds to the γ_2^+ separatrix of equation (2.13), see Figure 2.6. Result points of intersections $\mathcal{P}_0(\gamma^-) \cap \gamma_2^+$ can be divided into two groups: $\mathcal{P}_0(\gamma_1^-) \cap \gamma_2^+$ and $\mathcal{P}_0(\gamma_2^-) \cap \gamma_2^+$.

Consider points from the first group. Let a point \mathbf{q} belong to the intersection $\mathcal{P}_0(\gamma_1^-) \cap \gamma_2^+$. Then there exists a point $\mathbf{p} = (u_s, u'_s) \in \gamma_1^-$ such that $\mathcal{P}_0(\mathbf{p}) \in \gamma_2^+$. Due to the symmetries of the phase portraits for equations (2.13) and (2.14), $\mathbf{q} = (u_s, -u'_s)$, see Figure 2.6 (a). Consider a phase trajectory of (2.14) that lies outside of separatrix loop and connects points \mathbf{p} and \mathbf{q} . According to Appendix B exact form of the solution is

$$u(x) = x_0 \operatorname{cn} \left(\sqrt{x_0^2 - 1} x + x_1, k \right), \quad (2.23)$$

where k is elliptic modulus,

$$k = \frac{1}{\sqrt{2}} \frac{x_0}{\sqrt{x_0^2 - 1}}, \quad (2.24)$$

and x_0, x_1 are constants that are determined by initial conditions $(u(0), u'(0)) = \mathbf{p}$.

Next let's introduce x variable shift $x \rightarrow x - L_0/2$. Equation (2.23) persists its form but now $u(0) = u_0$, $u_0 > 0$, and $u'(0) = 0$. That allows us to determine constants x_0, x_1 : $x_0 = u_0$, $x_1 = 0$. Solution (2.23) takes form

$$u(x) = u_0 \operatorname{cn} \left(\sqrt{u_0^2 - 1} x, k \right), \quad (2.25)$$

and for coordinates of the points \mathbf{p} and \mathbf{q} we have

$$\mathbf{p} = (u(-L_0/2), u'(-L_0/2)) = (u_s, u'_s); \quad (2.26)$$

$$\mathbf{q} = (u(L_0/2), u'(L_0/2)) = (u_s, -u'_s). \quad (2.27)$$

Since value of H_0 (2.17) conserves on the trajectory that connects point \mathbf{p} and the point $(u_0, 0)$ one can write

$$H_0 = -u_0^2 + \frac{u_0^4}{2} = (u'_s)^2 - u_s^2 + \frac{u_s^4}{2}. \quad (2.28)$$

On the other hand the point \mathbf{p} belong to the separatrix of (2.13) and its coordinates satisfy an equality

$$H_* = (u'_s)^2 - u_s^2 - \frac{u_s^4}{2} = 0. \quad (2.29)$$

Comparing (2.28) and (2.29) one can conclude that

$$u_s^4 = \frac{u_0^4}{2} - u_0^2. \quad (2.30)$$

At the point \mathbf{q} we have

$$u_s = u_0 \operatorname{cn} \left(\frac{\sqrt{u_0^2 - 1} L_0}{2}, k \right). \quad (2.31)$$

Substitute u_s from (2.30) into (2.31), divide both side of the equality by u_0 , and introduce $4v_0^2 = u_0^2 - 1$. Equation (2.31) takes form

$$\left(\frac{1}{2} - \frac{1}{4v_0^2 + 1} \right)^{1/4} = \operatorname{cn}(v_0 L_0, k), \quad k = \frac{1}{\sqrt{2}} \sqrt{1 + \frac{1}{4v_0^2}}. \quad (2.32)$$

Let us analyse the limit $v_0 \rightarrow \infty$. First of all consider k as a function of v_0 and expand it into the series:

$$k(v_0) = \frac{1}{\sqrt{2}} + \frac{1}{8\sqrt{2}} \frac{1}{v_0^2} - \frac{1}{32\sqrt{2}} \frac{1}{v_0^4} + \dots \quad (2.33)$$

Let $k_0 = 1/\sqrt{2}$. We introduce the remainder $\Delta k = k(v_0) - k_0$. Note that Δk has the main term of order v_0^{-2} as $v_0 \rightarrow \infty$. Denote $w_0 = v_0 L_0$, consider $\operatorname{cn}(w_0, k)$ in the right side of (2.32) as a function of elliptic modulus k and expand it into the series in the vicinity of k_0 up to the second term:

$$\operatorname{cn}(w_0, k_0 + \Delta k) = \operatorname{cn}(w_0, k_0) + f(w_0, k_0) \Delta k + \mathcal{O}(w_0^{-1/4}). \quad (2.34)$$

Here $f(w_0, k_0)$ is the first derivative of elliptic cosine with respect to k at $k = k_0$:

$$f(w_0, k_0) = \frac{\operatorname{sn}(w_0) \operatorname{dn}(w_0) (w_0 - k_0 w_0 + k_0 \operatorname{sn}(w_0) \operatorname{cd}(w_0) - E(\phi(w_0)))}{2(k_0 - 1) k_0}. \quad (2.35)$$

Here $\phi(w, k)$ is the Jacobi amplitude and $E(\phi, k)$ is the incomplete elliptic integral of the second kind. All elliptic functions have the same modulus k_0 , we omit this parameter for the sake of brevity. This expression is quite tremendous, nevertheless, what interests us here is the orders of terms with respect to w_0 . It has a leading term of order w_0 as $w_0 \rightarrow \infty$. That allows us to conclude that the term $f(w_0, k_0) \Delta k$

of (2.34) in its turn has a leading term of order w_0^{-1} (or v_0^{-1}). Rewrite (2.32) in a form:

$$\left(\frac{1}{2} - \frac{1}{4v_0^2 + 1}\right)^{1/4} = \operatorname{cn}(v_0 L_0, k_0) + \mathcal{O}(v_0^{-1}), \quad (2.36)$$

Using the same approach again we expand the left side of (2.36) into a series:

$$\left(\frac{1}{2} - \frac{1}{4v_0^2 + 1}\right)^{1/4} = \frac{1}{\sqrt[4]{2}} - \frac{1}{2\sqrt[4]{2}} \frac{1}{(4v_0^2 + 1)} + \mathcal{O}(v_0^{-4}). \quad (2.37)$$

Combining (2.37) with (2.36) and comparing the orders of terms we conclude that

$$\operatorname{cn}(v_0 L_0, k_0) = \frac{1}{\sqrt[4]{2}} + \mathcal{O}(v_0^{-1}). \quad (2.38)$$

Let's express $v_0 L_0$ in the equation above

$$v_0 L_0 = \operatorname{cn}^{-1}\left(\frac{1}{\sqrt[4]{2}} + \mathcal{O}(v_0^{-1}), k_0\right) + 2K(k_0)n, \quad n \in \{0\} \cup \mathbb{N}. \quad (2.39)$$

Here $K(k)$ is the complete elliptic integral of the first kind. We left only positive roots since we are interested only in intersections $\mathcal{P}_0(\gamma_1^-) \cap \gamma_2^+$ where u_0 is positive and we can write

$$v_0 = \frac{u_0}{2} \sqrt{1 - \frac{1}{u_0^2}} = \frac{u_0}{2} - \frac{1}{2u_0} + \mathcal{O}(u_0^{-3}). \quad (2.40)$$

We note that by definition of cn^{-1} function

$$\operatorname{cn}^{-1}\left(2^{-1/4} + \mathcal{O}(v_0^{-1})\right) = F\left(\arccos\left(2^{-1/4} + \mathcal{O}(v_0^{-1})\right), k_0\right), \quad (2.41)$$

where $F(\phi, k)$ is incomplete elliptic integral of the first kind. Consider series expansion of \arccos up to the main term:

$$\arccos\left(2^{-1/4} + \mathcal{O}(v_0^{-1})\right) = \arccos\left(2^{-1/4}\right) + \mathcal{O}(v_0^{-1}). \quad (2.42)$$

Let's substitute (2.42) into (2.41), use additive property of integral, and apply integral mean value theorem to the second term:

$$\begin{aligned} \operatorname{cn}^{-1}\left(2^{-1/4} + \mathcal{O}(v_0^{-1})\right) &= F\left(\arccos\left(2^{-1/4}\right) + \mathcal{O}(v_0^{-1}), k_0\right) = \\ &= F\left(\arccos\left(2^{-1/4}\right), k_0\right) + F\left(\mathcal{O}(v_0^{-1}), k_0\right) = \\ &= \operatorname{cn}^{-1}\left(2^{-1/4}, k_0\right) + \mathcal{O}(v_0^{-1}). \end{aligned} \quad (2.43)$$

Put (2.43) and (2.40) into (2.39), also note that according to (2.40) we can safely replace $\mathcal{O}(v_0^{-1})$ with $\mathcal{O}(u_0^{-1})$,

$$u_0 = \frac{2}{L_0} \left(\operatorname{cn}^{-1} \left(2^{-1/4}, k_0 \right) + 2K(k_0)n \right) + \mathcal{O}(u_0^{-1}). \quad (2.44)$$

Finally let's get rid of u_0 in favor of u_s . For that purpose according to (2.28) we can write $\mathcal{O} \left(H_0^{-1/4} \right)$ instead of $\mathcal{O}(u_0^{-1})$, and it follows from (2.30) that

$$u_s = \frac{1}{\sqrt[4]{2}} u_0 + \mathcal{O}(u_0^{-1}). \quad (2.45)$$

Let's introduce the following denotation

$$x_n = \operatorname{cn}^{-1} \left(2^{-1/4}, k_0 \right) + 2K(k_0)n. \quad (2.46)$$

Now combining the expressions above all together and replacing u_s with u_{+n} we get

$$u_{+n} = \frac{2x_{n-1}}{\sqrt[4]{2}L_0} + \mathcal{O} \left(H_0^{-1/4} \right), \quad n \in \mathbb{N}. \quad (2.47)$$

In order to get the final formula of the proposition for $\{u_{+n}\}$ we need to consider points of intersections from the second group $\mathcal{P}_0(\gamma_2^-) \cap \gamma_2^+$. We can easily reduce this task to the previous one. Let there exists a point of intersection $\mathbf{q} \in \gamma_2^+$. Consider point $\mathbf{p} \in \gamma_2^-$, such that $\mathcal{P}_0(\mathbf{p}) = \mathbf{q}$, see Fig. 2.6 (b). We note that there exists a point $\mathbf{p}' \in \gamma_1^-$, and the trajectory (2.23) goes from the point \mathbf{p} to \mathbf{p}' over a half of the period $2K(k)/\sqrt{x_0^2 - 1}$, and after that cross the u axis at the point u_0 . Then we introduce an x variable shift $x \rightarrow x - (L_0/2 + K(k)/\sqrt{x_0^2 - 1})$, so that $u(0) = u_0$, $u_0 > 0$, and $u'(0) = 0$, and can determine $x_0 = u_0$, $x_1 = 0$. Solution (2.23) takes form (2.25) again and for coordinates of the points \mathbf{p}' and \mathbf{q} we have

$$\mathbf{p}' = \left(u \left(-L_0/2 + \frac{K(k)}{\sqrt{u_0^2 - 1}} \right), u' \left(-L_0/2 + \frac{K(k)}{\sqrt{u_0^2 - 1}} \right) \right) = (u_s, u'_s); \quad (2.48)$$

$$\mathbf{q} = \left(u \left(L_0/2 - \frac{K(k)}{\sqrt{u_0^2 - 1}} \right), u' \left(L_0/2 - \frac{K(k)}{\sqrt{u_0^2 - 1}} \right) \right) = (u_s, -u'_s). \quad (2.49)$$

Now we can use relations (2.48), (2.49) instead of (2.26), (2.27), and repeat all the steps above. Difference in x variable shift results in the additional term $K(k)$ in

(2.39) and (2.44). Finally we replace $K(k) = K(k_0 + \Delta k) = K(k_0) + \mathcal{O}(H_0^{-2/4})$, and get the following relation for x_n :

$$x_n = \operatorname{cn}^{-1} \left(2^{-1/4}, k_0 \right) + K(k_0)(2n+1). \quad (2.50)$$

Relation (2.47) remains the same. Combining (2.46) with (2.50) we get the result for separatrix intersections points $\{u_{+n}\} \in \mathcal{P}(\gamma^-) \cap \gamma_2^+$:

$$u_{+n} = \frac{2x_{n-1}}{\sqrt[4]{2}L_0} + \mathcal{O} \left(H_0^{-1/4} \right), \quad n \in \mathbb{N}, \quad (2.51)$$

where x_n satisfies the relation

$$x_n = \operatorname{cn}^{-1} \left(2^{-1/4}, k_0 \right) + K(k_0)n. \quad (2.52)$$

Points $\{u_{-n}\}$, $n \in \mathbb{N}$ from the left side of u' axis, $u_{-n} \in \mathcal{P}_0(\gamma^-) \cap \gamma_1^+$, should be treated in a similar way, proposition is proven. \square

Propositions 6 says that the far we goes from the $(0, 0)$ point on the phase plane, the better the asymptotic relation (2.21) works. It turns out that formula (2.21) works pretty well even for small number of n . See Figure 2.7 where we compare the predicted coordinates with actual intersections obtained by numerical computation of $\mathcal{P}_0(\gamma^-)$. Another interesting consequence of Proposition 6 is that set \mathcal{U}_L consists of infinitely many connected components. This obviously follows from that fact, that set $\mathcal{U}_{L_*}^-$ contains the entire curve γ^- and map \mathcal{P}_0 is continuous, so the image $\mathcal{P}_0(\mathcal{U}_{L_*}^-)$ cross \mathcal{U}_L^+ infinitely many times.

2.3.2. Construction of the Poincaré Map Domains

One of the possible way to construct \mathcal{U}_L^\pm sets for different maps associated with equation (2.1) is to use a numerical procedure called scanning of initial conditions plane (u, u') . That's how it works. At first ranges of scanning $u_{\min} \leq u \leq u_{\max}$, $u'_{\min} \leq u' \leq u'_{\max}$ are selected. Then the target segment of the initial conditions plane is covered by a uniform grid with small steps h and h' for each axis u and

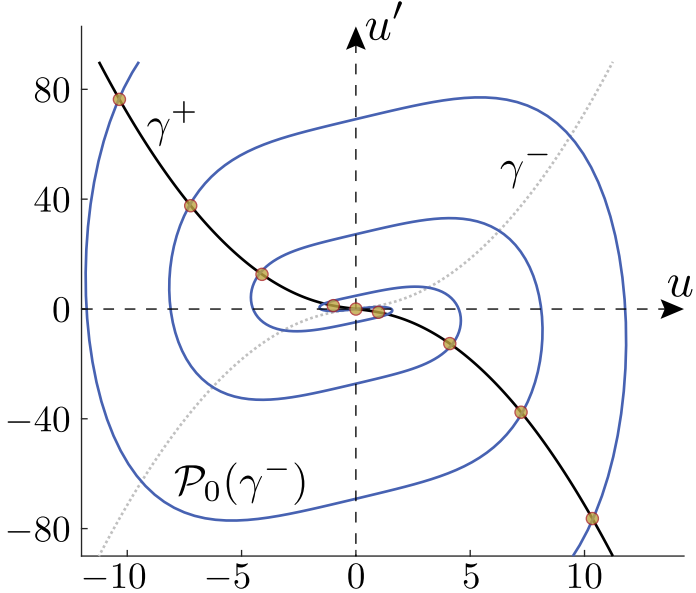


Figure 2.7. Comparison of asymptotic formula (2.21) with numerical computations for $L_0 = 1$. Curves γ^\pm are formed by the separatrices of (2.13), \mathcal{P}_0 -image of γ^- is a solid blue line computed numerically. Predicted points of intersections $u_{\pm n}$ from $\mathcal{P}_0(\gamma^-) \cap \gamma^+$ are marked with yellow dots. One can see that (2.21) predicts intersections quite precisely even for small number of n .

u' . Using Runge-Kutta 4th order method we solve differential equation in each node of the resulting grid. We use an interval $[0; L]$ for \mathcal{U}_L^+ where x changes in forward direction from 0 to L , and an interval $[-L; 0]$ in order to get \mathcal{U}_L^- where x changes in backward direction from 0 to $-L$. If absolute value of a calculated solution does not exceed some predefined constant M that is large enough, we suppose that such solution is non-collapsing, and include corresponding node point into \mathcal{U}_L^\pm sets. Then we color nodes on the initial conditions plane that correspond to non-collapsing solutions to get the final picture of \mathcal{U}_L^\pm sets. In our experiments we used $M = 10^5$ and $M = 10^7$, and got consistent results. Such procedure is pretty straightforward and can be efficiently performed by a computer since it admits natural parallelization. Let's apply this procedure to equation (2.12).

On Figure 2.8 (a) Poincaré map domain $\mathcal{U}_L^+ = \mathcal{U}_{L_*}^+$ for the parameters $(L_*, L_0) = (2, 1)$ is depicted. As we mentioned above it contains the curve γ^+ formed by separatrices of (2.13). Figure 2.8 (b) represents a \mathcal{P}_* -image of $\mathcal{U}_{L_*}^+$, $\mathcal{P}_*(\mathcal{U}_{L_*}^+) = \mathcal{U}_{L_*}^-$. According to Proposition 4 set $\mathcal{P}_*(\mathcal{U}_{L_*}^-)$ can be obtained by a reflection of the set

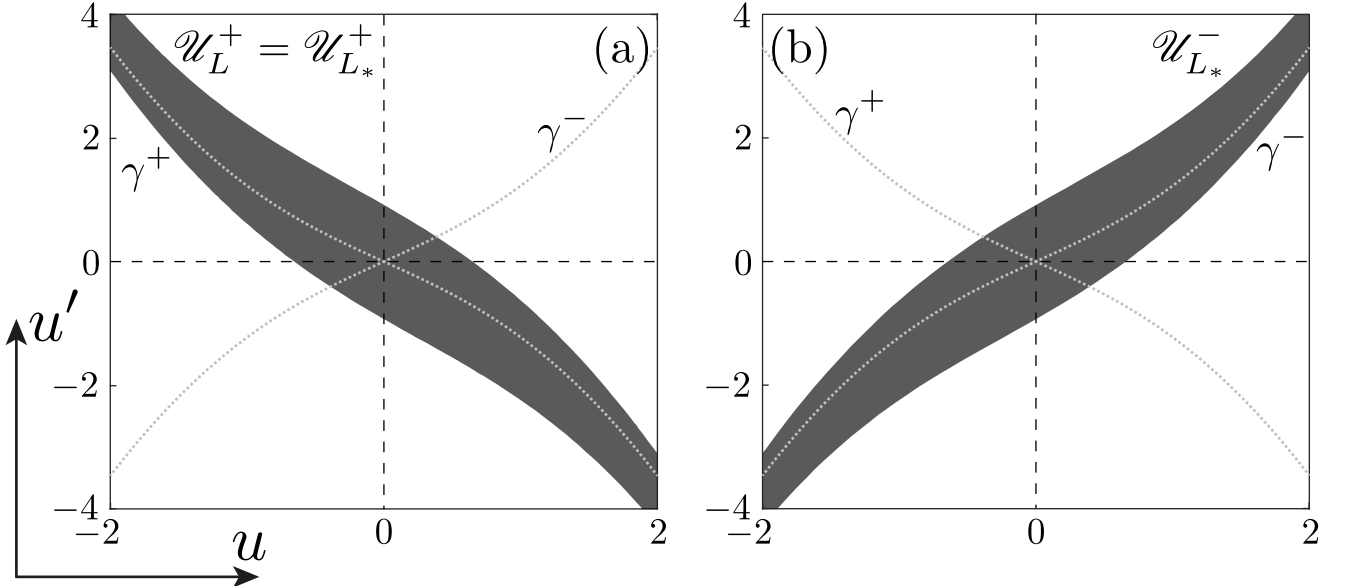


Figure 2.8. Sets $\mathcal{U}_{L_*}^{\pm}$ for the equation (2.13) for the parameter $L_* = 2$. Panel (a) represents $\mathcal{U}_{L_*}^{+}$ set, it coincides with the set \mathcal{U}_L^{+} for equation (2.12), since all solutions of the second equation (2.14) are regular. Panel (b) depicts $\mathcal{U}_{L_*}^{-}$ set, it's just a reflection of the set \mathcal{U}_L^{+} from the right panel due to Proposition 4.

$\mathcal{U}_{L_*}^{+}$, with respect to the u' axis. Set $\mathcal{U}_{L_*}^{-}$ in its turn contains curve γ^- .

Let's continue our scanning in order to get set \mathcal{U}_L^{-} and then intersect it with \mathcal{U}_L^{+} . On Figure 2.9 (a) set \mathcal{U}_L^{-} and its intersection with \mathcal{U}_L^{+} set are depicted for values of parameters $(L_*, L_0) = (2, 1)$. From our numerical procedure we can conclude that intersection $\mathcal{U}_L = \mathcal{U}_L^{+} \cap \mathcal{U}_L^{-}$ represents three connected components with monotonic borders. These components form a three-island set in the scanning area $-2 \leq u \leq 2$, $-4 \leq u' \leq 4$, denote them by D_i , $i \in \{-1, 0, +1\}$. Indeed, along with the monotonicity of the connected components borders we also know that two opposite borders of D_i , which entirely belong to the borders of the set \mathcal{U}_L^{+} , consist of points that are mapped to infinity under action of \mathcal{P} (by construction of \mathcal{U}_L^{+}). On other hand borders of \mathcal{U}_L^{-} contain two other borders of each D_i , and they are mapped to infinity under action of \mathcal{P}^{-1} . Thereby the obtained structure satisfy all the conditions of island set from Definition 4. However set \mathcal{U}_L^{-} entirely contains an image of the curve γ^- . We know that according to Proposition 6 image $\mathcal{P}(\gamma^-)$ has infinitely many intersections with the curve γ^+ . That's why outside of the scanning area there exist many other intersections between sets \mathcal{U}_L^{\pm} , and they form infinitely

many connected components in the result set \mathcal{U}_L . In a similar manner we denote those components by D_k , $k \in \{-1, -2, -3, \dots\}$ for the components on the left side of the u' axis and $k \in \{+1, +2, +3, \dots\}$ for the components on the right side. Due to monotonicity of \mathcal{U}_L^+ borders and general geometric properties of the spiral \mathcal{U}_L^- we can hypothesize that all the components D_k in \mathcal{U}_L set are also islands.

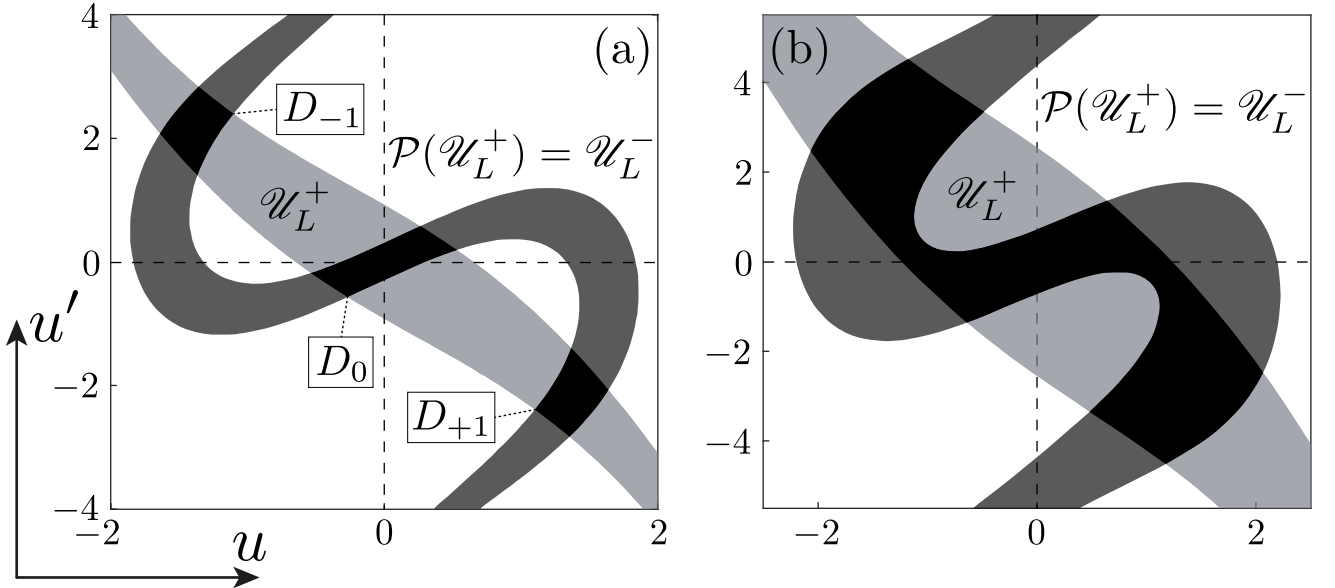


Figure 2.9. Sets \mathcal{U}_L^+ (light gray), \mathcal{U}_L^- (dark gray), and their intersection \mathcal{U}_L for two different sets of parameters. Panel (a) depict the case $(L_*, L_0) = (2, 1)$; three central connected components D_i form an island set. Panel (b) correspond to the case $(L_*, L_0) = (1.3, 1)$; geometry of the result sets does not allow to form islands.

Our numerical studies shows that for equation (2.12) three central components of \mathcal{U}_L play a crucial role in an island set formation. For example in Figure 2.1 (b) geometry of the \mathcal{U}_L^- for parameters $(L_*, L_0) = (1.3, 1)$ does not allow to form an island around the center. Establishing a criteria for existence of the island set is a quite tricky task even for a simple form equation (2.12), and such criteria is out of scope for the current work. Our approach is based on scanning of a sufficiently large subset of initial conditions plane around the center $(u, u') = (0, 0)$. If the resulting subset of \mathcal{U}_L form an island set we just *make a hypothesis* that all other intersections and also islands.

2.3.3. Complete Island Set

Let \mathcal{U}_L represents an island set. It turns out that for Eq. (2.12) the property of “completeness” for an island set in a sense of Definition 8 naturally arises from its construction. Let’s demonstrate it in an heuristic manner. At first, upper boundary of the set $\mathcal{U}_L^+ = \mathcal{U}_{L_*}^+$ consists of such points that the corresponding solution to the Cauchy problem with initial conditions at these points tends to $+\infty$ exactly at the point $x = L_*$. Therefore, while point \mathbf{p} is approaching to the upper boundary of \mathcal{U}_L^+ it’s \mathcal{P} -images tends to $(+\infty, +\infty)$. On other hand lower boundary of \mathcal{U}_L^+ consists of points that the corresponding solution to the Cauchy problem with initial conditions at these points tends to $-\infty$. So, while point \mathbf{p} is approaching to the lower boundary of \mathcal{U}_L^+ it’s \mathcal{P} -images tends to $(-\infty, -\infty)$.

Let’s consider a curve Γ inside one of islands $D_i \in \mathcal{U}_L$ that connects opposite boundaries of the set \mathcal{U}_L^+ . Denote by Γ_* its \mathcal{P}_* -image, $\Gamma_* = \mathcal{P}_*(\Gamma)$. It’s clear that Γ_* belongs to $\mathcal{U}_{L_*}^-$, and it’s stretched out continuously from $-\infty$ to $+\infty$ by u inside $\mathcal{U}_{L_*}^-$. Now consider the second map \mathcal{P}_0 of the decomposition $\mathcal{P} = \mathcal{P}_0 \mathcal{P}_*$. We know that this map curls the set $\mathcal{U}_{L_*}^-$ into a spiral (see Fig. 2.9 (a)). This spiral intersects \mathcal{U}_L^+ and form islands. So if we consider the \mathcal{P}_0 -image of Γ_* and take into account that the value of H_0 remains the same for all trajectories of (2.14) associated with \mathcal{P}_0 map, we can conclude that $\mathcal{P}_0(\Gamma_*)$ is stretched along the whole set \mathcal{U}_L^- and intersects each of the islands $D_i \in \mathcal{U}_L$ at least once. Such reasoning leads us to the conclusion that all islands in \mathcal{U}_L are forward-reachable. Similar consideration shows that islands from \mathcal{U}_L are also backward-reachable and the constructed island set is complete.

Let’s illustrate this idea. For this purpose we construct \mathcal{P}_* and \mathcal{P} -images of islands from Figure 2.9 (a). Again we do this numerically with the scanning procedure described above. In Figure 2.10 (a) one can see the \mathcal{P}_* -image of islands $D_i, i \in \{-1, 0, +1\}$. As we have expected these images are infinite curvilinear strips stretched inside the \mathcal{P}_* -image of the \mathcal{U}_L^+ set. \mathcal{P} -images of the islands are depicted

in Figure 2.10 (b). Images $\mathcal{P}(D_i)$ are infinite curvilinear strips curled up inside the \mathcal{U}_L^- set.

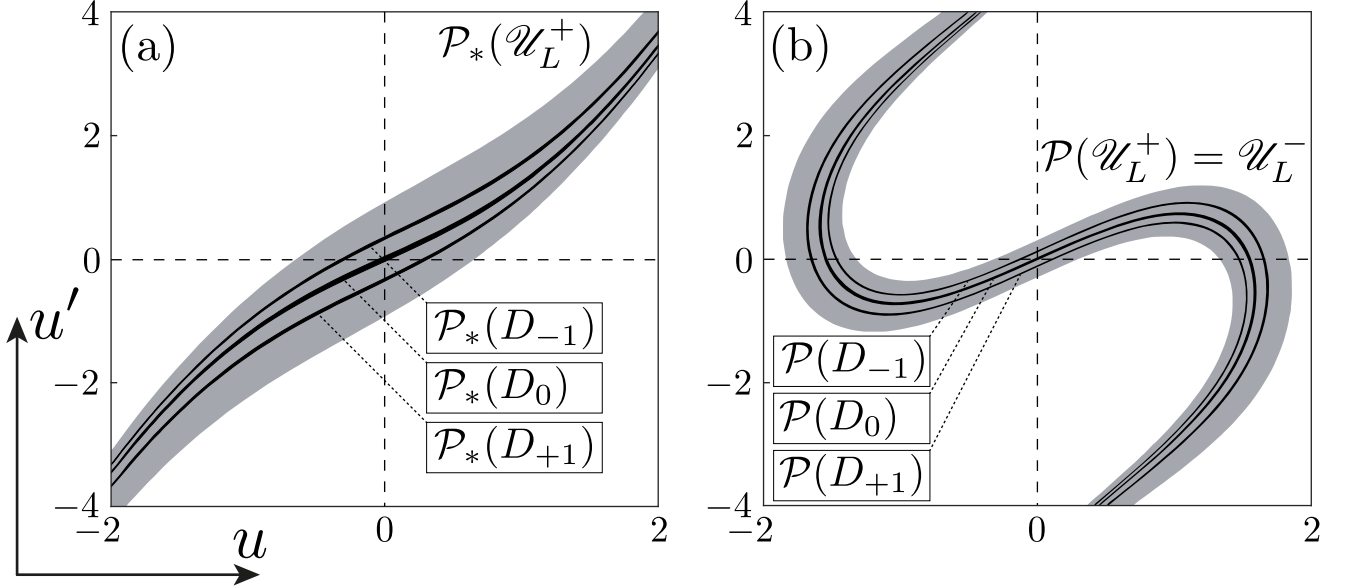


Figure 2.10. \mathcal{P}_* and \mathcal{P} -images of islands for Eq. (2.12) with parameters $(L_*, L_0) = (2, 1)$. Panel (a) represents their \mathcal{P}_* -images. Each image is a curvilinear strip stretched along the whole $\mathcal{P}_*(\mathcal{U}_L^+)$. Panel (b) represents \mathcal{P} -images.

The images $\mathcal{P}(D_i)$ resembles the image $\mathcal{P}_0(\gamma^-)$ of the separatrices γ^- . Each of them intersects \mathcal{U}_L^+ infinitely many times and cross each island from \mathcal{U}_L . To illustrate this, we combined Figure 2.10 (b) with Figure 2.9 (a) in Figure 2.11 where the notation: $\mathcal{P}(D_i) \cap D_j = H_{ij}$ is introduced.

The similar situation takes place for \mathcal{P}^{-1} map as well. Island set $\mathcal{U}_L = \bigcup_{i \in S} D_i$ for Eq. (2.12) is backward-reachable. It means that $V_{ij} = \mathcal{P}^{-1}(D_j) \cap D_i \neq \emptyset$ for each $i, j \in S$. In Figure 2.12 sets V_{ij} are depicted for $i, j \in \{-1, 0, +1\}$.

2.4. Symbolic Dynamics: Coding of Solutions

In this section we show how all the concepts introduced above can be used together to classify all bounded solutions of equation (2.1). Our classification is closely connected with the structure of the \mathcal{U}_L set. We demonstrate our approach for the previously considered piecewise pseudopotential equation (2.12). Let's introduce two sets.

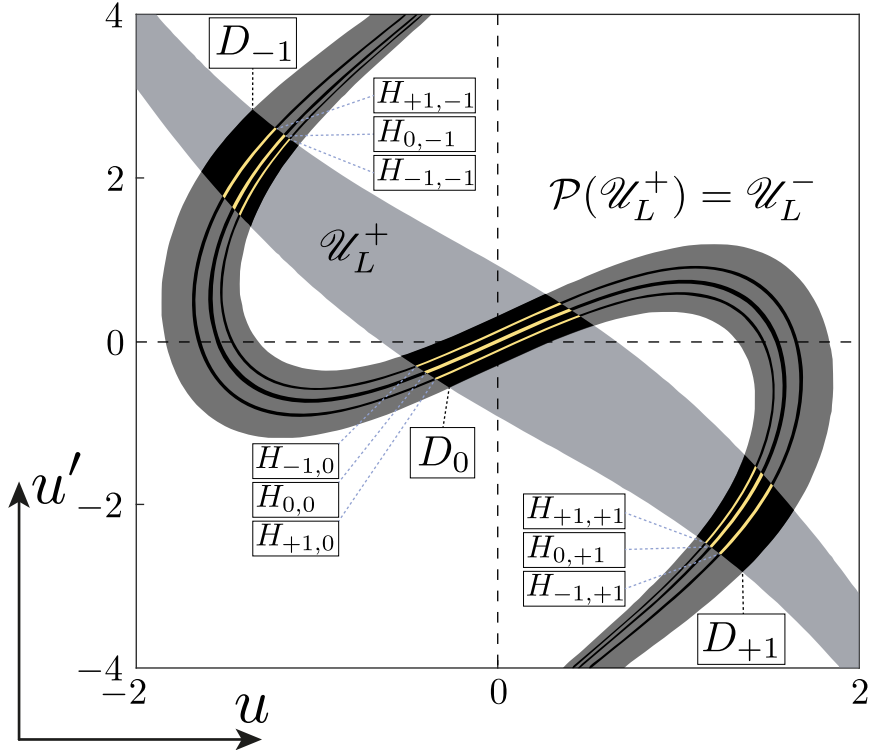


Figure 2.11. Island set $\mathcal{U}_L = \mathcal{U}_L^+ \cap \mathcal{U}_L^-$ and sets $H_{ij} = \mathcal{P}(D_i) \cap D_j$, $i, j \in \{-1, 0, +1\}$ for equation (2.12) with parameters $(L_*, L_0) = (2, 1)$. Island set $\mathcal{U}_L = \bigcup_{i \in S} D_i$ is forward-reachable, so \mathcal{P} -image of each island D_i intersects all other islands D_j , $j \in S$ including D_i itself.

Definition 12. Define set \mathcal{O} as a set of bi-infinite orbits of all regular solutions for equation (2.1), i.e. $\mathbf{r} \in \mathcal{O}$, $\mathbf{r} = \{\mathbf{p}_n\}$, $\mathcal{P}(\mathbf{p}_n) = \mathbf{p}_{n+1}$, $n \in \mathbb{Z}$.

Define a metric in \mathcal{O} as follows. Let $v, w \in \mathcal{O}$ be two orbits, $v = \{\mathbf{p}_n\}$, $\mathbf{p}_n = (\phi_n, \phi'_n)$, $w = \{\mathbf{q}_n\}$, $\mathbf{q}_n = (\psi_n, \psi'_n)$, then the distance $d_{\mathcal{O}}$ between orbits v and w is defined as a Euclidean distance between points \mathbf{p}_0 and \mathbf{q}_0 , i.e.

$$d_{\mathcal{O}}(v, w) = \|\mathbf{p}_0 - \mathbf{q}_0\| = \sqrt{(\phi_0 - \psi_0)^2 + (\phi'_0 - \psi'_0)^2}. \quad (2.53)$$

This implies that \mathcal{O} can be regarded as a topological space where neighbourhood $U_{\varepsilon}(u^*)$ of an element $u^* \in \mathcal{O}$ is defined as $U_{\varepsilon}(u^*) = \{u \mid d_{\mathcal{O}}(u^*, u) < \varepsilon\}$.

Definition 13. Define set \mathcal{S} as a set of bi-infinite sequences $\{\dots, i_{-1}, i_0, i_1, \dots\}$ over an alphabet where each symbol i_k , $k = 0, \pm 1, \dots$, corresponds to a connected component $D_k \in \mathcal{U}_L$.

We also write \mathcal{S}_N if the alphabet has N different symbols, and \mathcal{S}_{∞} if the number of symbols is infinite (corresponds to the infinite number of connected components in

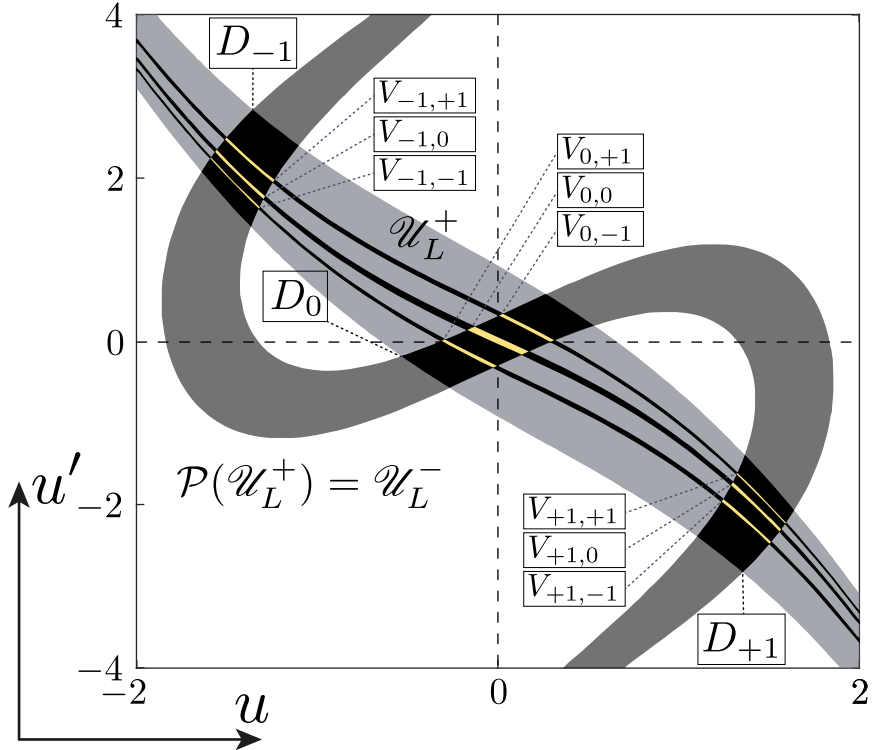


Figure 2.12. Island set $\mathcal{U}_L = \mathcal{U}_L^+ \cap \mathcal{U}_L^-$ and sets $V_{ij} = \mathcal{P}^{-1}(D_j) \cap D_i$, $i, j \in \{-1, 0, +1\}$ for equation (2.12) with parameters $(L_*, L_0) = (2, 1)$. Island set $\mathcal{U}_L = \bigcup_{i \in S} D_i$ is backward-reachable, so \mathcal{P} -pre-image of each island D_i intersects all other islands D_j , $j \in S$ including D_i itself.

\mathcal{U}_L). Set \mathcal{S} also can be regarded as a topological space where neighbourhood $W_k(\omega^*)$ of an element $\omega^* = \{\dots, i_{-1}^*, i_0^*, i_1^*, \dots\} \in \mathcal{S}$ is defined as $W_k(\omega^*) = \{\omega \mid i_s^* = i_s, |s| < k\}$.

What we are interested in is the connection between sets \mathcal{O} and \mathcal{S} . First of all the structure of island set \mathcal{U}_L can be easily used to assign symbolic sequences, also named codes, to the solutions, so the correspondence from \mathcal{O} to \mathcal{S} can be established. Let's demonstrate it with an example. Consider a localized solution $u(x)$ of Eq. (2.12) shown in the left panel of Figure 2.13. Construct the sequence of $(u(kL), u'(kL))$. On the plane (u, u') each of the points of this sequence is situated in some island D_i . In the point $x = 0$ value $u(0)$ and derivative $u'(0)$ match island D_{-1} . After that in the point $x = L$ our solution $u(x)$ cross the central islands D_0 and matches it again for $x = 2L$. In the point $x = 3L$ our solution came into the right island D_{+1} . That allows us to determine four central symbols of the result code: $\{-1, 0, 0, +1\}$, see Figure 2.13 (b). Moreover since our solution is localized all

other points $(u(kL), u'(kL))$ correspond to the central component of \mathcal{U}_L and all the symbols from the left side of “ -1 ” and the right side of “ $+1$ ” are “ 0 ”. Thereby finally we obtain the result bi-infinite sequence $\{\dots, 0, -1, 0, 0, +1, 0, \dots\}$ for the localized solution $u(x)$ from Figure 2.13 (a). Obviously points of orbit of our solution cannot lie down outside of \mathcal{U}_L because the solution is regular and has bi-infinite orbit, so at each step we have exactly one symbol to choose and the overall process identifies the result bi-infinite sequence uniquely.

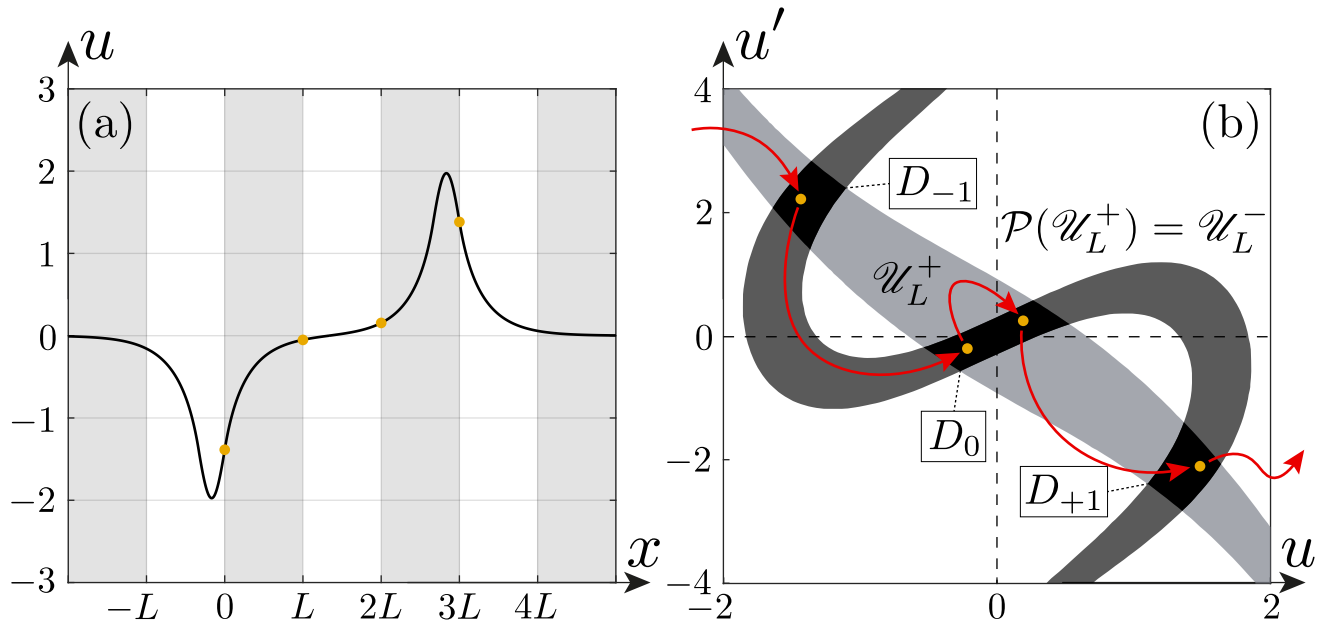


Figure 2.13. Illustration of the coding process. Panel (a) represents a localized solution for the Eq. (2.12) with parameters $(L_*, L_0) = (2, 1)$. This solution has been found numerically using the shooting method. Panel (b) represents a sketch of four points (yellow dots) of the solution orbit over the structure of the \mathcal{U}_L set. These points jump from island to island following the red arrows and determine the symbols of the result solution code: $\{\dots, 0, -1, 0, 0, +1, 0, \dots\}$.

2.4.1. Uniqueness of Solutions Coding

The most intriguing question about coding is the following: when is the correspondence between solutions orbits \mathcal{O} and codes \mathcal{S} based on the \mathcal{U}_L set structure for Eq. (2.1) is bijective (one-to-one)? We can also formulate another question: when there exists a homeomorphism between two topological spaces \mathcal{O} and \mathcal{S} ? In this section we determine sufficient conditions of existence of such correspondence.

One can reformulate one of the questions above as follows: could one find initial conditions for a Cauchy problem by a solution code? Let $\mathbf{s} = \{\dots, i_{-1}, i_0, i_1, \dots\}$ be a code derived from the structure of a complete island set \mathcal{U}_L . Consider its left part $\{\dots, i_{-2}, i_{-1}, i_0\}$. All the points from island D_{i_0} correspond to the symbol i_0 . Consider a set $H_{i_{-1}i_0} = \mathcal{P}(D_{i_{-1}}) \cap D_{i_0}$. The set $H_{i_{-1}i_0} \subset D_{i_0}$ consists of such points $\mathbf{p}_0 = (u_0, u'_0) \in D_{i_0}$ that the corresponding solution $u(x)$ to the Cauchy problem with initial conditions $u(0) = u_0, u'(0) = u'_0$ does not collapse at $[-L; 0]$, and $\mathbf{p}_{-1} = (u(-L), u'(-L)) \in D_{i_{-1}}$. Hence the code of solution with initial conditions taken from $H_{i_{-1}i_0}$ includes symbols $\{i_{-1}, i_0\}$. Continuing this process. Consider a set $H_{i_{-2}, i_{-1}, i_0} = \mathcal{P}(H_{i_{-2}, i_{-1}}) \cap D_{i_0}$, where $H_{i_{-2}, i_{-1}} = \mathcal{P}(D_{i_{-2}}) \cap D_{i_{-1}}$. The set $H_{i_{-2}, i_{-1}, i_0} \subset D_{i_0}$ consists of such points $\mathbf{p}_0 = (u_0, u'_0) \in D_{i_0}$ that the corresponding solution $u(x)$ to the Cauchy problem with initial conditions $u(0) = u_0, u'(0) = u'_0$ does not collapse at $[-2L; 0]$, and $\mathbf{p}_{-1} = (u(-L), u'(-L)) \in D_{i_{-1}}, \mathbf{p}_{-2} = (u(-2L), u'(-2L)) \in D_{i_{-2}}$. That's why the code of solution with initial conditions taken from H_{i_{-2}, i_{-1}, i_0} includes symbols $\{i_{-2}, i_{-1}, i_0\}$.

In order to formalize this process we introduce an arrow operator $X \xrightarrow{\mathcal{P}} Y = \mathcal{P}(X) \cap Y$. This operator is not associative and should be applied strictly from left to right, i.e. $X \xrightarrow{\mathcal{P}} Y \xrightarrow{\mathcal{P}} Z = (\mathcal{P}(X) \cap Y) \xrightarrow{\mathcal{P}} Z$. Consider a sequence of nested sets:

$$\begin{aligned}
D_{i_0} &\supseteq H_{i_0} &= D_{i_0}; \\
D_{i_0} &\supseteq H_{i_{-1}, i_0} &= D_{i_{-1}} \xrightarrow{\mathcal{P}} D_{i_0}; \\
D_{i_0} &\supseteq H_{i_{-2}, i_{-1}, i_0} &= D_{i_{-2}} \xrightarrow{\mathcal{P}} D_{i_{-1}} \xrightarrow{\mathcal{P}} D_{i_0}; \\
D_{i_0} &\supseteq H_{i_{-3}, i_{-2}, i_{-1}, i_0} &= D_{i_{-3}} \xrightarrow{\mathcal{P}} D_{i_{-2}} \xrightarrow{\mathcal{P}} D_{i_{-1}} \xrightarrow{\mathcal{P}} D_{i_0}; \\
&\dots
\end{aligned} \tag{2.54}$$

All of them are situated inside the island D_{i_0} , moreover all of sets H_{i_{-k}, \dots, i_0} are non-empty due to completeness of the island set \mathcal{U}_L . Consider an intersection of these sets $H_\infty = \bigcap_{k=0}^{\infty} H_{i_{-k}, \dots, i_0}$. By the construction resulting set H_∞ , if non-empty, consists of such points that the corresponding solution with initial conditions $u(0) = u_0, u'(0) = u'_0, (u_0, u'_0) \in H_\infty$, exists on the interval $(-\infty; 0]$ and its code coincide

with the left part of the initially considered sequence \mathbf{s} .

Let's do the similar operations with the right part of \mathbf{s} : $\{i_0, i_1, i_2, \dots\}$. Consider a sequence of nested sets:

$$\begin{aligned} D_{i_0} \supseteq V_{i_0} &= D_{i_0}; \\ D_{i_0} \supseteq V_{i_0, i_1} &= D_{i_1} \xrightarrow{\mathcal{P}^{-1}} D_{i_0}; \\ D_{i_0} \supseteq V_{i_0, i_1, i_2} &= D_{i_2} \xrightarrow{\mathcal{P}^{-1}} D_{i_1} \xrightarrow{\mathcal{P}^{-1}} D_{i_0}; \\ D_{i_0} \supseteq V_{i_0, i_1, i_2, i_3} &= D_{i_3} \xrightarrow{\mathcal{P}^{-1}} D_{i_2} \xrightarrow{\mathcal{P}^{-1}} D_{i_1} \xrightarrow{\mathcal{P}^{-1}} D_{i_0}; \\ &\dots \end{aligned}$$

All of these nested sets V_{i_0, \dots, i_k} are situated inside the island D_{i_0} and are non-empty. Consider an intersections $V_\infty = \bigcap_{k=0}^{\infty} V_{i_0, \dots, i_k}$. Set V_∞ , if non-empty, consists of such points that solution with initial conditions from V_∞ exists on the interval $[0; +\infty)$ and its code coincide with the right part of \mathbf{s} .

Intersection of these two sets $H_\infty \cap V_\infty$ consists of such points of initial conditions that gives the result regular solutions with the desired code \mathbf{s} . The geometry of $H_\infty \cap V_\infty$ can be quite complex. But if the intersection consists of just one point then we can say that the code identifies a solution uniquely.

Our goal is to formulate sufficient conditions that allows us to state that any bi-infinite code identify a regular solution uniquely. Again let \mathcal{U}_L represent a complete island set for equation of type (2.1). Consider the sequences of nested sets:

$$\begin{aligned} \mathcal{U}_L &= \mathcal{H}_0 \supseteq \mathcal{H}_1 \supseteq \mathcal{H}_2 \supseteq \mathcal{H}_3 \supseteq \dots, \quad \mathcal{H}_i = \mathcal{P}(\mathcal{H}_{i-1}) \cap \mathcal{H}_0; \\ \mathcal{U}_L &= \mathcal{V}_0 \supseteq \mathcal{V}_1 \supseteq \mathcal{V}_2 \supseteq \mathcal{V}_3 \supseteq \dots, \quad \mathcal{V}_i = \mathcal{P}^{-1}(\mathcal{V}_{i-1}) \cap \mathcal{V}_0. \end{aligned}$$

Define the following sets as intersections of the sequences above:

$$\begin{aligned} \mathcal{H}_\infty &= \mathcal{H}_0 \cap \mathcal{H}_1 \cap \mathcal{H}_2 \cap \mathcal{H}_3 \cap \dots; \\ \mathcal{V}_\infty &= \mathcal{V}_0 \cap \mathcal{V}_1 \cap \mathcal{V}_2 \cap \mathcal{V}_3 \cap \dots. \end{aligned}$$

By its construction their intersection $\mathcal{U}_\infty = \mathcal{H}_\infty \cap \mathcal{V}_\infty$ contains initial conditions for all regular solutions of equation (2.1). Set \mathcal{U}_∞ is a central object for describing

of the set of regular solutions for equation of such type [8, 7, 12]. Its structure may be quite sophisticated having a form of a complex fractal set. One can have a nice illustration on how this set may look like for equation (2.12). For that purpose we combine Figure 2.11 and Figure 2.12 into a single plot.

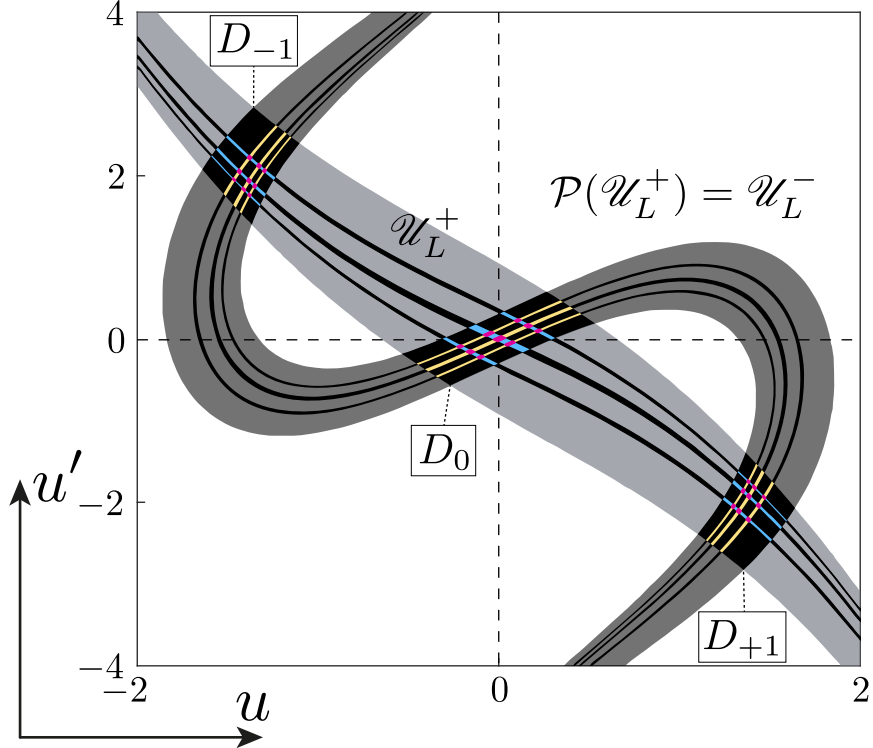


Figure 2.14. Subsets of \mathcal{H}_1 (yellow) and \mathcal{V}_1 (blue), and their intersection $\mathcal{H}_1 \cap \mathcal{V}_1$ (magenta). This figure give an illustration on how the partitioning inside the set \mathcal{U}_L (black) starts to occur while considering higher orders of \mathcal{P} and \mathcal{P}^{-1} .

In Figure 2.14 subsets of \mathcal{H}_1 (yellow) and \mathcal{V}_1 (blue) along with their intersection $\mathcal{H}_1 \cap \mathcal{V}_1$ (magenta) are presented. There exist other parts of \mathcal{H}_1 and \mathcal{V}_1 that can be obtained by considering \mathcal{P} and \mathcal{P}^{-1} -images of other islands lying outside of the scanning area, but we exclude them for the sake of clarity. One can see how the partitioning inside the \mathcal{U}_L occurs. Continuation of that process with higher orders of maps \mathcal{P} and \mathcal{P}^{-1} results in additional partitioning inside the set $\mathcal{H}_1 \cap \mathcal{V}_1$ and reveals the complex nature of the set \mathcal{U}_∞ . Eventually if for each code there exists exactly one point of initial conditions in the set \mathcal{U}_∞ then we can state the existence of one-to-one correspondence between regular solutions and symbolic sequences derived from the structure of the set \mathcal{U}_L . Let's now formulate the sufficient conditions of

that. We do this in a form of two hypotheses which are of the form of so-called Conley–Moser conditions [13, Chapter 25].

Hypothesis I. *For equation (2.1) with L -periodic functions $Q(x)$, $P(x)$ the set \mathcal{U}_L is a complete island set, $\mathcal{U}_L = \bigcup_{i \in S} D_i$, and there exist constants M, N such that $d_h(D_i) \leq M$ and $d_v(D_i) \leq N$ for any $i \in S$.*

Hypothesis II. *Let $\mathcal{U}_L = \bigcup_{i \in S} D_i$ be an island set. For each $i, j \in S$ there exist γ_{ij} such that for any h-strip $H \in D_i$ its \mathcal{P} -image $\tilde{H}_j = \mathcal{P}(H) \cap D_j$ is an $h_{\gamma_{ij}}$ -strip, and there exists $\mu > 1$ such that*

$$d_h(\tilde{H}_j) \leq (1/\mu)d_h(H). \quad (2.55)$$

For each $i, j \in S$ there exist δ_{ij} such that for any v-strip $V \in D_j$ its \mathcal{P} -pre-image $\tilde{V}_i = \mathcal{P}^{-1}(V) \cap D_i$ is a $v_{\delta_{ij}}$ -strip, and there exists $\nu > 1$ such that

$$d_v(\tilde{V}_i) \leq (1/\nu)d_v(V). \quad (2.56)$$

Two hypotheses introduced above allow us to formulate and prove the central theorem (Theorem 1) of our coding approach. This theorem partially reproduce the result initially proved in [8, Theorem 3.1]. However Theorem 1 turns out to be more suitable for further numerical analysis, since we excluded Hypothesis III from [8] and replaced it with modified version of Hypothesis II. Hypothesis III from [8] requires a sophisticated analyses of areas of sets D_i in plane which is hard to perform numerically.

Theorem 1. *Assume that Poincaré map associated with equation (2.1) satisfies Hypotheses I and II. Then there exists a homeomorphism of topological spaces* $\mathcal{C} : \mathcal{O} \rightarrow \mathcal{S}$, defined as follows: $\mathcal{C}(\mathbf{r}) = \mathbf{s}$, $\mathbf{r} \in \mathcal{O}$, $\mathbf{r} = \{\mathbf{p}_k\}$ and $\mathbf{s} \in \mathcal{S}$, $\mathbf{s} = \{i_k\}$, such that i_k is the number of the component $D_{i_k} \in \mathcal{U}_L$ where the point \mathbf{p}_k lies.*

*We use the symbol \mathcal{C} for the homeomorphism since it reminds the overall process as “coding”.

Proof. Evidently, for each bi-infinite orbit $\mathbf{r} \in \mathcal{O}$ of regular solution the image $\mathbf{s} = \mathcal{C}(\mathbf{r})$, $\mathbf{s} \in \mathcal{S}$ is defined uniquely. Let's prove that for each sequence $\mathbf{s} \in \mathcal{S}$ there exist unique orbit $\mathbf{r} \in \mathcal{O}$ such that $\mathbf{s} = \mathcal{C}(\mathbf{r})$.

Consider a sequence $\mathbf{s} = \{\dots, i_{-1}, i_0, i_1, \dots\}$. Let's find a location of the points $\mathbf{p} \in D_{i_0}$ such that $\mathcal{P}^{-1}(\mathbf{p}) \in D_{i_{-1}}$, $\mathcal{P}^{-2}(\mathbf{p}) \in D_{i_{-2}}$, etc. First of all, D_{i_0} is a γ_{i_0} -island, then it's an $h_{\gamma_{i_0}}$ -strip. Define an $h_{\gamma_{i_0}}$ -strip $H_{i_0} = D_{i_0}$ as a base step. From Hypothesis I we conclude that

$$d_h(H_{i_0}) \leq M. \quad (2.57)$$

Points $\mathbf{p} \in D_{i_0}$ such that $\mathcal{P}^{-1}(\mathbf{p}) \in D_{i_{-1}}$ are situated in the set $H_{i_{-1}, i_0} = \mathcal{P}(D_{i_{-1}}) \cap D_{i_0}$. Due to Hypothesis II set H_{i_{-1}, i_0} is an $h_{\gamma_{i_0, i_{-1}}}$ -strip. Its thickness satisfies an inequality

$$d_h(H_{i_{-1}, i_0}) \leq \mu^{-1} d_h(H_{i_0}) \leq \mu^{-1} M. \quad (2.58)$$

For simplicity define $\gamma = \max\{\gamma_{i_0}, \gamma_{i_0, i_{-1}}\}$.

Points $\mathbf{p} \in D_{i_0}$ such that $\mathcal{P}^{-1}(\mathbf{p}) \in D_{i_{-1}}$, $\mathcal{P}^{-2}(\mathbf{p}) \in D_{i_{-2}}$ are situated in the set $H_{i_{-2}, i_{-1}, i_0} = \mathcal{P}(H_{i_{-2}, i_{-1}}) \cap D_{i_0}$ where $H_{i_{-2}, i_{-1}} = \mathcal{P}(D_{i_{-2}}) \cap D_{i_{-1}}$. By Hypothesis II set $H_{i_{-2}, i_{-1}}$ is an h -strip. Hence, set H_{i_{-2}, i_{-1}, i_0} is an h_γ -strip and its thickness satisfies an inequality

$$d_h(H_{i_{-2}, i_{-1}, i_0}) \leq \mu^{-1} d_h(H_{i_{-2}, i_{-1}}) \leq \mu^{-2} d_h(D_{i_{-2}}) \leq \mu^{-2} M. \quad (2.59)$$

Continuation of that process leads us to the sequence of nested h_γ -strips similar to what we had in (2.54):

$$D_{i_0} = H_{i_0} \supseteq H_{i_{-1}, i_0} \supseteq H_{i_{-2}, i_{-1}, i_0} \supseteq \dots \quad (2.60)$$

Let's show that the infinite intersection of the h_γ -strips (2.60) is an h_γ -curve. Sequence of their thicknesses is bounded from above with a decreasing sequence $\{\mu^{-n} M\}$, $n = 0, 1, 2, \dots$. Value $\mu > 1$, so the limit $\lim_{n \rightarrow \infty} \mu^{-n} M = 0$. Now consider boundaries of the strips (2.54) as a functions of u . All of them are γ -Lipschitz functions. Their

domains are different, but all of them lie inside the domain Δ , defined as

$$\Delta = \text{dom}(\alpha_{i_0}^+) \cup \text{dom}(\alpha_{i_0}^-), \quad (2.61)$$

where $\alpha_{i_0}^\pm$ are opposite boundaries of the first strip H_{i_0} . We can continue each α^\pm boundary of h-strips (2.54) onto the whole Δ . Let $\alpha_{i_{-k}, \dots, i_0}^\pm$ be a boundaries of an h-strip H_{i_{-k}, \dots, i_0} . They can be considered as a functions of u , $u' = h_{i_{-k}, \dots, i_0}^\pm(u)$ with the domains $\Delta_{i_{-k}, \dots, i_0}^\pm = [a_{i_{-k}, \dots, i_0}^\pm; b_{i_{-k}, \dots, i_0}^\pm]$, and we can define new functions

$$\tilde{h}_{i_{-k}, \dots, i_0}^\pm(u) = \begin{cases} h_{i_{-k}, \dots, i_0}^\pm(a_{i_{-k}, \dots, i_0}^\pm) & u < a_{i_{-k}, \dots, i_0}^\pm; \\ h_{i_{-k}, \dots, i_0}^\pm(u) & u \in \Delta_{i_{-k}, \dots, i_0}^\pm; \\ h_{i_{-k}, \dots, i_0}^\pm(b_{i_{-k}, \dots, i_0}^\pm) & u > b_{i_{-k}, \dots, i_0}^\pm. \end{cases} \quad (2.62)$$

Such extension allows us to treat boundaries of H_{i_{-k}, \dots, i_0} as functions of u with the same domain and consider them as a part of the space $C_\gamma(\Delta)$ of γ -Lipschitz functions defined on the interval Δ . Definition of the h-strip thickness coincide with the metric defined by the maximum norm, and $C_\gamma(\Delta)$ is a complete metric space [14]. Now consider the sequence

$$\{\tilde{h}_{i_0}^+(u), \tilde{h}_{i_0}^-(u), \tilde{h}_{i_{-1}, i_0}^+, \tilde{h}_{i_{-1}, i_0}^-, \dots, \tilde{h}_{i_{-k}, \dots, i_0}^+, \tilde{h}_{i_{-k}, \dots, i_0}^-, \dots\}. \quad (2.63)$$

Since $H_{i_{-k}, \dots, i_0} \subseteq H_{i_{-k+1}, \dots, i_0}$ and $d_h(H_{i_{-k}, \dots, i_0}) \rightarrow 0$ as $k \rightarrow \infty$, sequence (2.63) is a Cauchy sequence. Therefore, since $C_\gamma(\Delta)$ is a complete metric space, the Cauchy sequence converges to a unique curve $\tilde{h}_\infty(u)$ which represents an h_γ -curve inside the island D_{i_0} . Since we extend h-strips boundaries onto the whole Δ there may be other parts of $\tilde{h}_\infty(u)$ lying outside of D_{i_0} . Denote by α_∞ a part of $\tilde{h}_\infty(u)$ that entirely belongs to D_{i_0} . This curve is the intersection of the h_γ -strips (2.60) and is an h_γ -curve.

In the same manner a sequence of nested v_δ -strips can be constructed,

$$D_{i_0} = V_{i_0} \supseteq V_{i_0, i_1} \supseteq V_{i_0, i_1, i_2} \supseteq \dots \quad (2.64)$$

Their thicknesses are bounded from above with a decreasing sequence $\{\nu^{-n}N\}$, $n = 0, 1, 2, \dots$ of a zero limit, $\lim_{n \rightarrow \infty} \nu^{-n}N = 0$. Considering a corresponding sequence

of δ -Lipschitz functions we conclude that the intersection of the strips (2.64) exists and is a v_δ -curve. Denote this curve by β_∞ .

The orbit $\mathbf{r} \in \mathcal{O}$ corresponding to the bi-infinite sequence $\{\dots, i_{-1}, i_0, i_1, \dots\}$ is generated by \mathcal{P} and \mathcal{P}^{-1} -iterations of the intersection $\alpha_\infty \cap \beta_\infty$ which according to the definitions of h- and v-curves *consists of one point*. Therefore orbit \mathbf{r} exists and is unique.

The continuity of \mathcal{C} and \mathcal{C}^{-1} maps follows from an observation that follows below. Since \mathcal{P} is continuous, if $\mathbf{r}^{(1)}, \mathbf{r}^{(2)} \in \mathcal{O}$,

$$\begin{aligned}\mathbf{r}^{(1)} &= \{\dots, \mathbf{p}_{-1}^{(1)}, \mathbf{p}_0^{(1)}, \mathbf{p}_1^{(1)}, \dots\}, \\ \mathbf{r}^{(2)} &= \{\dots, \mathbf{p}_{-1}^{(2)}, \mathbf{p}_0^{(2)}, \mathbf{p}_1^{(2)}, \dots\};\end{aligned}$$

are close enough in \mathcal{O} (i.e. points $\mathbf{p}_0^{(1)}$ and $\mathbf{p}_0^{(2)}$ are close in \mathbb{R}^2), then their \mathcal{C} -images share the same central block $|k| < n$ for some n . Therefore they are also close in \mathcal{S} -topology. If $\mathbf{s}^{(1)} = \mathcal{C}(\mathbf{p}^{(1)})$ and $\mathbf{s}^{(2)} = \mathcal{C}(\mathbf{p}^{(2)})$ share the same central block $|k| < n$ for some n then the points $\mathbf{p}_0^{(1)}$ and $\mathbf{p}_0^{(2)}$ are situated in the same area $H_{i_{-k}, \dots, i_k} \cap V_{i_0, \dots, i_k}$, so $\mathbf{p}_0^{(1)}$ and $\mathbf{p}_0^{(2)}$ are close in \mathcal{O} -topology. Theorem is proven. \square

2.5. Numerical Test of Existence of Coding Homeomorphism

In order to apply Theorem 1 to equation (2.1) one should get a strong evidence that Hypotheses I and II are valid. However it's rather difficult to obtain a rigorous mathematical proof of them even for the simplest form of the functions $Q(x)$, $P(x)$ in (2.1). Instead, in our current work we provide a computing procedure that allows to check numerically that Hypotheses I and II are valid at least at finite domain of plane of initial conditions. Hypothesis I can be verified in a straightforward way, since we can apply the scanning procedure and get a structure of the set \mathcal{U}_L . There may be two possible scenarios.

The first scenario is when we can prove that the set \mathcal{U}_L is bounded within a finite domain, like the authors of the work [8] did for $P(x) \equiv -1$. Then one can

apply a scanning procedure to that domain and thus provide a numerical evidence that Hypothesis I holds for the whole set \mathcal{U}_L .

The second scenario is when we cannot prove any statement on the boundaries and structure of \mathcal{U}_L , or this set is infinite and unbounded. For example, we saw previously that for equation (2.12) set \mathcal{U}_L is unbounded. In that case we cannot compute the whole set \mathcal{U}_L , since it's possible to scan only a finite subset of the initial conditions plane. But if the finite subset of \mathcal{U}_L represents an island set of N islands, the coding approach still can be possibly applied. Let's denote $\mathcal{D}_N = \bigcup_{k \in S_N} D_k$ the finite subset of N islands from \mathcal{U}_L , obtained by the scanning procedure. We can reduce our consideration to regular solutions which orbits visit only islands from \mathcal{D}_N . Let $\mathcal{O}_N \subset \mathcal{O}$ denote a subset of such orbits. If Hypothesis II is valid for the \mathcal{D}_N , we can conclude that conditions of Theorem 1 are met and there exists a homeomorphism between a *subset of orbits of regular solutions* \mathcal{O}_N and set of bi-infinite sequences \mathcal{S}_N of symbols from finite set S_N .

Hypothesis II does not admit straightforward numerical verification by itself. However, it can be reduced to another two statements, called Strips Mapping Theorems, which admit numerical verification. These statements rely on properties of linear operators $D\mathcal{P}_{\mathbf{p}}$, $D\mathcal{P}_{\mathbf{p}}^{-1}$, which are represented by the Jacobi matrices of \mathcal{P} and \mathcal{P}^{-1} ,

$$\mathcal{P}(\mathbf{q}) = \mathcal{P}(\mathbf{p}) + D\mathcal{P}_{\mathbf{p}}(\mathbf{q} - \mathbf{p}) + o(||\mathbf{q} - \mathbf{p}||); \quad (2.65)$$

$$\mathcal{P}^{-1}(\mathbf{q}) = \mathcal{P}^{-1}(\mathbf{p}) + D\mathcal{P}_{\mathbf{p}}^{-1}(\mathbf{q} - \mathbf{p}) + o(||\mathbf{q} - \mathbf{p}||). \quad (2.66)$$

Let's formulate the first statement that cover a part of Hypothesis I related to the h-strips mapping.

Theorem 2 (On h-strips mapping). *Let Poincaré map \mathcal{P} and its inverse \mathcal{P}^{-1} be defined on a complete (see Definition 8) island set $\bigcup_{i \in S} D_i$, where S is a finite or countable set of indices. Let for all $i, j \in S$ the set $V_{ij} = \mathcal{P}^{-1}(D_j) \cap D_i$ is non-empty, \mathcal{P} is defined on a closure $\overline{V_{ij}}$, and one of the following two conditions holds:*

(1) the borders α_i^\pm of an island D_i are increasing curves, $\forall \mathbf{p} \in \overline{V_{ij}}$ the signs of $\{a_{mn}\}$ in the matrix of the linear operator $D\mathcal{P}_{\mathbf{p}} = (a_{mn})$ have exactly one of the following configurations[†]:

$$(a) (+ +), \quad (b) (- -), \quad (c) (+ +), \quad (d) (- -);$$

and at the same time the borders α_j^\pm of D_j are increasing curves for cases (a), (b), and decreasing curves for (c), (d);

(2) the borders α_i^\pm of an island D_i are decreasing curves, $\forall \mathbf{p} \in \overline{V_{ij}}$ signs of $\{a_{mn}\}$ in the matrix of the linear operator $D\mathcal{P}_{\mathbf{p}} = (a_{mn})$ have exactly one of the following configurations:

$$(a) (+ -), \quad (b) (- +), \quad (c) (+ -), \quad (d) (- +);$$

and at the same time borders α_j^\pm of D_j are decreasing curves for cases (a), (b), and increasing for (c), (d);

and moreover $\exists \mu > 1$ such that $\forall p \in \overline{V_{ij}}, |a_{11}| \geq \mu$. Then

- (i) for any h-strip $H \in D_i$, $\mathcal{P}(H) \cap D_j = \tilde{H}_j$ is also an h-strip;
- (ii) $d_h(\tilde{H}_j) \leq (1/\mu)d_h(H)$ (here $d_h(\cdot)$ is an h-strip thickness in a sense of Definition 9).

Proof of Theorem 2 can be found in Appendix C. Basically, this theorem postulates two following things:

- If linear operator $D\mathcal{P}_{\mathbf{p}} = (a_{mn})$, $\mathbf{p} \in V_{ij}$, satisfies some conditions about signs of a_{mn} , then \mathcal{P} maps h-strips to h-strips.
- If for the linear operator $D\mathcal{P}_{\mathbf{p}} = (a_{mn})$ the estimation $|a_{11}| \geq \mu > 1$, takes place for $\mathbf{p} \in V_{ij}$ ($\exists \mu$), then \mathcal{P} shrinks thickness of h-strips.

[†]By “+” and “-” sign we mean strict inequalities $a_{mn} > 0$, $a_{mn} < 0$ to be held.

The next theorem establish the similar properties for the v-strips mapping.

Theorem 3 (On v-strips mapping). *Let Poincaré map \mathcal{P} and its inverse \mathcal{P}^{-1} be defined on a complete (see Definition 8) island set $\bigcup_{i \in S} D_i$, where S is a finite or countable set of indices. Let for all $i, j \in S$ the set $H_{ij} = \mathcal{P}(D_i) \cap D_j$ is non-empty, \mathcal{P}^{-1} is defined on a closure $\overline{H_{ij}}$, and one of the following two conditions holds:*

- (1) *the borders β_j^\pm of an island D_j are increasing curves, $\forall \mathbf{q} \in \overline{H_{ij}}$ the signs of $\{b_{mn}\}$ in the matrix of the linear operator $D\mathcal{P}_{\mathbf{q}}^{-1} = (b_{mn})$ have exactly one of the following configurations:*

$$(a) (+ +), \quad (b) (- -), \quad (c) (+ -), \quad (d) (- +);$$

and at the same time the borders β_i^\pm of D_i are increasing curves for cases (a), (b), and decreasing curves for (c), (d);

- (2) *the borders β_j^\pm of an island D_j are decreasing curves, $\forall \mathbf{q} \in \overline{H_{ij}}$ the signs of $\{b_{mn}\}$ in the matrix of the linear operator $D\mathcal{P}_{\mathbf{q}}^{-1} = (b_{mn})$ have exactly one of the following configurations:*

$$(a) (+ -), \quad (b) (- +), \quad (c) (+ -), \quad (d) (- +);$$

and at the same time borders β_i^\pm of D_i are decreasing curves for cases (a), (b), and increasing for (c), (d);

and moreover $\exists \nu > 1$ such that $\forall q \in \overline{H_{ij}}, |b_{22}| \geq \nu$. Then

- (i) *for any v-strip $V \in D_j$, $\mathcal{P}^{-1}(V) \cap D_i = \tilde{V}_i$ is also a v-strip;*
- (ii) *$d_v(\tilde{V}_i) \leq (1/\nu)d_v(V)$ (here $d_v(\cdot)$ is an v-strip thickness in a sence of Definition 11).*

Proof of this theorem is analogous to the previous one and can be performed in the same manner with minor adjustments. Similarly, this theorem postulate two following things:

- If linear operator $D\mathcal{P}_{\mathbf{q}}^{-1} = (b_{mn})$, $\mathbf{q} \in H_{ij}$, satisfies *some conditions* about signs of b_{mn} , then \mathcal{P}^{-1} maps v-strips to v-strips.
- If for the linear operator $D\mathcal{P}_{\mathbf{q}}^{-1} = (b_{mn})$ the estimation $|b_{22}| \geq \nu > 1$ takes place for $\mathbf{q} \in H_{ij}$ ($\exists \nu$), then \mathcal{P}^{-1} shrinks thickness of v-strips.

The great advantage of Theorems 2 and 3 is that linear operators $D\mathcal{P}_{\mathbf{p}}$ and $D\mathcal{P}_{\mathbf{q}}^{-1}$ can be constructed numerically. After that the conditions of the theorems above can be verified via the numerical grid in a finite area of plane of initial conditions. That allows to turn theorems on h- and v-strips mapping into a numerical algorithm of Hypothesis II verification, see Algorithm 1.

Algorithm 1. Numerical Check of Hypothesis II

Input: Hypothesis I takes place for the complete island set $\mathcal{D}_N = \bigcup_{k \in S_N} D_k$.

Step (1). For all $i, j \in S_N$ construct numerically sets $H_{ij} = \mathcal{P}(D_i) \cap D_j$, and $V_{ij} = \mathcal{P}^{-1}(D_j) \cap D_i$.

Step (2). Signs verification.

- For each point $\mathbf{p} \in V_{ij}$ of numerical grid compute 2×2 matrix $D\mathcal{P}_{\mathbf{p}} = (a_{mn})$ and check signs of a_{mn} along the conditions of Theorem 2.
- For each point $\mathbf{q} \in H_{ij}$ of numerical grid compute 2×2 matrix $D\mathcal{P}_{\mathbf{q}}^{-1} = (b_{mn})$ and check signs of b_{mn} along the conditions of Theorem 3.

Step (3). Numerical estimation of values μ, ν .

- Using the numerical grid compute an estimation $\mu_* = \min_{\mathbf{p} \in V_{ij}} a_{11}(\mathbf{p})$; check that $\mu_* > 1$.
 - Using the numerical grid compute an estimation $\nu_* = \min_{\mathbf{q} \in H_{ij}} b_{22}(\mathbf{q})$; check that $\nu_* > 1$.
-

If the verification provided by the steps above is successful then one have a numerical evidence that Hypothesis II is valid. Hence, accordingly to Theorem 1, there exists a homeomorphism \mathcal{C} between orbits of regular solutions \mathcal{O}_N and bi-infinite sequences \mathcal{S}_N of symbols from S_N . Let us illustrate this idea for the considered

equation (2.12) with the parameters $(L_*, L_0) = (2, 1)$. Applying of the technique above can be summarized within a picture, see Figure 2.15.

In Figure 2.15 three-islands set $\mathcal{D}_3 = \{D_{-1}, D_0, D_{+1}\}$ is presented. All three connected components have monotonic boundaries, so they satisfy Hypothesis I. Sets $H_{ij} = \mathcal{P}(D_i) \cap D_j$ and $V_{ij} = \mathcal{P}^{-1}(D_j) \cap D_i$ are constructed numerically. Matrix $D\mathcal{P}_{\mathbf{p}} = (a_{mn})$ is computed in each point $\mathbf{p} \in V_{ij}$. Signs of a_{mn} are depicted in Figure 2.15 with small matrices right after each V_{ij} label. Values a_{mn} satisfy the conditions of Theorem 2. Indeed, consider a pair of islands D_0 and D_{+1} . Signs of a_{mn} have the same configurations (— —) for the whole set $V_{0,+1}$. Boundaries α_0^\pm of islands D_0 are the parts of boundaries of \mathcal{U}_L^- (dark-gray) and represent increasing curves. Boundaries α_{+1}^\pm are also increasing. This means that condition (1b) of Theorem 2 is satisfied and for any h-strip $H \in D_0$, it's \mathcal{P} -image $\mathcal{P}(H) \cap D_{+1} = \tilde{H}_{+1}$ is also an h-strip within island D_{+1} . Other pairs of islands are considered in the same way.

Similarly, $D\mathcal{P}_{\mathbf{q}}^{-1} = (b_{mn})$ is computed in each point $\mathbf{q} \in H_{ij}$. Signs of b_{mn} are depicted right after each H_{ij} label. One can check, that such sings configuration satisfy the conditions of Theorem 3.

The lower boundary of $|a_{11}(\mathbf{p})|$ values is $\mu_* = 4.648$. It's computed for $\mathbf{p} \in V_{ij}$, $i, j \in \{-1, 0, +1\}$. The corresponding histogram of a_{11} values (blue histogram) is presented in Figure 2.15. The computed lower boundary of $|b_{22}(\mathbf{q})|$, $\mathbf{q} \in H_{ij}$, $i, j \in \{-1, 0, +1\}$ is $\nu_* = 4.676$ (yellow histogram). Both μ_* and ν_* are greater than 1. Hence, the corresponding conditions of Theorem 2 and 3 are satisfied and \mathcal{P} shrinks thickness of h-strips, while \mathcal{P}^{-1} shrinks thickness of v-strips. This completes the verification of Hypothesis II.

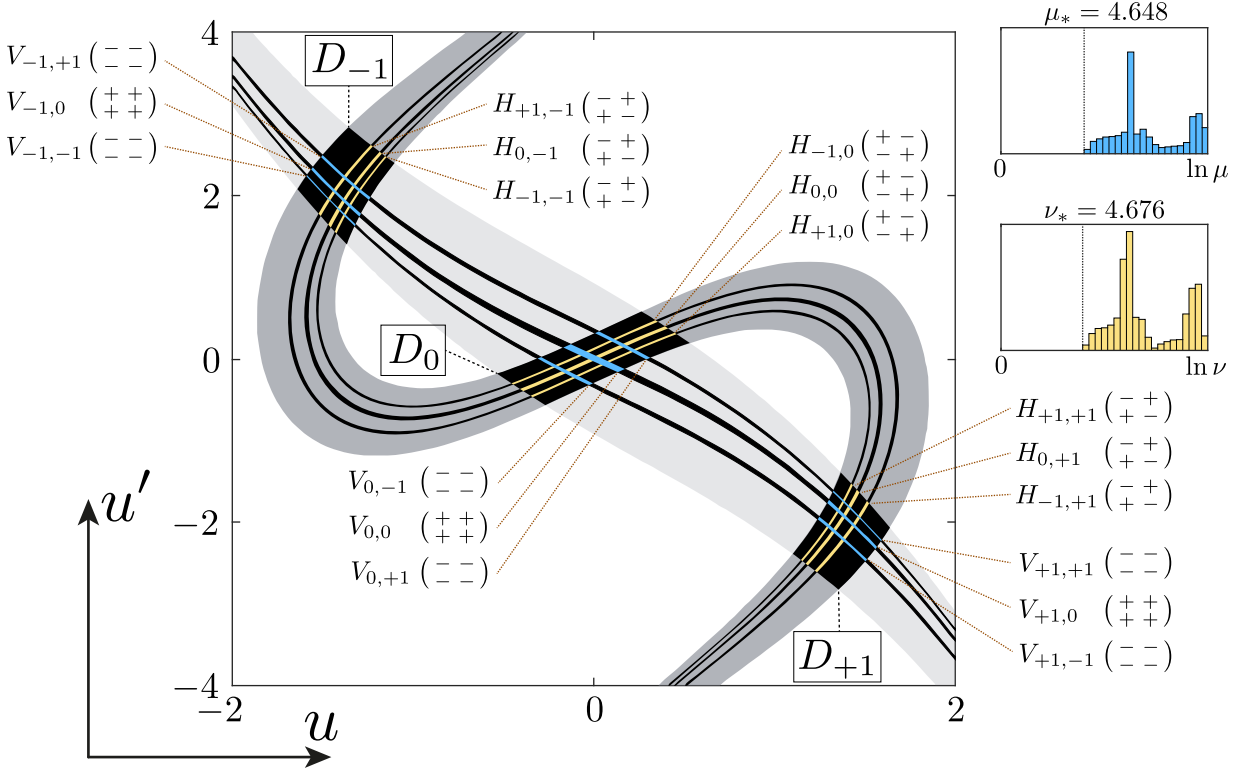


Figure 2.15. Illustration to the verification of Hypothesis II for equation (2.12) with parameters $(L_*, L_0) = (2, 1)$ for three-component island set $\mathcal{D}_3 = \{D_{-1}, D_0, D_{+1}\}$.

2.6. Stationary Solutions of GPE with Piecewise Pseudopotential

Let's demonstrate how coding of solutions can be used to identify classes of different solutions. For that purpose we use again Eq. (2.12) with the parameters $(L_*, L_0) = (2, 1)$. We have shown previously that there exists a numerical evidence that Hypotheses I and II are valid for three central islands. We checked them for a larger number of connected component as well, like 5, 7, and 9 central islands, and saw that the hypotheses remain valid. Let's now restrict our consideration by the first five central components D_i , $i \in \{-2, -1, 0, +1, +2\}$ of the island set \mathcal{U}_L . Since our numerical analysis shown that both Hypothesis I and II are valid, Theorem 1 can be applied. It allows to conclude that there exists a homeomorphism between a subset of regular solutions and the set \mathcal{S}_5 .

Such correspondence allows us to make conclusion on different types of regular solutions of equation (2.12). For example, there exist periodic solutions of a

period nL for any number $n \in \mathbb{N}$. Their symbolic codes have a periodic structure $\{\dots, i_0, \dots, i_n, i_0, \dots, i_n, \dots\}$. There also exist localized solutions of different shapes. Their symbolic codes have a central block of non-zero symbols, and all other symbols on the left and right sides of this block are “0”, $\{\dots, 0, 0, i_0, \dots, i_n, 0, 0, \dots\}$. Regular solution of the domain wall shapes can also be found. They are coded with sequences which has “0” symbols only on the left or on the right side, $\{\dots, 0, 0, i_0, i_1, \dots\}$, $\{\dots, i_{-1}, i_0, 0, 0, \dots\}$.

Several periodic and localized solutions are presented in Figure 2.16. Numerical computation of solution by its code in a general case is a separate complex task. Nevertheless localized solutions can be found by the shooting method, and periodic solutions of a period nL can be found by solving the nonlinear equation $\mathbf{p} - \mathcal{P}^n(\mathbf{p}) = 0$, $\mathbf{p} \in \mathbb{R}^2$, with properly chosen initial approximation which can be guessed from the \mathcal{U}_L structure. It’s worth to mention here the paper [12] where authors provide an algorithm which allows to reconstruct the profile of localized solution by its code for equation (2.1) with $P(x) \equiv -1$. Presumably an analogous technique can be applied for a periodic pseudopotential $P(x)$.

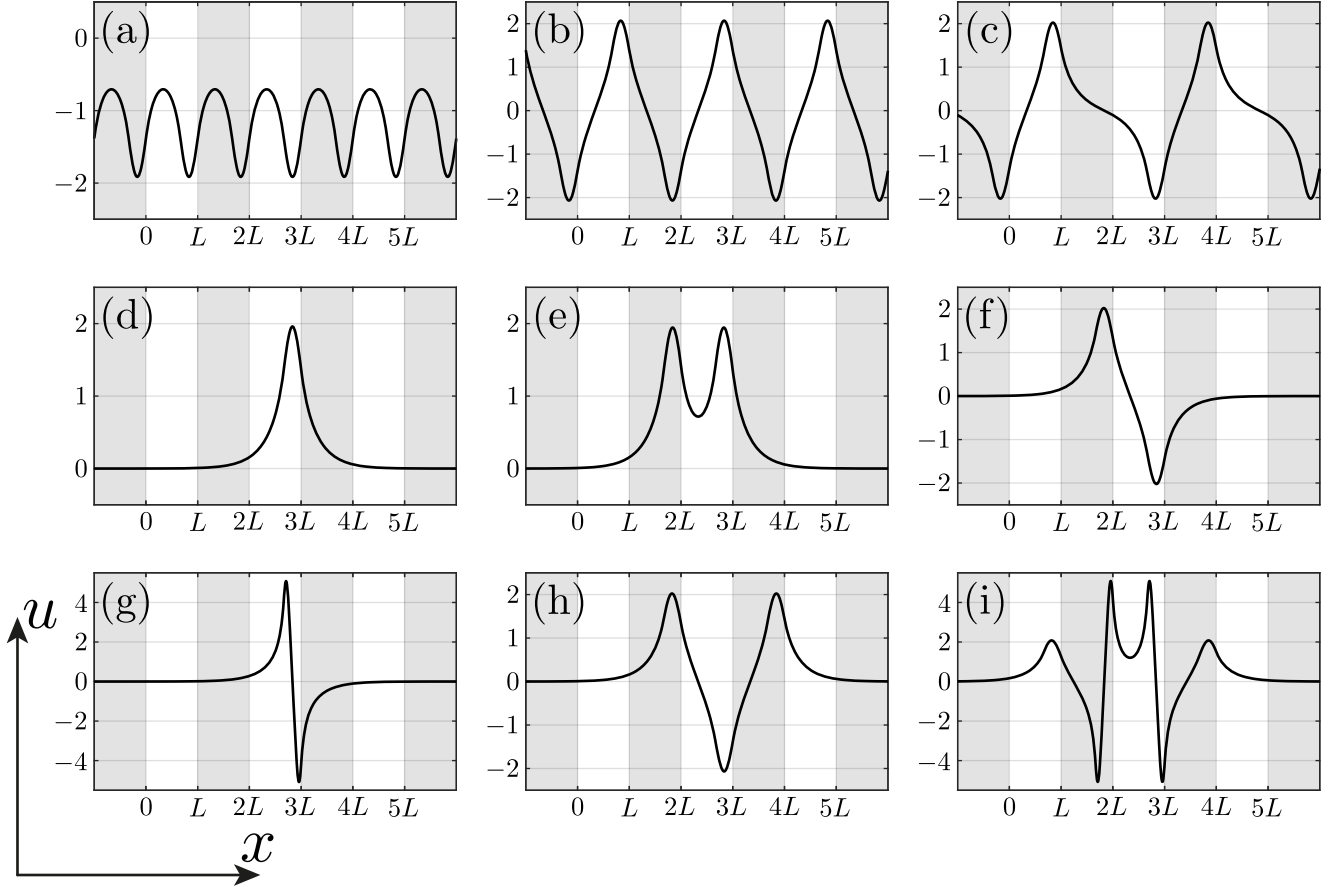


Figure 2.16. Different solutions for equation (2.12) with parameters $(L_*, L_0) = (2, 1)$. Each solution has a corresponding symbolic code, this code identify the solution uniquely. Gray strips divide the x axis according to the period L . First three panels represent periodic solutions, their codes have periodic structure: (a) L -periodic solution $\{\dots, -1, -1, -1, \dots\}$; (b) $2L$ -periodic solution $\{\dots, -1, +1, -1, +1, \dots\}$; (c) $3L$ -periodic solution $\{\dots, -1, +1, 0, -1, +1, 0, \dots\}$. Other six panels represent localized solutions, their codes have “0” symbol to the left and right of the central block: (d) $\{\dots, 0, 0, +1, 0, 0, \dots\}$; (e) $\{\dots, 0, 0, +1, +1, 0, 0, \dots\}$ (f) $\{\dots, 0, 0, +1, -1, 0, 0, \dots\}$ (g) $\{\dots, 0, 0, -2, 0, 0, \dots\}$ (h) $\{\dots, 0, 0, +1, -1, +1, 0, 0, \dots\}$ (i) $\{\dots, 0, 0, +1, +2, -2, +1, 0, 0, \dots\}$.

2.7. Summary

In this chapter the approach for classification of bounded solutions for equation (2.1) has been exposed. This approach is based on the analysis of the dynamics of Poincaré map \mathcal{P} on the set \mathcal{U}_L . It turns out that under some restrictions the map \mathcal{P} is a horseshoe map with finite or infinite number of partitions. This allows us to establish a homeomorphism between orbits of regular solutions of (2.1) and symbolic sequences over some alphabet based on the structure of the set \mathcal{U}_L .

We formulated sufficient conditions for the existence of this homeomorphism in a form of two hypotheses, see Hypotheses I and II. Hypothesis I can be verified numerically in a straightforward way. Hypothesis II requires a more delicate attitude. We replaced Hypothesis II with Theorems 2 and 3, they are proved in Appendix C. These theorems admits numerical verification by Algorithm 1. If all steps of the algorithm above are successful, we can conclude that Hypothesis II takes place.

The elaborated technique was applied to equation (2.12) with the simplest form of periodic pseudopotential $P(x)$. On the example of equation (2.12) we show that the presence of sign-altering periodic pseudopotential results in the existence of a plethora of regular solutions. Such observation allows us we to expect that similar variety of regular solutions is a common property for the overall class of equations (2.1).

Chapter 3

Localized Solutions of Gross-Pitaevskii Equation with Periodic Pseudopotential

3.1. Objectives

In this chapter we apply the coding approach to the Gross-Pitaevskii equation of the form

$$i\Psi_t + \Psi_{xx} - U(x)\Psi + P(x)|\Psi|^2\Psi = 0. \quad (3.1)$$

Here both potential $U(x)$ and pseudopotential $P(x)$ are periodic functions. Such equation occurs in physics of Bose-Einstein condensate (BEC) where periodical pseudopotential is achieved by means of the Feshbach resonance controlled by magnetic or optical fields [1, 2, 3]. Experimentally, the possibility of the periodic modulation of the nonlinearity was demonstrated in [15]. One can also find equation (3.1) in optics where spatial modulation of the Kerr coefficient can be achieved by means of inhomogeneous density of resonant nonlinearity-enhancing dopants implanted into the waveguide [4].

We are interested in stationary localized solutions of equation (3.1), also called as solitons in physical applications. Strictly speaking, the objects that we are going to study are not solitons in the mathematically rigorous meaning, but rather “solitary waves”, as they appear in a nonintegrable model. Nevertheless, the application of the word “soliton” to localized pulses in BECs is commonly adopted in physics literature, therefore we also use this word. Stationary solutions satisfy the ansatz $\Psi(t, x) = u(x)e^{i\omega t}$, where function $u(x)$ is a solution of equation

$$u_{xx} + Q(x)u + P(x)u^3 = 0, \quad Q(x) = -\omega - U(x). \quad (3.2)$$

Localized solutions satisfy the localization condition

$$\lim_{x \rightarrow \pm\infty} u(x) = 0, \quad (3.3)$$

which implies that the function $u(x)$ is real, see [16]. In what follows below we also assume that the potential $U(x)$ is absent, i.e. $U(x) \equiv 0$, so the effects produced by the periodic modulation of the nonlinearity are not obscured by the linear-lattice potential. Prototypical example of periodic pseudopotential is provided by a function

$$P(x) = \alpha + \cos 2x, \quad \alpha \in \mathbb{R}. \quad (3.4)$$

Resulting GPE equation takes form

$$i\Psi_t + \Psi_{xx} + (\alpha + \cos 2x)|\Psi|^2\Psi = 0, \quad (3.5)$$

where the period of pseudopotential function $P(x)$ is scaled to be $L = \pi$. Corresponding stationary state equation is

$$u_{xx} - \omega u + (\alpha + \cos 2x)u^3 = 0. \quad (3.6)$$

Equation (3.5) and (3.6) are the objects of our analysis during this chapter. The same model has been previously discussed in literature, see paper [17]. In [17] only single-peak localized solution, called *fundamental soliton* (FS), was studied in details. For that purpose authors used variational approximation method which requires initial guess of the solution shape. Such limitation does not allow to find more sophisticated localized solutions. By using of our coding technique we are going to reveal significantly wider class of stationary localized solutions of Eq. (3.5).

3.2. Coding of Solutions

Our approach requires the presence of singular solutions families. That's why according to Proposition 2 we assume that $\alpha \in (-1; 1)$, so that function $P(x)$ alternates its sign along the value x . We also assume that $\omega > 0$. This restriction comes from the obvious condition of the soliton localization, given by Eq.(3.3).

Let's introduce a Poincaré map $\mathcal{P} : \mathbb{R}^2 \rightarrow \mathbb{R}^2$ associate with equation (3.6) in the same way we did it before in (2.2) assuming $L = \pi$. Poincaré map \mathcal{P} and its

inverse \mathcal{P}^{-1} is not defined in the whole plane (u, u') of initial conditions. We can construct their domains using the scanning technique introduced in Chapter 2. Sets \mathcal{U}_π^+ and \mathcal{U}_π^- for different parameters (ω, α) are presented in Figure 3.1. Numerical results allow us to conclude that the sets \mathcal{U}_π^\pm are unbounded spirals with infinite number of rotations around the origin, similar to what we saw previously for equation (2.12). According to the Proposition 4 these sets are related with a reflection with respect to the u' axis, i.e. $\mathcal{U}_\pi^- = I\mathcal{U}_\pi^+$. Their thicknesses depend on the parameter α . If these sets are thin enough their intersection $\mathcal{U}_\pi = \mathcal{U}_\pi^+ \cap \mathcal{U}_\pi^-$ form an island set. In Figure 3.1 panels (a), (b), and (c) resulting set \mathcal{U}_π cannot be regarded as island set. In panel (d) \mathcal{U}_π is a seven-component island set in the scanning area.

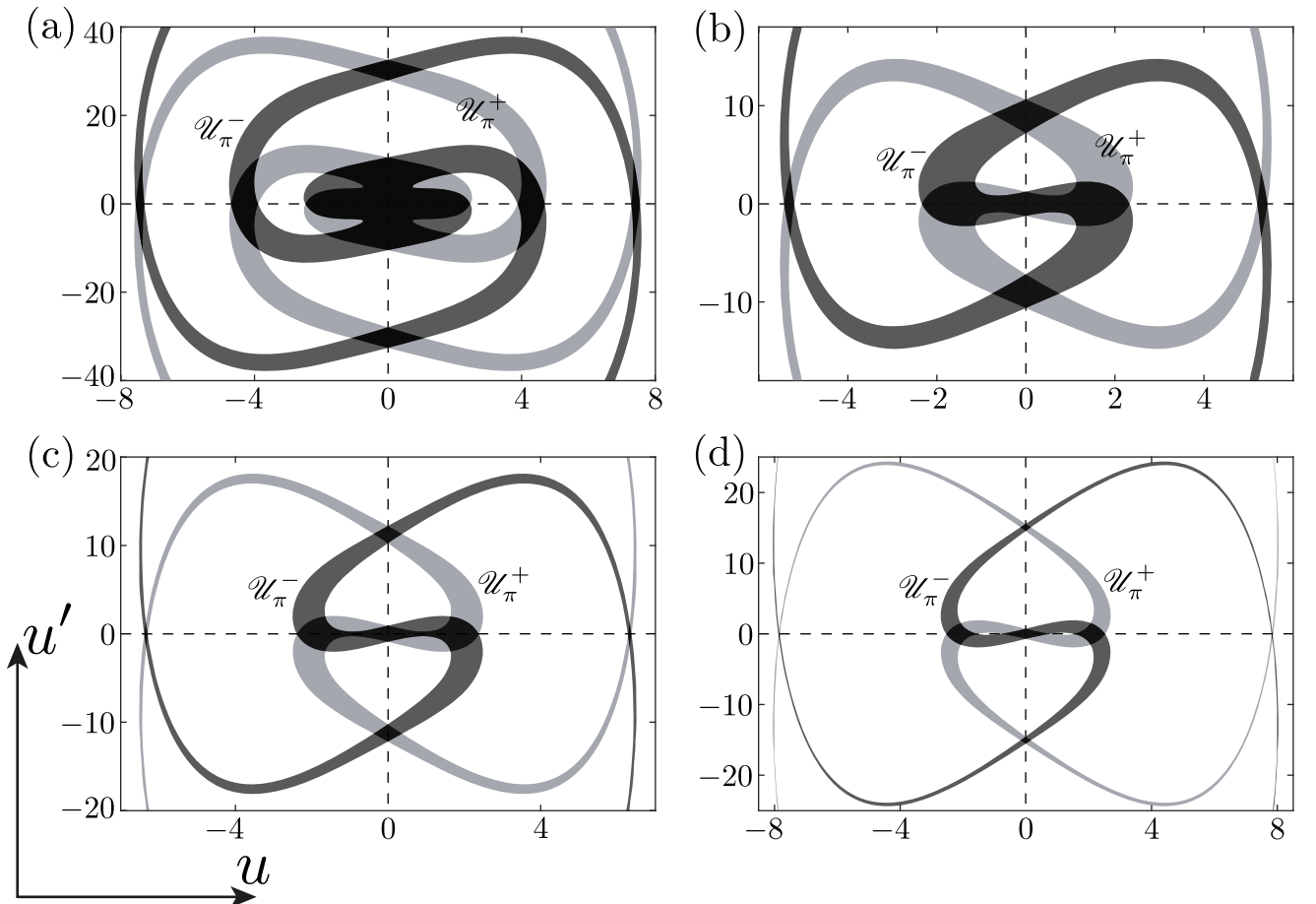


Figure 3.1. Sets \mathcal{U}_π^+ (light gray), \mathcal{U}_π^- (dark gray), and their intersection $\mathcal{U}_\pi = \mathcal{U}_\pi^+ \cap \mathcal{U}_\pi^-$ (black) for equation (3.6) with different parameters (ω, α) . Panel (a): $(\omega, \alpha) = (1, 0.6)$; panel (b): $(\omega, \alpha) = (1, 0.3)$; panel (c): $(\omega, \alpha) = (1, 0.1)$; panel (d): $(\omega, \alpha) = (1, -0.1)$. On panels (a), (b), and (c) intersection \mathcal{U}_π doesn't form an island set due to the central connected component. On panel (d) seven connected components of \mathcal{U}_π form an island set.

Presence of the island set structure is a first required step of our coding technique. In Chapter 2 we established two hypotheses which must be valid, so the conditions of Theorem 1 take place. Let's focus on the case $(\omega, \alpha) = (1.5, 0)$. We restrict the scanning area in plane (u, u') of initial conditions by seven components of \mathcal{U}_π . The set \mathcal{U}_π is depicted in Figure 3.2. From that picture we conclude that Hypothesis I holds since each connected component of \mathcal{U}_π represent a curvilinear quadrangle with monotonic boundaries, and each boundary satisfies the conditions from Definition 4. The connected components can be enumerated with symbols $\{D_k\}$, $k = \pm 1, \pm 2, \dots$ for the components along the u axis, and $k = \pm 1i, \pm 2i, \dots$ for the components along the u' axis. The central component is denoted by D_0 . Applying this notation for the seven-component island set from Figure 3.2 we have $\mathcal{U}_\pi = \bigcup_{k \in S_7} D_k$, $S_7 = \{-2, -1i, -1, 0, +1, +1i, +2\}$.

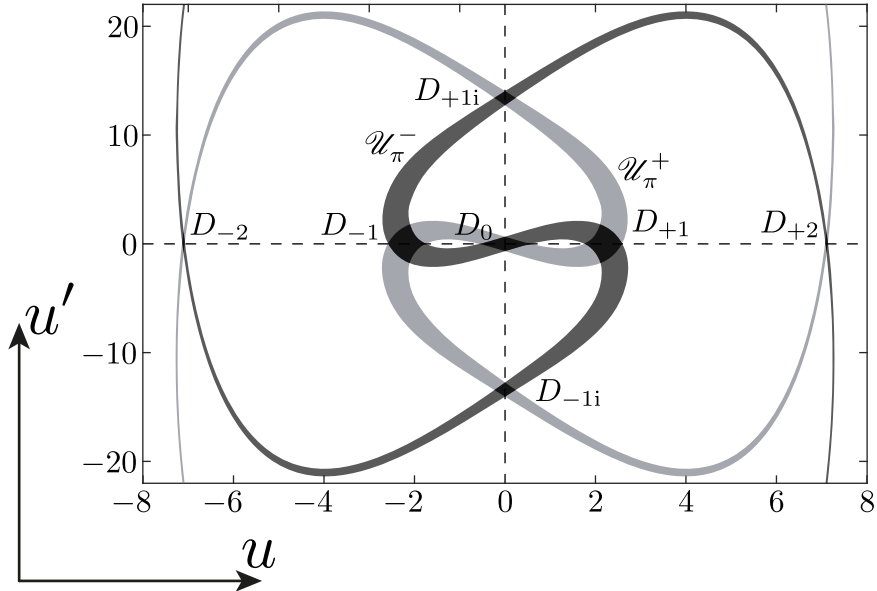


Figure 3.2. Seven-component island set $\mathcal{U}_\pi = \bigcup_{k \in S_7} D_k$ (black) formed by the intersection of \mathcal{U}_π^\pm for equation (3.6) with parameters $(\omega, \alpha) = (1.5, 0)$.

To check Hypothesis II we use the numerical procedure described in Chapter 2 which relies on Strips Mapping Theorems from Appendix C. Since set \mathcal{U}_π is symmetric with respect to the u and u' axis we can check Hypothesis II only for four islands: D_0 , D_{+1} , D_{+2} , and D_{+1i} . For each island D_k we introduce a grid of values for numerical computations like we do it during the scanning procedure. Using that

grid we compute sets $H_{i,k} = \mathcal{P}(D_i) \cap D_k$ and sets $V_{k,i} = \mathcal{P}^{-1}(D_i) \cap D_k$, where $i \in S_7$. In each point $\mathbf{p} \in V_{k,i}$ we construct a matrix of the 2-dimensional linear operator $D\mathcal{P}_{\mathbf{p}} = (a_{mn})$. Then we analyse signs of (a_{mn}) . For each set $V_{k,i}$ sings of (a_{mn}) must have exactly one configuration specified in Theorem 2. For each island D_k we also compute a numerical estimation of the lower boundary of $|a_{11}|$ values, denote it by μ_* . Corresponding histograms of $|a_{11}|$ values in logarithmic scale are presented in Figure 3.3 along with their lower boundary μ_* for each island. Value μ_* is the numerical estimation of the value μ from Theorem 2. If the signs of values (a_{mn}) computed for $V_{k,i}$ sets satisfy the conditions of Theorem 2 and the overall estimation $\mu_* > 1$ takes place, we conclude that Hypothesis II holds true for h-strips.

Similarly, for each set $H_{i,k}$ we construct a matrix of the linear operator $D\mathcal{P}_{\mathbf{p}}^{-1} = (b_{mn})$ in each point $\mathbf{p} \in H_{i,k}$. We perform an estimation of the lower boundary of the values $|b_{22}|$, denote the estimated value by ν_* . If $\nu_* > 1$ and the signs of values (b_{mn}) computed for $H_{i,k}$ sets satisfy the conditions of Theorem 3, we conclude that Hypothesis II holds true for v-strips as well.

Complete results of our numerical analysis are presented in Figure 3.3. Let's provide several examples on how this picture should be treated. Consider an island D_{+1} . Operator $D\mathcal{P}_{\mathbf{p}} = (a_{mn})$ is computed in each point of the set $V_{+1,0}$ and has signs configuration $(\begin{smallmatrix} - & + \\ + & - \end{smallmatrix})$ on the whole $V_{+1,0}$, i.e. $a_{11} < 0, a_{12} > 0, a_{21} < 0, a_{22} > 0$. Boundaries α_{+1}^{\pm} of the island D_{+1} are the parts of boundaries of \mathcal{U}_π^- and have the form of decreasing curves, see Figure 3.3 (b). Boundaries α_0^{\pm} of the island D_0 are increasing curves. It means that condition (2d) of Theorem 2 takes place for a pair of islands D_{+1} and D_0 . For the sets $V_{k,i}$ all the values $|a_{11}| \geq \mu_* > 1$. Thus, according to Theorem 2 we can conclude that for any h-strip $H \in D_{+1}$ its \mathcal{P} -image $\tilde{H}_0 = \mathcal{P}(H) \cap D_0$ is also as h-strip and $d_h(\tilde{H}_0) \leq (1/\mu_*)d_h(H)$.

For another example let's consider a pair of islands D_{+1i} and D_{+2} . Operator $D\mathcal{P}_{\mathbf{p}}^{-1} = (b_{mn})$ has signs configuration of the form $(\begin{smallmatrix} - & - \\ + & + \end{smallmatrix})$ for all $\mathbf{p} \in H_{+1i,+2}$. Boundaries β_{+1i}^{\pm} of the island D_{+1i} are decreasing curves, and boundaries β_{+2}^{\pm} of the island D_{+2} are increasing. Estimations $\nu_* > 1$ takes place for all the sets $H_{i,k}$. Thus, con-

dition (1d) of Theorem 3 is satisfied which implies that and for any v-strip $V \in D_{+2}$ its \mathcal{P} -pre-image $\tilde{V}_{+1i} = \mathcal{P}^{-1}(V) \cap D_{+1i}$ is also a v-strip and $d_v(\tilde{V}_{+1i}) \leq (1/\nu_*) d_v(V)$. Other sets $H_{i,k}$, $V_{k,i}$ are considered in a similar way. According to the numerical computations Theorems 2 and 3 are valid for all islands D_k , $k \in S_7$.

The procedure described above provides a numerical evidence for Hypotheses I and II. That allows us to apply Coding Theorem and conclude that for Eq. (3.6) there exists a homeomorphism $\mathcal{C} : \mathcal{O}_7 \rightarrow \mathcal{S}_7$ between a subset of orbits of bounded solutions, denoted by \mathcal{O}_7 , and a set \mathcal{S}_7 of bi-infinite sequences of symbols from alphabet $S_7 = \{-2, -1i, -1, 0, +1, +1i, +2\}$. Orbits of such solutions may visit only islands D_k , where $k \in S_7$. Moreover there is no any other bounded solution which orbit visits only these seven islands. The numerical results from above can be extended to a larger island set, although it requires significant computing capacities.

Existence of the homeomorphism allows to make a conclusion on the structure of bounded solutions of Eq. 3.6 For example Eq. 3.6 admits periodic solution of period $n\pi$ for any number $n \in \mathbb{N}$. Several periodic solutions are presented in Figure 3.4, π -periodic solution in panel (a), and 2π -periodic solutions in panels (b) and (c). There also exists a plethora of soliton solutions. The orbit corresponding to the soliton solution starts and ends in the central connected components; therefore, it has the code of the form $\{\dots, 0, 0, k_1, k_2, \dots, k_N, 0, 0, \dots\}$, where symbols k_1 and k_N are different from “0”. Some of the soliton solutions of (3.6) for $(\omega, \alpha) = (1.5, 0)$ are shown in Figure 3.4, panels (d) — (i). The soliton solution in panel (d) is the fundamental soliton (FS) that has been already studied in [17]. It has code $\{\dots, 0, +1, 0, \dots\}$, or $\{\dots, 0, -1, 0, \dots\}$ which is its symmetric counterpart.

Other types of localized solutions have been also found. For example, solution, shown in panel (e), represents a so-called *dipole soliton* (DS) [18], which is essentially confined to a single period of pseudopotential $P(x)$. This solution corresponds to code $\{\dots, 0, -1i, 0, \dots\}$, and its symmetric counterpart is $\{\dots, 0, +1i, 0, \dots\}$. DS is similar to *sub-fundamental solitons* (SFSs) reported in [19, 20, 21, 22] in models with the linear lattice potential $U(x)$, as both soliton species feature the

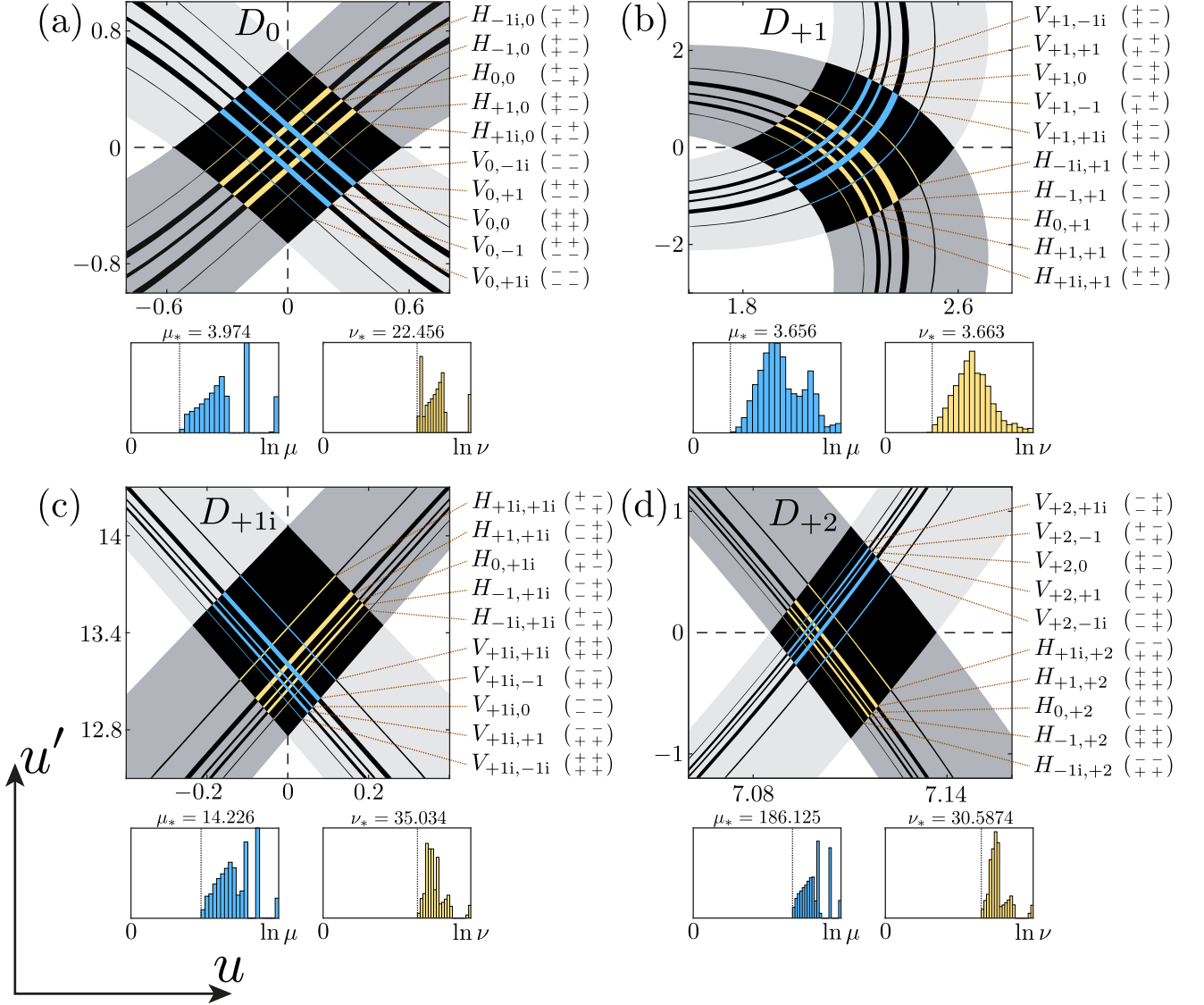


Figure 3.3. Illustration to Hypothesis II validation for equation (3.6) with parameters $(\omega, \alpha) = (1.5, 0)$. Islands D_k are black curvilinear quadrangles with monotonic boundaries. Boundaries of the set \mathcal{U}_π^+ (light gray) contains β_k^\pm boundaries for each island D_k ; boundaries of \mathcal{U}_π^- (dark gray) contains α_k^\pm boundaries correspondingly. Estimations of μ_* and ν_* values are shown with histograms below each island. Configuration of value signs in operators $D\mathcal{P}_{\mathbf{p}} = (a_{mn})$, $\mathbf{p} \in V_{k,i}$ (blue), and $D\mathcal{P}_{\mathbf{p}}^{-1} = (b_{mn})$, $\mathbf{p} \in H_{i,k}$ (yellow) are shown from the right side of each island D_k . All of them satisfy the conditions of Theorem 2 (On h-strip mapping) and Theorem 3 (On v-strips mapping) from Appendix C. Sets $H_{+2,k}$ and $V_{k,+2}$ are not depicted since they are too thin and barely visible at this scale, but all the computations have been also provided for them and the overall result satisfies the above mentioned theorems as well.

antisymmetric profile squeezed into a single cell of the underlying lattice potential (ordinary potential $U(x)$, in the case of SFS, and the pseudopotential $P(x)$, as concerns the DS). The area of the localization of the soliton corresponding to code

$\{\dots, 0, k_1, \dots, k_N, 0, \dots\}$, where the symbols k_1 and k_N are different from “0”, is $N\pi$, i.e. it extends over N periods of the underlying pseudopotential $P(x)$. In particular, the solitons with codes $\{\dots, 0, k, 0, \dots\}$, $k \neq 0$ (named *elementary solitons*), are localized, essentially, in one period of the pseudopotential.

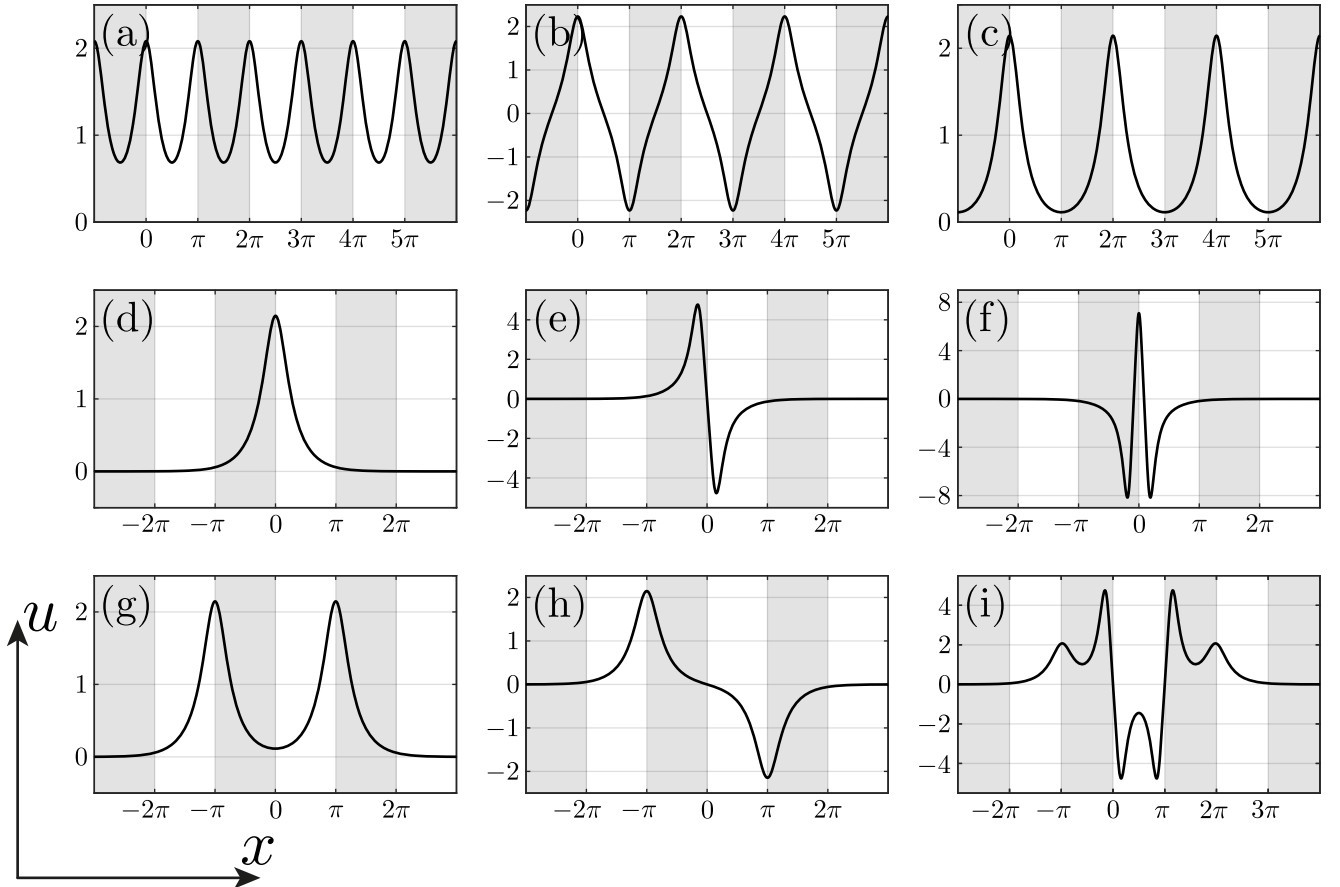


Figure 3.4. Different solutions for equation (3.6) with parameters $(\omega, \alpha) = (1.5, 0)$. Each solution has a corresponding symbolic code, this code identify the solution uniquely. Gray strips divide the x axis according to the period π . First three panels represent periodic solutions, their codes have periodic structure: (a) π -periodic solution $\{\dots, +1, +1, +1, \dots\}$; (b) 2π -periodic solution $\{\dots, +1, -1, +1, -1, \dots\}$; (c) 2π -periodic solution $\{\dots, +1, 0, +1, 0, \dots\}$. Other six panels represent localized solutions, their codes have “0” symbol to the left and right of the central block: (d) fundamental soliton with code $\{\dots, 0, +1, 0, \dots\}$; (e) dipole soliton with code $\{\dots, 0, -1i, 0, \dots\}$ (f) elementary soliton with code $\{\dots, 0, +2, 0, \dots\}$ (g) $\{\dots, 0, +1, 0, +1, 0, \dots\}$ (h) $\{\dots, 0, +1, 0, -1, 0, \dots\}$ (i) $\{\dots, 0, +1, -1i, +1, \dots\}$.

3.3. Analysis of Stability

Stability is a critically important issue for stationary localized solutions. By stability of localized stationary solution we mean its resistance to small perturbations. From the perspective of real physical experiments only stable solutions can be obtained in a real experimental setup. Here we address the stability of stationary localized solutions produced by Eq. (3.5). Let $u(x)$ be a solution if Eq. (3.6). Following the well-established approach, see e.g. [23], let's consider small perturbations around a solution $u(x)$ of the form

$$\Psi(t, x) = \left(u(x) + \tilde{U}(t, x) \right) e^{i\omega t}; \quad |\tilde{U}(t, x)| \ll 1, \quad (3.7)$$

where $\tilde{U}(t, x)$ is a complex-valued function. Then the perturbation $\tilde{U}(t, x)$ satisfies the linear equation

$$i\tilde{U}_t + \tilde{U}_{xx} - \omega\tilde{U} + (\alpha + \cos 2x)u^2(2\tilde{U} + \tilde{U}^\dagger) = 0. \quad (3.8)$$

Here dagger “ \dagger ” means complex conjugate. Seeking solutions to (3.8) as

$$\tilde{U}(t, x) = (v(x) + w(x))e^{\lambda t} + (v^\dagger(x) - w^\dagger(x))e^{\lambda^\dagger t}; \quad \lambda \in \mathbb{C}, \quad (3.9)$$

we arrive at the eigenvalue problem

$$i \begin{pmatrix} 0 & \partial_{xx} + G_1(x) \\ \partial_{xx} + G_2(x) & 0 \end{pmatrix} \begin{pmatrix} v \\ w \end{pmatrix} = \lambda \begin{pmatrix} v \\ w \end{pmatrix}, \quad (3.10)$$

where

$$G_1(x) = -\omega + (\alpha + \cos 2x)u^2;$$

$$G_2(x) = -\omega + 3(\alpha + \cos 2x)u^2.$$

Equation (3.10) is the linear-stability eigenvalue problem for the soliton. Its λ -spectrum is called the linear-stability spectrum for this soliton. The soliton is linearly stable if the spectrum produced by Eq. (3.10) contains at least one eigenvalue λ with a non-zero real part, $\Re(\lambda) > 0$. Otherwise, the soliton is linearly unstable.

Equation (3.10) generates spectrum consisting of continuous and discrete parts. One can show, see e.g. [23], that the continuous spectrum is represented by two rays, $[i\omega; +i\infty)$ and $(-i\infty; -i\omega]$, if $\omega > 0$, and by the whole imaginary axis, if $\omega < 0$. The discrete spectrum includes zero eigenvalue $\lambda = 0$. It is easy to see that other eigenvalues of discrete spectrum of Eq. (3.10) have the following symmetry properties: if λ is an eigenvalue, then so are λ^\dagger , $-\lambda$, and $-\lambda^\dagger$. This means that these eigenvalues always appear in pairs or quadruples.

3.3.1. Fourier Collocation Method

To find discrete eigenvalues numerically we use so-called Fourier Collocation Method (FCM) described in [23]. This method is very efficient to find *exponential instabilities* that appear due to real eigenvalues. We also say that solution *oscillatory unstable* if the spectrum has quartets of complex with non-zero real parts.

To apply FCM, we first truncate the infinite x -axis into a finite interval into a finite interval $[-L/2; L/2]$, where L is the length of the interval. Length of the interval is considered to be large enough to cover soliton solution localization well. On this interval we expand the eigenfunctions $[v(x); w(x)]^T$ and functions G_1 , G_2 into Fourier series:

$$v(x) = \sum_n a_n e^{ink_0 x}; \quad w(x) = \sum_n b_n e^{ink_0 x}, \quad (3.11)$$

$$G_1 = \sum_n c_n^{(1)} e^{ink_0 x}; \quad G_2 = \sum_n c_n^{(2)} e^{ink_0 x}, \quad (3.12)$$

where $k_0 = 2\pi/L$. After substitution of (3.11) and (3.12) into (3.10), we have the following eigenvalue system fro the coefficients a_j , b_j :

$$-(k_0 j)^2 b_j + \sum_n c_n^{(1)} b_{j-n} = -i\lambda a_j; \quad (3.13)$$

$$-(k_0 j)^2 a_j + \sum_n c_n^{(2)} a_{j-n} = -i\lambda b_j, \quad (3.14)$$

where $-\infty < j < +\infty$. Truncating the number of Fourier modes to $-N \leq j \leq N$, this infinite-dimensional eigenvalue problem can be reduced to the finite-dimensional

one:

$$i \begin{pmatrix} 0 & D + C_1 \\ D + C_2 & 0 \end{pmatrix} \begin{pmatrix} A \\ B \end{pmatrix} = \lambda \begin{pmatrix} A \\ B \end{pmatrix}, \quad (3.15)$$

where

$$D = (ik_0)^2 \text{diag}(-N, -N+1, \dots, N-1, N)^2;$$

$$A = (a_{-N}, a_{-N+1}, \dots, a_N)^T; \quad B = (b_{-N}, b_{-N+1}, \dots, b_N)^T,$$

and matrices C_1, C_2 are of the form of Toeplitz matrices

$$C_{1,2} = \begin{pmatrix} c_0^{(1,2)} & c_{-1}^{(1,2)} & \cdots & c_{-N}^{(1,2)} & 0 & \cdots & 0 \\ c_1^{(1,2)} & c_0^{(1,2)} & c_{-1}^{(1,2)} & \ddots & \ddots & \ddots & \vdots \\ \vdots & c_1^{(1,2)} & c_0^{(1,2)} & c_{-1}^{(1,2)} & \ddots & \ddots & 0 \\ c_N^{(1,2)} & \ddots & \ddots & \ddots & \ddots & \ddots & c_{-N}^{(1,2)} \\ 0 & c_N^{(1,2)} & \ddots & \ddots & \ddots & \ddots & \vdots \\ \vdots & \ddots & \ddots & \ddots & \ddots & \ddots & \vdots \\ 0 & \cdots & 0 & c_N^{(1,2)} & \cdots & c_1^{(1,2)} & c_0^{(1,2)} \end{pmatrix}. \quad (3.16)$$

The matrix eigenvalue problem (3.15) can be solved by any matrix eigenvalue problem solver. Solution of the eigenvalue problem gives $2N + 1$ eigenvalues. In our computations we used $N = 256$ and $N = 512$ and got nearly identical spectrums. From the practical point of view for the linear-stability analysis the number of Fourier modes can be relatively small, since eigenvalues for the higher modes have zero real part.

3.3.2. Evolutionary Simulation

To control linear-stability analysis and get additional confidence in stability of localized solutions we also performed a numerical simulation of their evolution. For that purpose Trofimov-Peskov finite-difference scheme [24] for numerical solution of the Gross-Pitaevskii (3.1) equation was used. The scheme preserves several

invariants of the problem: the norm of the solution

$$N = \int_{-\infty}^{+\infty} |u(x)|^2 dx, \quad (3.17)$$

and its energy

$$E = \int_{-\infty}^{+\infty} \left(|u'(x)|^2 + U(x)|u(x)| - \frac{1}{2}P(x)|u(x)|^4 \right) dx. \quad (3.18)$$

The scheme is implicit, its realization implying iterations for the calculation of values in each temporal layer, but it allows running computation with larger temporal step. In order to reveal instability (if it is), the soliton profile was perturbed at the initial moment with a small perturbation. A finite spatial domain $[-5\pi; 5\pi]$ was used, with reflection of radiation from boundaries eliminated by means of absorbing boundary conditions. During our analysis we got consistent results between the linear stability and evolutionary simulation.

3.3.3. Results of Linear Stability Analysis

With the help of FCM, a great number of localized stationary solutions of equation (3.5), represented by different codes, were analyzed. Due to the infinite number of essentially different solitons, it's not possible to perform a comprehensive stability analysis of all localized solutions. However, we observed that a majority of the solitons are linearly unstable, thus being physically irrelevant solutions. *Stable solitons* can be categorized as follows:

- (a) among the elementary solitons, it was found that FS and DS are *linearly stable*, under some restrictions on parameters ω and α , while other elementary solitons were found to be unstable;
- (b) there are stable localized solutions of the form of FS complexes — for instance, with codes $\{\dots, 0, +1, -1, +1, 0, \dots\}$ and $\{\dots, +1, 0, -1, 0, \dots\}$.

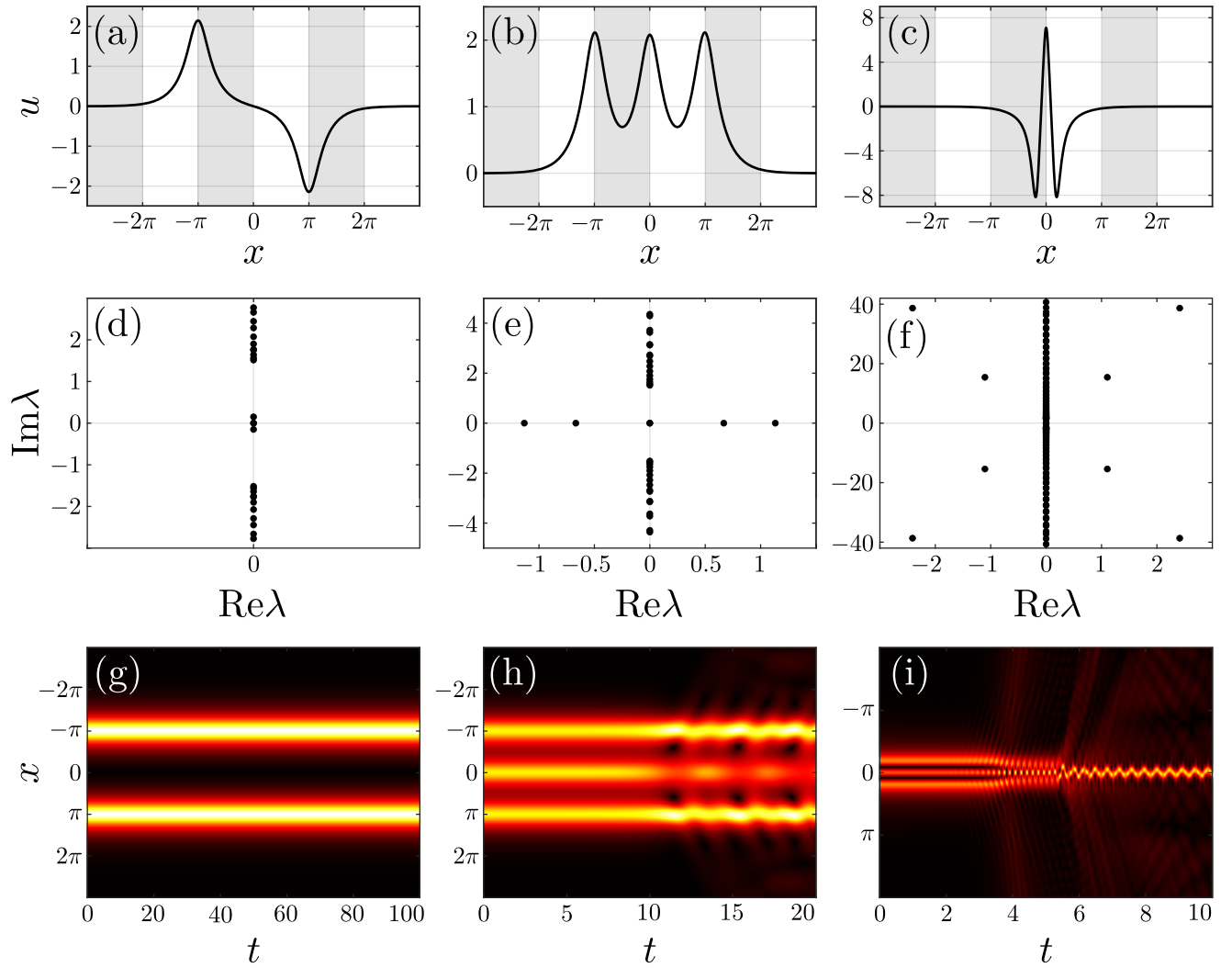


Figure 3.5. Examples of stability analysis for localized solutions of equation (3.5) with parameters $(\omega, \alpha) = (1.5, 0)$. First three panels represent profiles of solutions of different codes: (a) $\{\dots, 0, +1, 0, -1, 0, \dots\}$; (b) $\{\dots, 0, +1, +1, +1, 0, \dots\}$; (c) $\{\dots, 0, +2, 0, \dots\}$. Panels (d), (e), and (f) are the corresponding λ -spectrums for the solutions above. According to them, solution in panel (a) is linearly stable. Solution in panel (b) is exponentially unstable, while solution in panel (c) is oscillatory unstable. Linear-stability analysis match the results of evolutionary simulation presented in panel (g), (h), and (i).

Several localized solution, their linear-stability spectrums, and corresponding results of evolutionary simulation are in Figure 3.5. Panel (a) corresponds to a stable localized solution of code $\{\dots, 0, +1, 0, -1, 0, \dots\}$. Such solution can be considered as a combination of two FSs of codes $\{\dots, 0, +1, 0, \dots\}$ and $\{\dots, 0, -1, 0, \dots\}$. Another similar combination of code $\{\dots, 0, +1, +1, +1, 0, \dots\}$ in panel (b) is unstable. Elementary soliton of code $\{\dots, 0, +2, 0, \dots\}$ from panel (c) is unstable as

well as any other elementary solitons except of FS and DS. Other examples can be found in our work [18].

Combination of coding technique and linear-stability analysis together give a powerful tool of visualization of stationary localized solutions stability for equation of type (3.1) with periodic potential and pseudopotential. If it's possible to find such parameters that the Theorem 1 is applicable, then for these parameters we can apply coding and describe at least a huge subset of bounded solutions. After that one can vary one of the parameters using a numerical grid and perform a numerical continuation for the described solutions to the non-coding area of parameters. During the numerical continuation of solutions we can compute linear-stability spectrums in each point of the parameters grid. Then we can parametrized the obtained solutions, for example using their norm (3.17), plot the branches of different solution families and color the stability regions.

Illustration of the described idea for Eq. (3.5) is presented in Figure 3.6. In that figure several branches of solutions are depicted in (N, ω) axes, while parameter $\alpha = 0$. Regions of linear stability are marked with bold black lines. One can see that FS solution of code $\{\dots, 0, \pm 1, 0, \dots\}$, branch (I), and solution of code $\{\dots, 0, \pm 1, 0 \mp 1, 0, \dots\}$, branch (II), are mostly stable and loose their stability near the point $\omega = 0$. Dipole soliton, branch (IV), exists for $\omega > \omega^*$ and has an ω -region of stability. At $\omega^* \approx 0.265$, the DS family, coded by $\{\dots, 0, \pm 1i, 0, \dots\}$, undergoes a saddle-node bifurcation and annihilate with the family coded by $\{\dots, 0, \mp 1, \pm 1i, \pm 1, 0, \dots\}$.

Stable Dipole Soliton

As an outcome of our analysis for physical applications, the most significant finding is the existence of stable DS family, which was not previously considered in the setting of GPE with periodic pseudopotential. Existence of such family is also predicted by variational approximation method, see [18]. The DS family may be parametrized by ω . The norm of the DS grows with the growth of ω . Although the DS is very similar, in its shape, to the sub-fundamental solitons in systems with

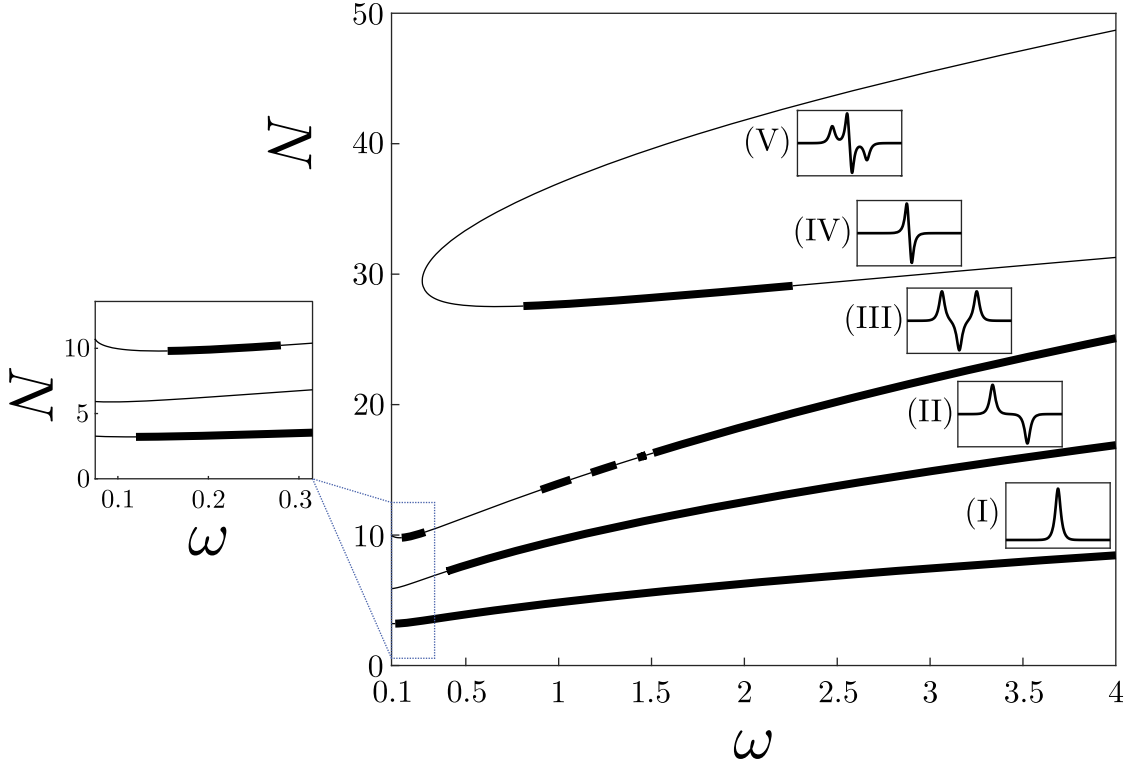


Figure 3.6. Branches of solutions for Eq. (3.5) and their linear stability. Branch (I) represent fundamental soliton family of code $\{\dots, 0, \pm 1, 0, \dots\}$. Branches (II) and (III) are FS complexes of codes $\{\dots, \pm 1, 0, \mp 1, 0, \dots\}$ and $\{\dots, \pm 1, \mp 1, \pm 1, 0, \dots\}$ correspondingly. Dipole soliton family of code $\{\dots, 0, \pm 1i, 0, \dots\}$ is presented by the branch (IV). It coalesces at $\omega = \omega^*$ with family $\{\dots, 0, \mp 1, \pm 1i, \pm 1, 0, \dots\}$ of branch (V). Linear stability regions are colored with bold black lines.

periodic potential, the DS in the present model is not sub-fundamental, as its norm is *higher* than that of the FS existing for the same ω , see Figure 3.6. Evolutionary simulation showed that if for some ω the DS is unstable, then it transforms into the FS after some time. An example of that is provided in Figure 3.7.

3.4. Summary

In this chapter we studied stationary solutions of Gross–Pitaevskii equation (3.1) with presence of periodic pseudopotential $P(x)$ of the cosine form (3.4), while potential $U(x)$ is absent. We focused on localized solutions as they are of particular interest for physical experiments. Periodicity of pseudopotential $P(x)$ allowed us to apply coding technique from Chapter 2. We provided a numerical evidence for Hy-

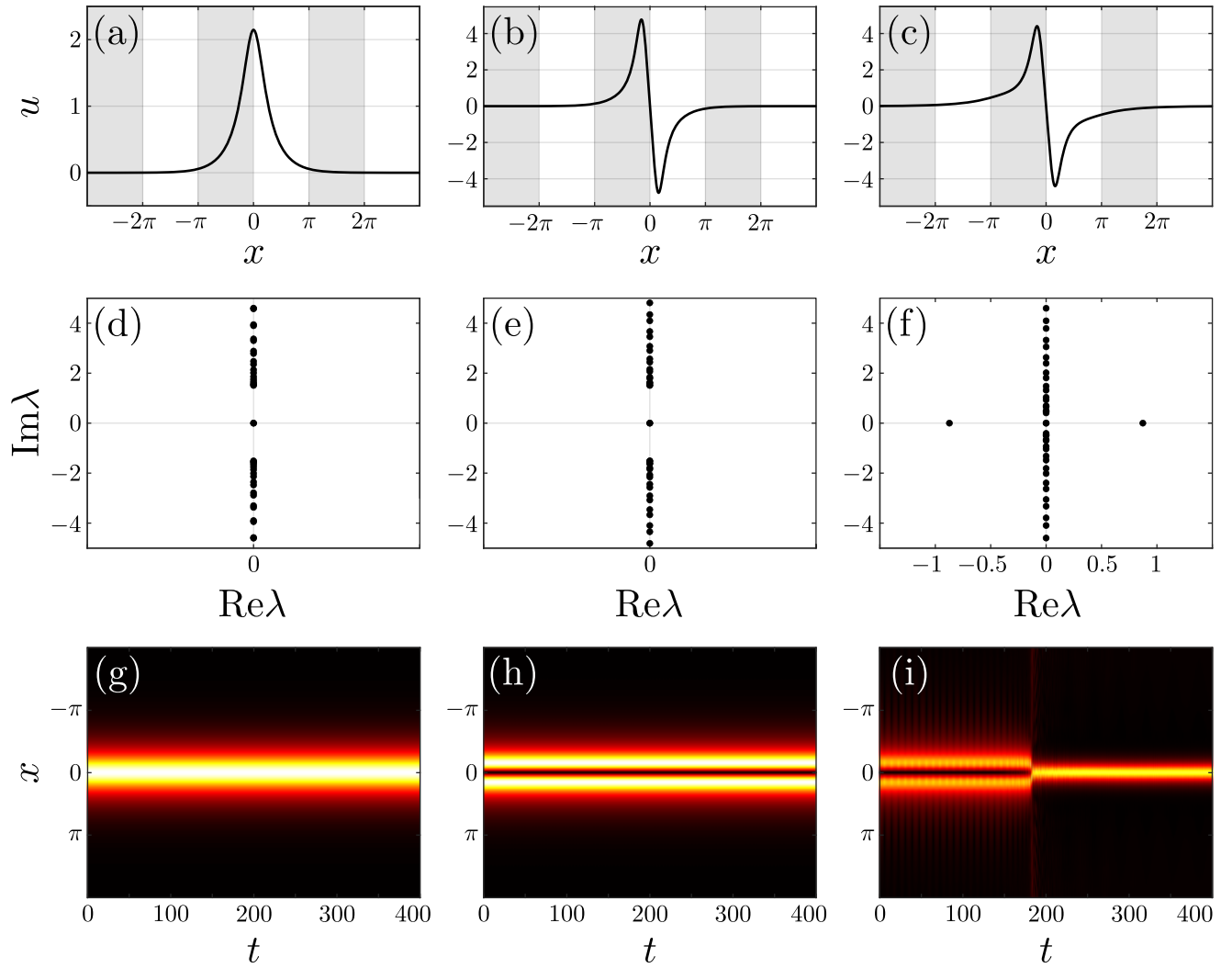


Figure 3.7. Stability of dipole soliton. Panel (a) represent a stable fundamental soliton (FS) for parameters $(\omega, \alpha) = (1.5, 0)$. Panel (b) corresponds to stable dipole soliton (DS) for $(\omega, \alpha) = (1.5, 0)$. Unstable DS is presented in panel (c) for parameters $(\omega, \alpha) = (0.4, 0)$. It's exponentially unstable and during our simulation at $t \approx 200$ transforms into a stable fundamental soliton.

potheses I and II, which allow to apply Theorem 1, and concluded that there exist a homeomorphism between a subset of bounded solutions and bi-infinite symbolic sequences from some alphabet. Existence of the homeomorphism reveal the complex nature of stationary solutions. Like we saw it in Chapter 2 presence of periodic pseudopotential that alters its sign along the period generates a great variety of different stationary solutions. We apply linear-stability analysis to identify physically relevant localized solutions among them. Outcome of our analysis is the existence of stable dipole soliton (DS) family previously not considered in this setting. Results of our finding were published in [18].

Chapter 4

Localized Solutions of Nonlinear Harmonic Oscillator with Periodic Pseudopotential

4.1. Objectives

In this chapter we study localized solutions of Gross–Pitaevskii equation with a harmonic-oscillator (parabolic) trapping potential and a periodic pseudopotential in front of cubic term. The effective one-dimensional GPE for mean-fields wave function $\Psi(t, x)$ is

$$i\Psi_t + \Psi_{xx} - \frac{1}{2}a^2x^2\Psi + P(x)|\Psi|^2\Psi = 0, \quad (4.1)$$

where a^2 is the strength of the harmonic-oscillator potential, and pseudopotential $P(x)$ is a function of period $L = 2\pi/\Omega$:

$$P(x + 2\pi/\Omega) = P(x). \quad (4.2)$$

Such model can be achieved by means of combination of a magnetic trap and an optical lattice which induces the periodic pseudopotential via the Feshbach resonance [25]. Intervals with positive (negative) values of $P(x)$ correspond to spatial domains with attractive (repulsive) interactions between particles.

The model includes *two scales*: the characteristic harmonic-oscillator length $l_{HO} \sim 1/\sqrt{a}$, and period $L = 2\pi/\Omega$ of the pseudopotential. In particular, the limit case of the wide harmonic-oscillator trap $\Omega \gg 2\pi\sqrt{a}$, is a physically relevant one. Let's introduce additional rescaling

$$t \rightarrow \frac{a}{\sqrt{2}}t, \quad x \rightarrow \frac{\sqrt{a}}{\sqrt[4]{2}}x, \quad \Psi \rightarrow \frac{\sqrt[4]{2}}{\sqrt{a}}\Psi. \quad (4.3)$$

This allows to fix $a \equiv 1$ and convert (4.1) into a normalized form

$$i\Psi_t + \Psi_{xx} - x^2\Psi + P(x)|\Psi|^2\Psi = 0, \quad (4.4)$$

where $P(x)$ is periodic with spatial frequency $\tilde{\Omega} = \Omega/\sqrt{a}$. In what follows below, symbol $\tilde{\Omega}$ is replaced by Ω . To estimate physically relevant values of Ω we use the results of experimental realization of the periodically-modulated Feshbach resonance in [15]. There the corresponding scaled spatial frequency being $\Omega \sim 100$. It can be made smaller, taking larger a .

Equation (4.4) is our basic model. The objective of our analysis is to study its localized stationary solutions of the form

$$\Psi(t, x) = u(x)e^{-i\omega t}, \quad (4.5)$$

where real-valued function $u(x)$ satisfies equation

$$u_{xx} + (\omega - x^2)u + P(x)u^3 = 0 \quad (4.6)$$

with localization boundary conditions

$$\lim_{x \rightarrow \pm\infty} u(x) = 0. \quad (4.7)$$

During our numerical analysis we focus on the practically important case when the pseudopotential function $P(x)$ in (4.4) is taken as a sum of constant and harmonic parts of a prototypical cosine form:

$$P(x) = P_0 + P_1 \cos(\Omega x). \quad (4.8)$$

As we say it in Chapter 3 stability of solutions is a critically important property. Linear stability of localized solutions is addressed by considering of small perturbations of a solution $u(x)$ of the form:

$$\Psi(t, x) = \left(u(x) + (v(x) + w(x))e^{\lambda t} + (v^\dagger(x) - w^\dagger(x))e^{\lambda^\dagger t} \right) e^{-i\omega t}, \quad (4.9)$$

where $|v(x)| \ll 1$, $|w(x)| \ll 1$. Substituting (4.9) into (4.4) and performing linearization with respect to $v(x)$ and $w(x)$, we arrive at eigenvalue problem

$$i \begin{pmatrix} 0 & \mathcal{L}_- \\ \mathcal{L}_+ & 0 \end{pmatrix} \begin{pmatrix} v \\ w \end{pmatrix} = \lambda \begin{pmatrix} v \\ w \end{pmatrix}, \quad (4.10)$$

where

$$\begin{aligned}\mathcal{L}_- &= \partial_{xx} + \omega - x^2 + P(x)u^2; \\ \mathcal{L}_+ &= \partial_{xx} + \omega - x^2 + 3P(x)u^2.\end{aligned}$$

This problem is similar to the previously considered problem (3.10). Fourier Collocation Method from Chapter 3 is also applicable for effective numerical evaluation of spectrum (4.10). Eigenvalues with non-zero real part rise to the instability, while pure imaginary spectrum indicates that solutions is linearly stable. Again, we note that the eigenvalues appears in pairs and quadruples, i.e. if λ is an eigenvalue, then $-\lambda$, λ^\dagger , $-\lambda^\dagger$ are eigenvalues too.

For the analytical analysis during this chapter it's convenient to rewrite eigenvalue problem (4.10) in the equivalent form:

$$\mathcal{L}_+\mathcal{L}_-w = \Lambda w, \quad \Lambda = -\lambda^2. \quad (4.11)$$

In terms of (4.11), a solution $u(x)$ passes the linear stability test if the spectrum of eigenvalues Λ is all-real positive.

4.1.1. Solutions with linear counterpart

An important class of localized solutions of equation (4.6) is *nonlinear solutions with linear counterpart*. Such terminology has been adopted in [26, 27]. Existence of such solution came from the consideration of the low-amplitude limit. For a small value of norm N , see (3.17), the nonlinear term in (4.6) may be neglected, which leads to the ordinary harmonic-oscillator equation

$$u_{xx} + (\omega - x^2)u = 0. \quad (4.12)$$

Equation (4.12) produces the commonly known set of eigenvalues and eigenfunctions:

$$\tilde{\omega}_n = 2n + 1; \quad \tilde{u}_n(x) = \frac{1}{\sqrt{2^n n! \sqrt{\pi}}} H_n(x) e^{-\frac{1}{2}x^2}; \quad n = 0, 1, \dots, \quad (4.13)$$

where $H_n(x)$ functions are Hermite polynomials. In particular,

$$H_0(x) = 1, \quad H_1(x) = 2x, \quad H_2(x) = 4x^2 - 2.$$

When the nonlinearity is switched on, each linear eigenstate $(\tilde{\omega}_n, \tilde{u}_n(x))$ bifurcates into a one-parameter set $\Gamma_n = (\omega_n, u_n(x))$ of small-amplitude localized solutions of (4.6). These solutions are produced by equation (4.6) and become essentially nonlinear with the increase of N and distance between ω_n and $\tilde{\omega}_n$. Localized solutions from family Γ_n feature the same parity as the corresponding linear eigenfunction $\tilde{u}_n(x)$, solution with even n are even functions of x , and those with the odd n are odd. Localized solution with $n = 0$ originates from the ground state of the harmonic-oscillator.

During our analysis it's interesting to compare the results with the well-studied case of Gross–Pitaevskii equation (4.4) with constant $P(x)$ (negative or positive). In this case $P_1 \equiv 0$ in (4.8), and after additional rescaling $\Psi \rightarrow \Psi / \sqrt{|P_0|}$ equation (4.6) takes form

$$u_{xx} + (\omega - x^2)u + \sigma_0 u^3 = 0, \quad (4.14)$$

where $\sigma_0 = P_0/|P_0| = \text{sign}(P_0)$. Let's call equation (4.14) the *nonlinear harmonic-oscillator equation with constant pseudopotential* (we also refer to this equation simply as *nonlinear harmonic-oscillator*). The case $\sigma_0 = 1$ ($\sigma_0 = -1$) corresponds to the attractive (repulsive) interparticle interactions. It's convenient to illustrate branches of localized solutions of equation (4.14) by means of respective $N(\omega)$ curves, which are presented in Figure 4.1, as per [28, 29] for the cases $\sigma_0 = \pm 1$. The branches Γ_n , $n = 0, 1, \dots$, correspond to the solutions with linear counterparts, bifurcating from them at the points $\tilde{\omega}_n = 2n + 1$, $N = 0$. All the branches being represented by monotonous functions $N(\omega)$. Other results obtained for localized solutions of (4.14) can be presented as follows.

- Presumably, there exist no nonlinear solutions of (4.14) without linear counterpart [6].

- Solutions corresponding to families Γ_0, Γ_1 are stable in the small-amplitude limit and for moderate and large amplitudes as well for both cases $\sigma_0 = \pm 1$.
- The small-amplitude solutions belonging to the branch Γ_2 are unstable. For the case $\sigma_0 = 1$, the instability of the branch Γ_2 persists for $\omega^* < \omega < 5$, where $\omega^* \approx 3.83$. According to the numerical study at $\omega < \omega^*$ these solutions was reported to be stable [6]. For the case $\sigma_0 = -1$ the branch Γ_2 is fully unstable.

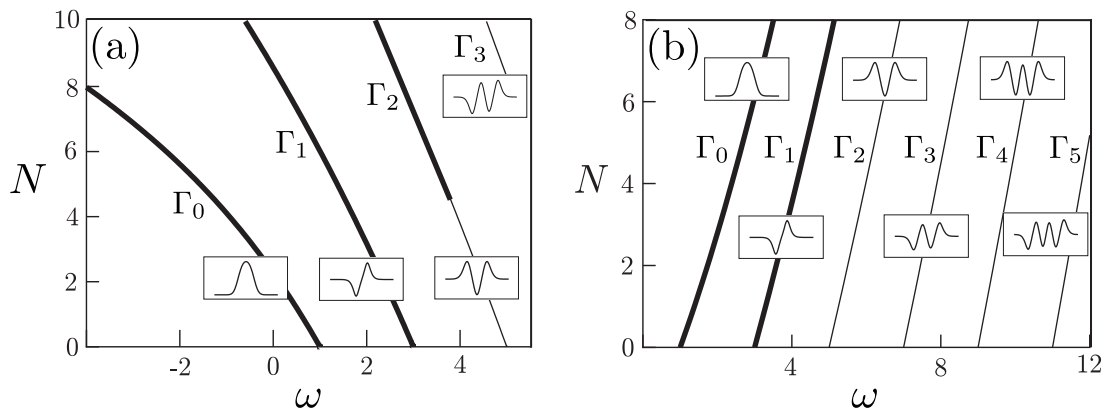


Figure 4.1. $N(\omega)$ curves for equation (4.14), with (a) $\sigma_0 = 1$, (b) $\sigma_0 = -1$. Bold (thin) segments correspond to stable (unstable) solutions. Insets show schematic profiles of solutions $u_n(x)$ from each family Γ_n .

Before we can move on let's briefly resume our goals in this chapter. We study localized solutions of equation (4.4) with periodic pseudopotential (4.8). We apply linear stability analysis to find stable solutions among them. Our baseline model for comparison is well-studied equation (4.14) for nonlinear harmonic-oscillator with constant pseudopotential. We pay special attention to the localized solutions with linear counterpart, and study how the presence of periodic pseudopotential $P(x)$ of the cosine form (4.8) affects their stability.

4.2. Small-Amplitude Localized Solutions with Linear Counterpart

For Eq. (4.6) let's consider a small-amplitude limit of solutions with linear counterpart. As we say above, such solutions $u_n(x)$ originate from the bifurcation of eigenstates $(\tilde{\omega}_n, \tilde{u}_n(x))$ of harmonic-oscillator equation (4.12) and form families $\Gamma_n = (\omega_n, u_n(x))$. If the amplitude of $u_n(x)$ is small the localized solutions from branch Γ_n are approximated by expansions [29],

$$u_n(x) = \varepsilon \tilde{u}_n(x) + o(\varepsilon), \quad \omega_n = \tilde{\omega}_n - \varepsilon^2 \Delta_n + o(\varepsilon^2), \quad (4.15)$$

where $\varepsilon \ll 1$ is a small parameter, and

$$\Delta_n = \int_{-\infty}^{+\infty} P(x) \tilde{u}_n^4(x) dx = \frac{1}{2^{2n}(n!)^2 \pi} \int_{-\infty}^{+\infty} P(x) H_n^4(x) e^{-2x^2} dx. \quad (4.16)$$

Let's address stability of these small-amplitude solutions. We note that with the help of expansion (4.15), operator $\mathcal{L}_+ \mathcal{L}_-$ in (4.11) may be considered as a perturbation of operator \mathcal{L}_n^2 , where

$$\mathcal{L}_n = \partial_{xx} + 2n + 1 - x^2. \quad (4.17)$$

Specifically,

$$\begin{aligned} \mathcal{L}_+ &= \mathcal{L}_n + \varepsilon^2 (3P(x) \tilde{u}_n^2(x) - \Delta_n) + o(\varepsilon^2); \\ \mathcal{L}_- &= \mathcal{L}_n + \varepsilon^2 (P(x) \tilde{u}_n^2(x) - \Delta_n) + o(\varepsilon^2). \end{aligned}$$

So, for the operator $\mathcal{L}_+ \mathcal{L}_-$ we can write

$$\mathcal{L}_+ \mathcal{L}_- = \mathcal{L}_n^2 + \varepsilon^2 M_n + o(\varepsilon^2), \quad (4.18)$$

where

$$M_n = (2P(x) \tilde{u}_n^2(x) - \Delta_n) \mathcal{L}_n + \mathcal{L}_n (P(x) \tilde{u}_n^2(x) - \Delta_n). \quad (4.19)$$

Operator \mathcal{L}_n is self-adjoint in L^2 space, and its spectrum consists of eigenvalues $\varkappa_k = 2(n - k)$ with corresponding eigenfunctions $\tilde{u}_k(x)$, $k = 0, 1, \dots$ in the form (4.13).

The spectrum is equidistant, all the eigenvalues being simple. There are infinitely many negative eigenvalues, n positive eigenvalues, and one zero eigenvalue. The eigenvalues $\tilde{\Lambda}_k$ of operator \mathcal{L}_n^2 are squared eigenvalues of \mathcal{L}_n , i.e. $\tilde{\Lambda}_k = \varkappa_k^2 = 4(k - n)^2$, corresponding to the same eigenfunctions $\tilde{u}_k(x)$. This means that the spectrum of \mathcal{L}_n^2 includes n *double positive eigenvalues* $\tilde{\Lambda}_k = 4(n - k)^2$, $k = 0, 1, \dots, (n - 1)$, one *simple zero eigenvalue* and *infinitely many simple positive eigenvalues*. Each of the double eigenvalues has an invariant subspace spanned by two functions, $\tilde{u}_k(x)$ and $\tilde{u}_{2n-k}(x)$. If $n = 0$, then all eigenvalues of \mathcal{L}_n^2 are simple.

Generically, small perturbation of \mathcal{L}_n results in *splitting* of the double eigenvalues. Each of them can split into (i) two real eigenvalues of the perturbed operator or (ii) two complex-conjugate eigenvalues. If the case (i) takes place for each double eigenvalue, then small-amplitude localized solutions bifurcating from the n -th linear eigenstate are marginally stable, at least in some vicinity of the bifurcation. However, if at least for one double eigenvalue the case (ii) takes place, then the bifurcating small-amplitude solutions are unstable in vicinity of the bifurcation.

To address the splitting of double eigenvalues when passing from operator \mathcal{L}_n^2 to the perturbed one, $\mathcal{L}_+ \mathcal{L}_-$ in (4.18), we construct an *asymptotic expansion for perturbed eigenvalues* following [29]. Under the actions of the perturbation, each double eigenvalue $\tilde{\Lambda}_k$ splits into two simple ones:

$$\Lambda_{k,1} = \tilde{\Lambda}_k + \varepsilon^2 \gamma_1 + o(\varepsilon^2), \quad \Lambda_{k,2} = \tilde{\Lambda}_k + \varepsilon^2 \gamma_2 + o(\varepsilon^2), \quad (4.20)$$

where the coefficients $\gamma_{1,2}$ are the eigenvalues of the 2×2 matrix

$$\widetilde{M}_n = \begin{pmatrix} \langle M_n \tilde{u}_k, \tilde{u}_k \rangle & \langle M_n \tilde{u}_k, \tilde{u}_{2n-k} \rangle \\ \langle M_n \tilde{u}_{2n-k}, \tilde{u}_k \rangle & \langle M_n \tilde{u}_{2n-k}, \tilde{u}_{2n-k} \rangle \end{pmatrix}. \quad (4.21)$$

Therefore, if the eigenvalues of \widetilde{M}_n are real for each $k = 0, 1, \dots, n - 1$, then the spectrum of $\mathcal{L}_+ \mathcal{L}_-$ remains real and the nonlinear localized solution $u_n(x)$ is stable, at least for sufficiently small ε . Otherwise, if eigenvalues of \widetilde{M}_n are complex for some $k = 0, 1, \dots, n - 1$, then solution $u_n(x)$ is unstable in a vicinity of the bifurcation.

Note that, as no double eigenvalues exist for $n = 0$, the small-amplitude solutions of the family Γ_0 are stable for any $P(x)$.

Using explicit expressions for the eigenfunctions $\tilde{u}_n(x)$ from (4.15) and expressions for M_n from (4.19), one can compute the entries of the matrix \widetilde{M}_n :

$$\begin{aligned} \langle M_n \tilde{u}_k, \tilde{u}_k \rangle &= \frac{8(n-k)}{\pi 2^{(n+k)} n! k!} \int_{-\infty}^{+\infty} P(x) H_n^2(x) H_k^2(x) e^{-2x^2} dx \\ &\quad - \frac{4(n-k)}{\pi 2^{2n} (n!)^2} \int_{-\infty}^{+\infty} P(x) H_n^4(x) e^{-2x^2} dx; \end{aligned} \quad (4.22)$$

$$\begin{aligned} \langle M_n \tilde{u}_k, \tilde{u}_{2n-k} \rangle &= -\langle M_n \tilde{u}_{2n-k}, \tilde{u}_k \rangle = \\ &= \frac{4(n-k)}{\pi 2^{2n} n! \sqrt{k!(2n-k)!}} \int_{-\infty}^{+\infty} P(x) H_n^2(x) H_{2n-k}(x) H_k(x) e^{-2x^2} dx; \end{aligned} \quad (4.23)$$

$$\begin{aligned} \langle M_n \tilde{u}_{2n-k}, \tilde{u}_{2n-k} \rangle &= -\frac{8(n-k)}{\pi 2^{(3n-k)} n! (2n-k)!} \int_{-\infty}^{+\infty} P(x) H_n^2(x) H_{2n-k}^2(x) e^{-2x^2} dx \\ &\quad + \frac{4(n-k)}{\pi 2^{2n} (n!)^2} \int_{-\infty}^{\infty} P(x) H_n^4(x) e^{-2x^2} dx. \end{aligned} \quad (4.24)$$

Formulas (4.22) – (4.24) with $P(x) = \pm 1$ were used in [29] to explore the stability of small-amplitude nonlinear solutions in the model with constant pseudopotential.

4.3. Branches of Nonlinear Localized Solutions for Periodic Pseudopotential, $P(x) = P_0 + P_1 \cos(\Omega x)$

We present our numerical and analytical results for pseudopotential of the cosine form (4.8). It represents a sum of a constant part P_0 and a periodic part $P_1 \cos(\Omega x)$. In what follows below we conclude that the relation between the magnitudes of $|P_0|$ and $|P_1|$ is important. Hence, it's necessary to consider two cases separately: (a) $|P_0| \gtrsim |P_1|$, when the constant component is not negligible, and (b) $|P_0| \ll |P_1|$, when the constant component is negligible and pseudopotential (4.8)

should be treated as a function with zero mean. We consider each of these cases separately.

4.3.1. Periodic pseudopotential with Non-Zero Mean, $|P_0| \gtrsim |P_1|$

If P_0 component of pseudopotential is not negligible, one can scale out the absolute value of it, by replacing

$$\Psi \rightarrow \Psi / \sqrt{|P_0|}, \quad P_1 / |P_0| \rightarrow P_1. \quad (4.25)$$

Equation (4.4) takes form

$$i\Psi_t + \Psi_{xx} - x^2\Psi + (\sigma_0 + P_1 \cos(\Omega x))|\Psi|^2\Psi = 0. \quad (4.26)$$

where $\sigma_0 \equiv P_0 / |P_0| = \text{sign}(P_0)$. Stationary states equation in this case has form

$$u_{xx} + (\omega - x^2)u + (\sigma_0 + P_1 \cos(\Omega x))u^3 = 0. \quad (4.27)$$

A generic picture of localized solutions of equation (4.27) can be obtained by means of a numerical shooting algorithm. A representative example of the respective $N(\omega)$ curves with $\sigma_0 = 1$, $P_1 = 2$ (which implies that the sign of the pseudopotential periodically flips), and $\Omega = 12$ is displayed in Figure 4.2. One can immediately observe that, apart from branches Γ_n originating from their linear counterparts, numerous branches of localized solutions *without linear counterpart* exist too. Thus, the presence of the periodic component in the pseudopotential essentially enriches the diversity of available solutions. This contrasts with the case of nonlinear harmonic-oscillator with constant pseudopotential, see Figure 4.1. However, we did not find stable solutions without linear counterpart. On Figure 4.2 the only stables solutions correspond to branches Γ_0 , Γ_1 , Γ_2 .

Similar situation takes place for $\sigma_0 = -1$, while all other parameters remain the same, $P_1 = 2$ and $\Omega = 12$. Respective $N(\omega)$ curves are presented in Figure 4.3. Localized solutions without linear counterpart correspond to branches (a) and (b). Branches Γ_0 , Γ_1 have stability regions. All other families were found to be unstable.

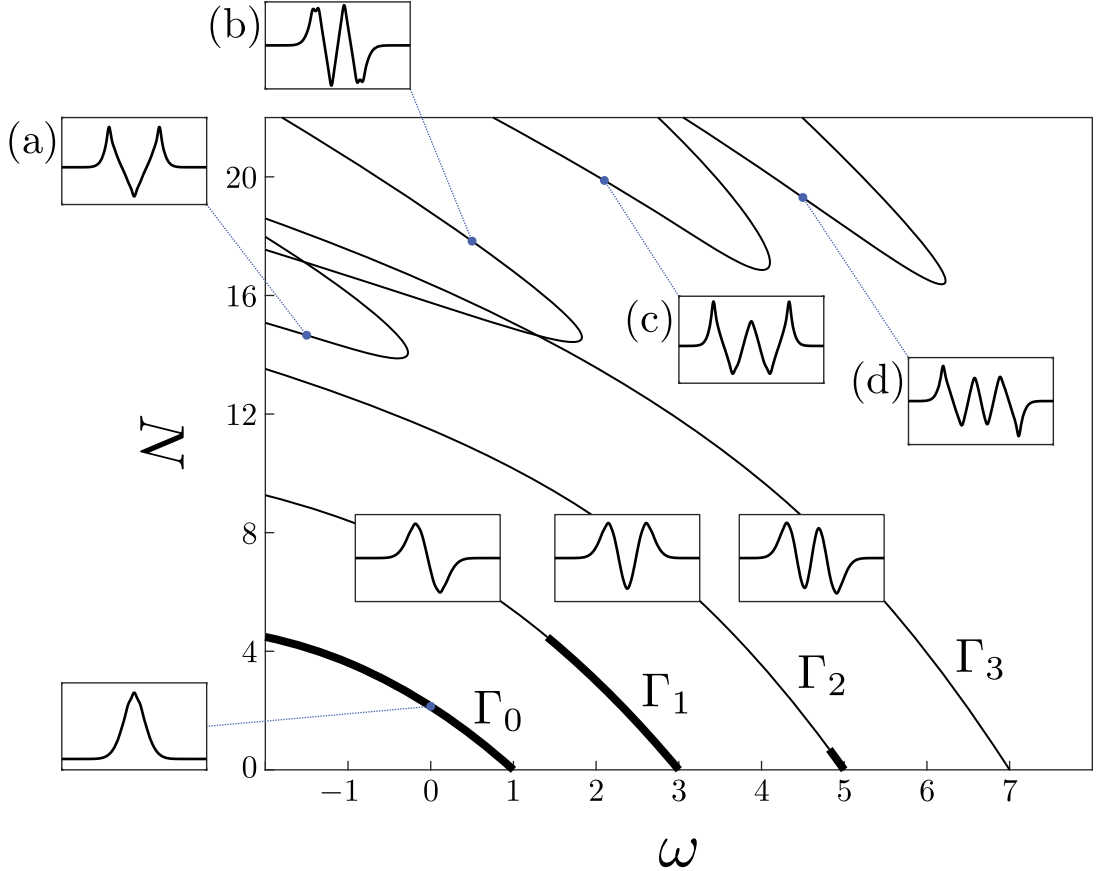


Figure 4.2. Curves $N(\omega)$ of localized solution families for equation (4.27) with non-zero mean cosine pseudopotential with $\sigma_0 = 1$, $P_1 = 2$, and $\Omega = 12$. Thin and bold lines show unstable and stable solution families. Branches Γ_n , $n = 0, 1, 2, 3$ represent solutions with linear counterpart. Insets on top and outside of the branches are representative profiles $u(x)$ of solutions obtained from the corresponding families. Branches (a), (b), (c), and (d) represent solutions without linear counterpart. All of them were found to be unstable.

In the limit of the rapidly oscillation of $P(x)$, $\Omega \rightarrow \infty$, localized solutions of (4.27) may be approximated by solutions of nonlinear harmonic-oscillator equation with constant pseudopotential (4.14). The asymptotic formula can be obtained by means of averaging with respect to fast oscillations (see, e.g. [30]):

$$u(x) = v(x) + \frac{1}{\Omega^2} \left(w(x) + P_1 w^3(x) \cos(\Omega x) \right) + o\left(\frac{1}{\Omega^2}\right), \quad \Omega \rightarrow \infty. \quad (4.28)$$

Here $v(x)$ is a solution of Eq. (4.14), and $w(x)$ is a localized solution of the linear equation

$$w_{xx} + (\omega - x^2 + 3\sigma_0 v^2(x))w = -\frac{3}{2}P_1^2 v^5(x). \quad (4.29)$$

We stress that asymptotic relation (4.28) is valid for nonlinear solutions of arbitrary

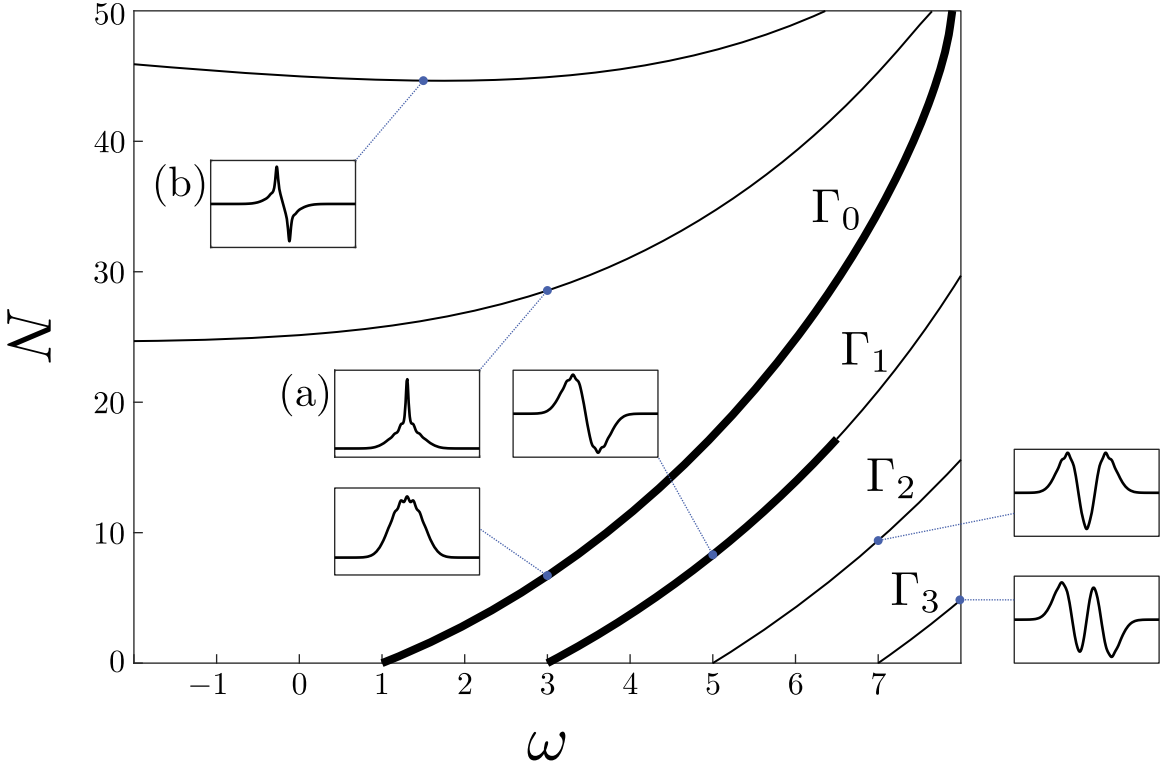


Figure 4.3. Curves $N(\omega)$ of localized solution families for equation (4.27) with non-zero mean cosine pseudopotential with $\sigma_0 = -1$, $P_1 = 2$, and $\Omega = 12$. Thin and bold lines show unstable and stable solution families. Branches Γ_n , $n = 0, 1, 2, 3$ represent solutions with linear counterpart, two of them, Γ_0 and Γ_1 , have regions of stability. All other families are unstable. Insets with blue dashed lines represent profiles $u(x)$ of the solutions.

amplitudes (i.e. not only in the small-amplitude limit), provided that Ω^2 is large enough.

Figure 4.4 shows the branches Γ_0 , Γ_1 , and Γ_2 for different spatial frequencies of the periodic pseudopotential, $\Omega = 8$, $\Omega = 12$, and $\Omega = 16$. For convenience in Figure 4.4 we use the following notation. We denote Γ_n branches of equation (4.14) for nonlinear harmonic-oscillator with constant pseudopotential with parameter $\sigma_0 = 1$. Branches Γ_n^Ω correspond to solutions of equation (4.27) with different frequencies Ω of pseudopotential. According to the asymptotic prediction (4.28), branches Γ_n^Ω approach the corresponding branches Γ_n of equation (4.14) as Ω grows. Additionally, Eq. (4.28) implies that stability of a localized solution under the action of the rapidly oscillating pseudopotential is determined by stability of its counterpart in the nonlinear harmonic-oscillator model (4.14) with constant pseudopotential.

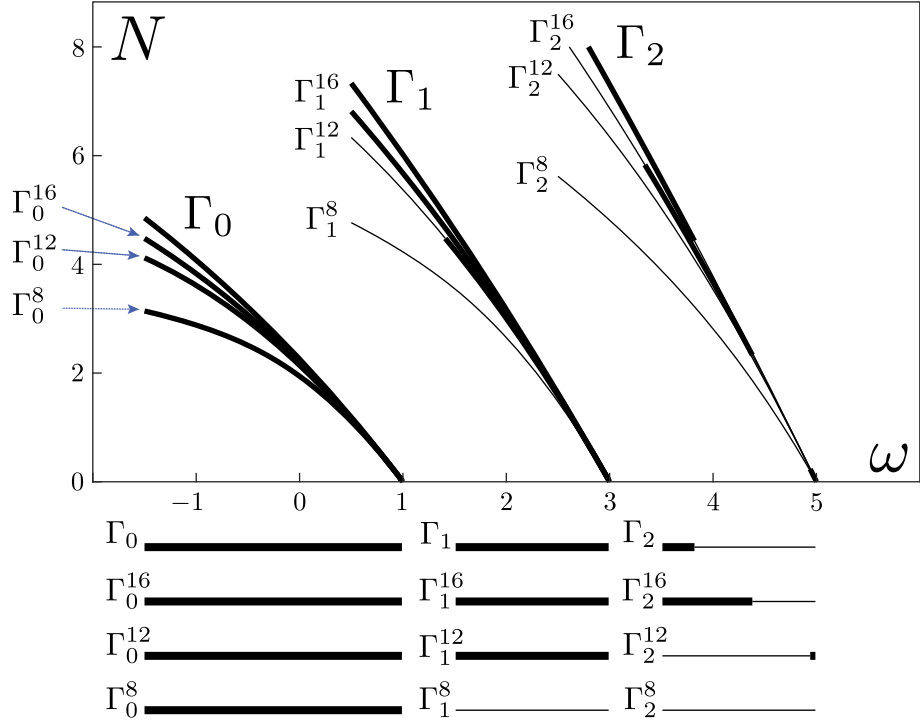


Figure 4.4. Curves $N(\omega)$ of branches Γ_n^Ω for equation (4.27) with $\sigma_0 = 1$, $P_1 = 2$, and $\Omega = 8, 12, 16$. Only branches with $n = 0, 1, 2$ are shown. For comparison, the corresponding dependencies Γ_n for nonlinear harmonic-oscillator (4.14) for the case $\sigma_0 = 1$ are show too. These curves are identical to those in Figure 4.1 (a). According to (4.28) branches Γ_n^Ω approaches Γ_n as Ω grows. Bold (thin) lines correspond to stable (unstable) solutions. For convenience the stability of the families Γ_n^Ω and Γ_n is duplicated by straight lines under the main plot.

tial. Indeed, the presence of eigenvalues with non-zero real parts in the perturbative spectrum of a nonlinear harmonic-oscillator solution implies the existence of such eigenvalues in the spectrum of the corresponding localized solution of (4.27) if Ω is large enough. For example, the segment of the branch Γ_1^8 (obtained for parameters $\sigma_0 = 1$, $P_1 = 2$, $\Omega = 8$) shown in Figure 4.4 is completely unstable, but stability of the corresponding family for $n = 1$ restores for higher values of Ω , which agrees with nonlinear harmonic-oscillator limit, where this branch is entirely stable. For the branch Γ_2 the situation is more complex. Small-amplitude solutions belonging to Γ_2^8 are unstable, but they become stable for Γ_2^{12} . However, Eq. (4.28) implies that the further increase of Ω will necessarily leads to the destabilization of these solutions (see branch Γ_2^{16}), because in the nonlinear harmonic-oscillator limit the small amplitude solutions belonging to Γ_2 are unstable.

To check predictions of the linear-stability analysis, we have performed simulations of the evolutions of localized solutions in the framework of time-dependent GPE (4.26), using an implicit finite-difference scheme from [24] that has been already used in Chapter 3. In the simulation, solutions which are predicted to be linearly stable keep their shape indefinitely long, see Figure 4.5 (e). Solutions that are predicted to be unstable typically transform into a pulsating object localized over one period of the pseudopotential, see Figure 4.5 (f).

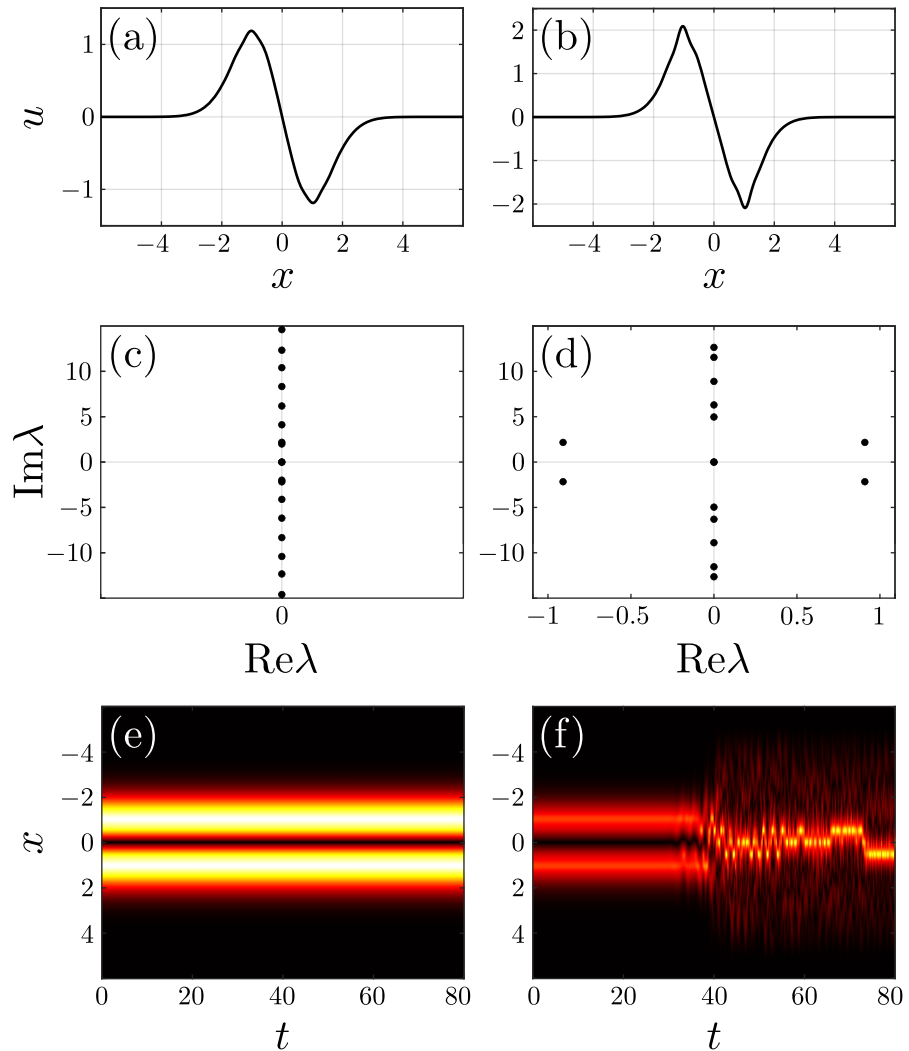


Figure 4.5. Results of stability analysis for solutions belonging to the branch Γ_1 of (4.26) with pseudopotential $P(x) = 1 + 2 \cos(12x)$, and different parameters of ω . Shapes $u(x)$ of the stationary solutions are presented in panels (a) and (b) $\omega = 2$ and $\omega = 0$. The linear-stability spectrums are in panels (c) and (d) correspondingly. The evolutionary simulations are presented in panels (e) and (f). Localized solution with parameter $\omega = 2$ is stable, while solutions with parameter $\omega = 0$ is unstable.

4.3.2. Periodic pseudopotential with Zero Mean, $|P_0| \ll |P_1|$

According to the results of the previous section, the effect of a rapidly oscillating pseudopotential with non-zero mean may be approximated using the standard nonlinear harmonic-oscillator model with uniform nonlinearity. However, the situation becomes essentially different for the case $|P_0| \ll |P_1|$. If P_0 component of the pseudopotential can be neglected, we drop P_0 , and rescale equation (4.4) by replacing

$$\Psi \rightarrow \Psi / \sqrt{|P_1|}, \quad (4.30)$$

which leads to the equation

$$i\Psi_t + \Psi_{xx} - x^2\Psi + \sigma_1 \cos(\Omega x)|\Psi|^2\Psi = 0, \quad (4.31)$$

where $\sigma_1 = P_1/|P_1| = \text{sign}(P_1)$. Stationary states equation has the form

$$u_{xx} + (\omega - x^2)u + \sigma_1 \cos(\Omega x)u^3 = 0. \quad (4.32)$$

The $N(\omega)$ curves for (4.32) with $\sigma_1 = 1$ and $\Omega = 8$ are shown in Figure 4.8. Here we again observe the branches Γ_n bifurcating from the linear limit and various families without linear counterparts, see branches (a), (b), (b'), (c), (d) in Figure 4.8. The branches Γ_n feature stable and unstable segments. Most part of the localized solutions without linear counterpart being unstable, however we found one branch without linear counterpart, family (b) on the corresponding inset of Figure 4.8, that features small stability region.

Let's focus on the localized solutions with linear counterpart under action of rapidly oscillating pseudopotential. In the limit N

1, weakly nonlinear solutions belonging to branches Γ_n , $n = 0, 1, \dots$, are produced by equations (4.15) where Δ_n is given by (4.16), with $P(x) = \sigma_1 \cos(\Omega x)$. The numerical found values of Δ_n , $n = 0, 1, 2$ for σ_1 and several different values of Ω are presented in Table 4.1.

To find the asymptotic form of Δ_n for $\Omega \rightarrow \infty$, we note that, for any arbitrary

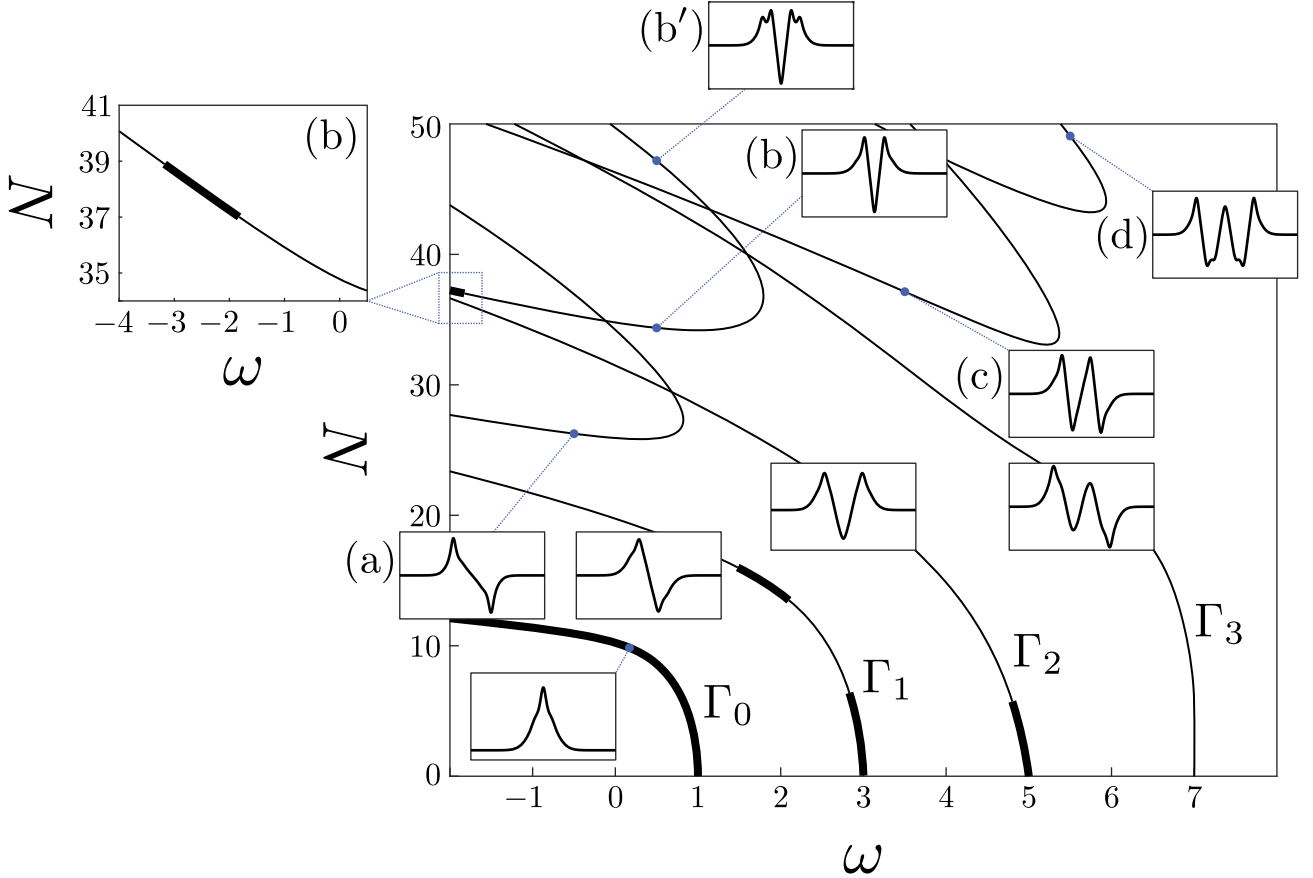


Figure 4.6. Curves $N(\omega)$ for localized solutions of equation (4.32) with parameters $\sigma_1 = 1$ and $\Omega = 8$. Thin and bold lines show unstable and stable solution families. Insets depicts profiles of the solutions. Additional window in the upper left corner shows stability region for solutions from the branch (b) without linear counterpart.

polynomial of degree $2m$

$$Q_{2m}(x) = a_{2m}x^{2m} + a_{2m-1}x^{2m-1} + \cdots + a_0, \quad (4.33)$$

the following asymptotic relation holds

$$\int_{-\infty}^{+\infty} Q_{2m}(x)e^{-2x^2} \cos(\Omega x) dx \approx (-1)^m \frac{a_{2m}\sqrt{2\pi}\Omega^{2m}}{2^{4m+1}} e^{-\Omega^2/8}, \quad \Omega \rightarrow \infty. \quad (4.34)$$

Since the coefficient in front of the highest-power term in the Hermite polynomial $H_n(x)$ is 2^n , equation (4.34) with $Q_{2m}(x)$ substituted by $H_n(x)$ yields

$$\Delta_n \approx \frac{\sqrt{2}\Omega^{4n}}{2^{6n+1}(n!)^2\sqrt{\pi}} e^{-\Omega^2/8}, \quad \Omega \rightarrow \infty. \quad (4.35)$$

Therefore, for sufficiently large Ω , Δ_n are all positive and decay exponentially, which agrees with the data in Table 4.1.

Ω	0	2	8	18
$n = 0$	$3.9894 \cdot 10^{-1}$	$2.4197 \cdot 10^{-1}$	$1.3383 \cdot 10^{-4}$	$1 \cdot 10^{-18}$
$n = 1$	$2.9921 \cdot 10^{-1}$	$-1.2100 \cdot 10^{-1}$	$5.4536 \cdot 10^{-3}$	$2 \cdot 10^{-15}$
$n = 2$	$2.5557 \cdot 10^{-1}$	$-1.3611 \cdot 10^{-1}$	$2.1097 \cdot 10^{-2}$	$5 \cdot 10^{-13}$

Table 4.1. The values of Δ_n , $n = 0, 1, 2$, calculated as per Eq. (4.16) for $P(x) = \cos(\Omega x)$, $\Omega = 0, 2, 8, 18$. They determine the perturbative shift of chemical potential of weakly nonlinear localized solutions, pursuant to Eq. (4.15).

In the small-amplitude limit, the stability of localized solutions with linear counterpart is determined by the eigenvalues of matrix \widetilde{M}_n , see (4.21). One can compute these eigenvalues numerically with any necessary accuracy. The results for two different values of frequency, $\Omega = 8$ and $\Omega = 16$, are summarized in Tables 4.2 and 4.3. In these tables, n is the index of the branch Γ_n . For instance, $n = 2$ means that the branch Γ_2 , which starts from $\tilde{\omega}_2 = 2 \cdot 2 + 1 = 5$, is under consideration. While k , running from 0 to $n - 1$, enumerates double eigenvalues $\tilde{\Lambda}_k = 4(n - k)^2$. Each cell with $n > k$ contains either two real numbers or symbol “ \mathbb{C} ”. These numbers are real eigenvalues of matrix \widetilde{M}_n , whereas symbol “ \mathbb{C} ” indicates that eigenvalues of \widetilde{M}_n are complex, and the corresponding low-amplitude solutions of the branch Γ_n are unstable. For $n < k$ the double eigenvalues do not exist (marked with dashes at the corresponding positions in the tables).

To be specific, let us describe in details the branch Γ_2 in the case of $P(x) = \cos(8x)$, Table 4.2. In this case, there are two double eigenvalues in the spectrum, $\tilde{\Lambda}_0 = 16$ and $\tilde{\Lambda}_1 = 4$. According to Table 4.2 and equation (4.20), they split as

$$\Lambda_{0,1} = 16 - 0.012 \cdot \varepsilon^2 + \dots, \quad \Lambda_{0,2} = 16 + 0.203 \cdot \varepsilon^2 + \dots; \quad (4.36)$$

$$\Lambda_{1,1} = 4 - 0.176 \cdot \varepsilon^2 + \dots, \quad \Lambda_{1,2} = 4 + 0.159 \cdot \varepsilon^2 + \dots. \quad (4.37)$$

Hence, the small-amplitude solutions belonging to branch Γ_2 are stable in this case. The situation is different for branches $\Gamma_{3,4,5}$ from Table 4.2. For each of these branches the bifurcation of a complex-conjugate pair occurs: for $n = 3$ the eigenvalue

	$n = 1$	$n = 2$	$n = 3$	$n = 4$	$n = 5$
$k = 0$	0.132	-0.012	\mathbb{C}	0.424	-0.845
	-0.028	0.203		-0.828	-0.660
$k = 1$	-	-0.176	0.432	-0.486	0.356
		0.159	-0.190	0.048	0.944
$k = 2$	-	-	-0.068	-0.206	0.531
			-0.132	0.196	-0.600
$k = 3$	-	-	-	\mathbb{C}	0.166
					-0.122
$k = 4$	-	-	-	-	\mathbb{C}

Table 4.2. Eigenvalues of matrix \widetilde{M}_n in the case $P(x) = \cos(8x)$. Here n is the index of branch Γ_n , and k enumerates double eigenvalues $\tilde{\Lambda}_k = 4(n-k)^2$. Each cell with $n > k$ contains either two real numbers or symbol “ \mathbb{C} ”. These numbers are real eigenvalues of matrix \widetilde{M}_n , whereas symbol “ \mathbb{C} ” indicates that eigenvalues of \widetilde{M}_n are complex, and the corresponding low-amplitude solutions of the branch Γ_n are unstable. Results in this table agree with Figure 4.8.

	$n = 1$	$n = 2$	$n = 3$	$n = 4$	$n = 5$
$k = 0$	$-2.0 \cdot 10^{-11}$	$-7.6 \cdot 10^{-9}$	$-8.7 \cdot 10^{-7}$	$-4.0 \cdot 10^{-5}$	$-9.5 \cdot 10^{-4}$
	$5.7 \cdot 10^{-10}$	$-9.2 \cdot 10^{-7}$	$2.2 \cdot 10^{-4}$	$-1.2 \cdot 10^{-2}$	$1.5 \cdot 10^{-1}$
$k = 1$	-	$-4.2 \cdot 10^{-9}$	$-5.8 \cdot 10^{-7}$	$-3.0 \cdot 10^{-5}$	$-7.6 \cdot 10^{-4}$
		$7.3 \cdot 10^{-8}$	$-3.6 \cdot 10^{-5}$	$3.3 \cdot 10^{-3}$	$-6.8 \cdot 10^{-2}$
$k = 2$	-	-	$-3.4 \cdot 10^{-7}$	$-2.0 \cdot 10^{-5}$	$-5.7 \cdot 10^{-4}$
			$3.9 \cdot 10^{-6}$	$-6.8 \cdot 10^{-4}$	$2.6 \cdot 10^{-2}$
$k = 3$	-	-	-	$-1.3 \cdot 10^{-5}$	$-3.6 \cdot 10^{-4}$
				$1.0 \cdot 10^{-4}$	$-6.8 \cdot 10^{-3}$
$k = 4$	-	-	-	-	$-2.7 \cdot 10^{-4}$
					$1.5 \cdot 10^{-3}$

Table 4.3. Eigenvalues of matrix \widetilde{M}_n for $P(x) = \cos(16x)$. The same notation as for Table 4.2 is used.

$\tilde{\Lambda}_0 = 36$ splits into complex eigenvalues, while for $n = 4$ and $n = 5$ the same happens for $\tilde{\Lambda}_2 = 4$. Therefore, for $\Omega = 8$ the small-amplitude solutions are stable for branches $\Gamma_{0,1,2}$, but unstable for $\Gamma_{3,4,5}$. Table 4.3 is produced for $\Omega = 16$. It implies that the small-amplitude solutions are stable for all branches $\Gamma_{1,\dots,5}$.

To explain the different stability of small-amplitude solutions with different values of frequency Ω , we consider the behaviour of the eigenvalues of \tilde{M}_n at $\Omega \rightarrow \infty$. Using explicit results given by equations (4.22)–(4.24) and asymptotic relation (4.35), we obtain

$$\langle M_n \tilde{u}_k, \tilde{u}_k \rangle \sim -\frac{2\sqrt{2}(n-k)\Omega^{4n}}{2^{6n}(n!)^2\sqrt{\pi}}e^{-\Omega^2/8}; \quad (4.38)$$

$$\langle M_n \tilde{u}_k, \tilde{u}_{2n-k} \rangle = -\langle M_n \tilde{u}_{2n-k}, \tilde{u}_k \rangle \sim \frac{2\sqrt{2}(n-k)\Omega^{4n}}{2^{6n}n!\sqrt{k!(2n-k)!}\sqrt{\pi}}e^{-\Omega^2/8}; \quad (4.39)$$

$$\langle M_n \tilde{u}_{2n-k}, \tilde{u}_{2n-k} \rangle \sim -\frac{4\sqrt{2}(n-k)\Omega^{2(3n-k)}}{\sqrt{\pi}2^{3(3n-k)}n!(2n-k)!}e^{-\Omega^2/8}. \quad (4.40)$$

These relations imply that

$$\tilde{M}_n = \begin{pmatrix} O(\Omega^{4n}e^{-\Omega^2/8}) & O(\Omega^{4n}e^{-\Omega^2/8}) \\ O(\Omega^{4n}e^{-\Omega^2/8}) & O(\Omega^{2(3n-k)}e^{-\Omega^2/8}) \end{pmatrix}, \quad \Omega \rightarrow \infty. \quad (4.41)$$

All elements of the matrix \tilde{M}_n are of the same order, except for the one in the right lower corner which is of greater order since $n > k$. It means that, for Ω large enough, eigenvalues of \tilde{M}_n are real, hence the solutions from branches Γ_n for arbitrary n are stable in the small-amplitude limit. This explains the difference between Table 4.2 and Table 4.3. The increase of the frequency from $\Omega = 8$ to $\Omega = 16$ results in stabilization of some small-amplitude solutions.

Results of our asymptotic findings are illustrated in Figure 4.7, where numerically generated $N(\omega)$ curves for $\Omega = 8$, $\Omega = 12$, and $\Omega = 16$ are depicted. It follows from these plots that the branch Γ_0 is the “most stable” one for all the three values of Ω . One also notices that, for the greatest value $\Omega = 16$ there exist a “stability window” in a vicinity of the bifurcations for all branches $\Gamma_{0,1,2,3}$, in agreement with the asymptotic results presented above.

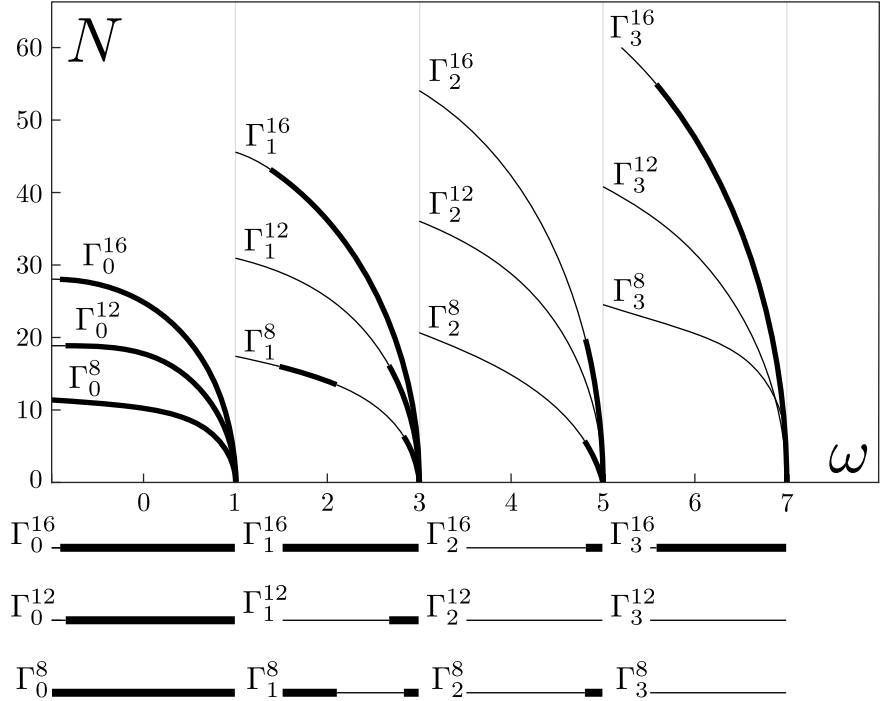


Figure 4.7. Curves $N(\omega)$ of branches Γ_n , $n = 0, 1, 2, 3$ for equation (4.32) with $\sigma_1 = 1$ and $\Omega = 8, 12, 16$. The following notation is used: branch Γ_n^Ω corresponds to the branch with linear counterpart Γ_n , obtained for equation (4.32) where the frequency of pseudopotential equals Ω . Bold (thin) lines correspond to stable (unstable) solutions. For convenience the stability of the families Γ_n^Ω is duplicated by straight lines under the main plot.

Numerical study of the temporal evolution of localized solutions in the framework of time-dependent GPE (4.4) confirms the prediction of the linear-stability analysis, see Figure 4.8. As an example of a distinctive pattern of dynamical behaviour of unstable stationary solution under small perturbation, in Figure 4.8 we display the transformation of an unstable solution from the branch Γ_1 into a pulsating object localized over one period of the pseudopotential $P(x) = \cos(8x)$.

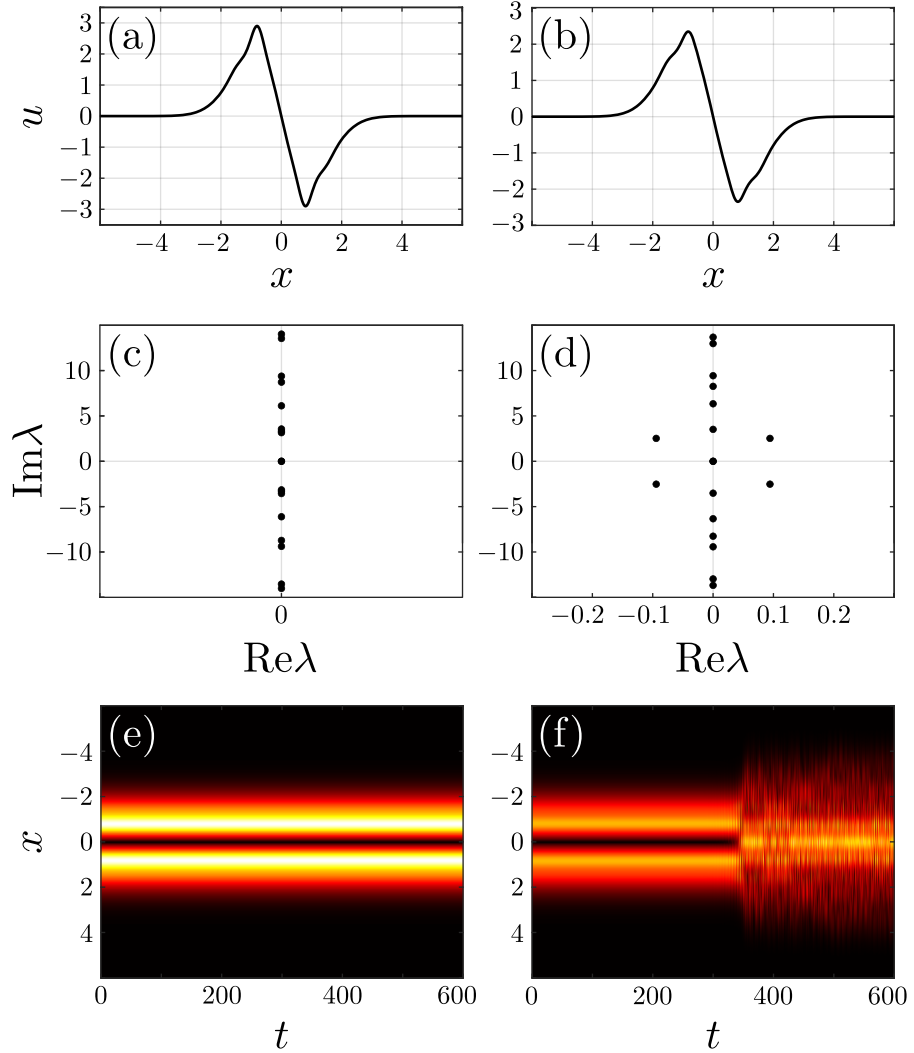


Figure 4.8. Results of stability analysis for solutions belonging to the branch Γ_1 of (4.31) with pseudopotential $P(x) = \cos(8x)$, and different parameters of ω . Shapes $u(x)$ of the stationary solutions are presented in panels (a) $\omega = 2$ and (b) $\omega = 2.5$. The linear-stability spectrums are in panels (c) and (d) correspondingly. The evolutionary simulations are presented in panels (e) and (f). Localized solution with parameter $\omega = 2$ is stable, while solutions with parameter $\omega = 2.5$ is unstable.

4.4. Summary

In this chapter we studied localized stationary solutions of Gross–Pitaevskii equation with the harmonic-oscillator potential and pseudopotential $P(x)$, which is a periodic function oscillating with spatial frequency Ω . Let's summarize our results. It was found that the presence of periodic pseudopotential significantly enrich the variety of localized solutions, in comparison with the well-studied case of the uniform nonlinearity (4.14). Specifically, GPE with periodic pseudopotential admits solutions without linear counterpart which do not exist in the case of $P(x) = \pm 1$. As concerns solutions bifurcating from eigenstate of linear problem, their properties are essentially different depending on the presence constant additive term in $P(x)$ (non-zero mean value). If the mean is non-zero, then properties of nonlinear solutions in a rapidly oscillating pseudopotential may be approximated using solutions for the standard nonlinear harmonic-oscillator model (with constant pseudopotential). However, the reduction to the standard model with constant nonlinearity does not work for the system with zero-mean periodic pseudopotential. Most interesting, in this we have found that the rapidly oscillating pseudopotential can stabilize small-amplitude localized solutions belonging to higher families, which are unstable in the model with $P(x)$ of non-zero mean. Specifically, for any given branch with index n , there exists a threshold value of the spatial frequency Ω_n , such that the small-amplitude solutions belonging to this branch are stable for $\Omega > \Omega_n$. All results of our work were published in [31].

Appendix A

Lemma on Bounded Solutions

Lemma (On bounded solutions). *Let $f(t, z)$ be defined for $t \geq t_0$, $|z| < +\infty$. Let $f(t, z)$ be a function that is continuous with respect to t , continuously differentiable with respect to z , and has the following properties:*

- (i) *for $|z| < \rho$, $\rho > 0$, the estimate $|f(t, z)| < \eta_\rho(t)|z|$ is valid, where $\eta_\rho(t) \in L_1(t_0; +\infty)$;*
- (ii) *for all z_1, z_2 such that $|z_{1,2}| < \rho$, $\rho > 0$, there exists a function $\tilde{\eta}_\rho(t) \in L_1(t_0; +\infty)$, such that $|f(t, z_2) - f(t, z_1)| \leq \tilde{\eta}_\rho(t)|z_2 - z_1|$;*
- (iii) *for $|z| < \rho$, $\rho > 0$, the estimate $|f_z(t, z)| < \theta_\rho(t)|z|$ is valid, where $\theta_\rho \in L_1(t_0, +\infty)$;*
- (iv) *for all z_1, z_2 such that $z_{1,2} < \rho$, $\rho > 0$, there exists function $\tilde{\theta}_\rho \in L_1(t_0; +\infty)$, such that $|f_z(t, z_2) - f_z(t, z_1)| \leq \tilde{\theta}_\rho|z_2 - z_1|$.*

Then for the equation

$$z_{tt} - \alpha z_t + f(t, z) = 0, \quad \alpha > 0 \quad (\text{A.1})$$

the following statements are valid:

- (A) *for each solution $z(t)$ of equation (A.1) that is bounded when $t \rightarrow +\infty$ there exists $C \in \mathbb{R}$ such that $z(t) \rightarrow C$ as $t \rightarrow +\infty$;*
- (B) *for each $C \in \mathbb{R}$ there exists unique solution $Z(t, C)$ of equation (A.1), defined on a segment $(t_C; +\infty)$, such that*

$$Z(t, C) = C + o(1), \quad t \rightarrow +\infty; \quad (\text{A.2})$$

- (C) *family of solutions $Z(t, C)$ is C^1 -smooth with respect to the parameter C .*

Proof. Let us prove the statement (A) first. Applying the method of variation of parameters one can find that a solution of equation (A.1) satisfies the equality:

$$z(t) = \varkappa_1 + \varkappa_2 e^{\alpha t} + \int_{t_0}^t e^{\alpha \eta} \left(\int_{\eta}^{+\infty} e^{-\alpha \xi} f(\xi, z(\xi)) d\xi \right) d\eta. \quad (\text{A.3})$$

It follows from the condition (i) that if $z(t)$ is bounded while $t \rightarrow +\infty$ then the integral

$$\int_{t_0}^{+\infty} e^{\alpha \eta} \left(\int_{\eta}^{+\infty} e^{-\alpha \xi} f(\xi, z(\xi)) d\xi \right) d\eta \quad (\text{A.4})$$

converges. Furthermore for all bounded solutions $\varkappa_2 = 0$, hence $z(t)$ tends to some constant for $t \rightarrow +\infty$. That proves the point (A).

Move on to the point (B). We make the change of variable $u(t) = z(t) - C$, where C is arbitrary constant. Rewrite equation (A.1) in the form of system of equations

$$y_t = Ay + F(t, y), \quad (\text{A.5})$$

where

$$y = \begin{pmatrix} u \\ v \end{pmatrix}, \quad A = \begin{pmatrix} 0 & 1 \\ 0 & \alpha \end{pmatrix}, \quad F(t, y) = \begin{pmatrix} 0 \\ f(t, u + C) \end{pmatrix}.$$

Now we apply Theorem 9.1 from [32, Chapter XII] to system (A.5). It states that (A.5) has a solution which tends to zero at infinity if the following conditions are satisfied:

- (1) function $F(t, y)$ is continuous and $\|F(t, y)\| \leq \lambda(t)$ for $t \in [t_0; +\infty)$, $\|y\| \leq \rho$, where $\lambda(t) \in L_1(t_0; +\infty)$;
- (2) for all $g(t) = \text{col}(g_1(t), g_2(t))$, $g(t) \in L_1(t_0; +\infty)$ there exists a solution $y(t) \in L_0^\infty(t_0; +\infty)$ of the inhomogeneous system

$$y_t = Ay + g(t); \quad (\text{A.6})$$

(hereinafter by $\|\cdot\|$ we denote the Euclidean norm in \mathbb{R}).

Firstly, due to condition (i) if $|u| \leq \rho$ and $t > t_0$ relation $\|f(t, u, C)\| \leq \rho\eta_\rho(t)$ takes place, moreover $\eta_\rho(t) \in L_1(t_0; +\infty)$, hence the condition (1) of the above-mentioned theorem is satisfied. Secondly, general solution of the inhomogeneous system of equations (A.6) can be written as:

$$u(t) = C_2 + \int_{t_0}^t \left(g_1(\eta) + e^{\alpha\eta} \left(C_1 - \int_{+\infty}^\eta e^{-\alpha\xi} g_2(\xi) d\xi \right) \right) d\eta; \quad (\text{A.7})$$

$$v(t) = u_t(t) - g_1(t). \quad (\text{A.8})$$

Since $g_{1,2}(t) \in L_1(t_0; +\infty)$ one can choose appropriate parameters C_1, C_2 in order to get a solution which tends to zero while $t \rightarrow +\infty$, so the condition (2) of the theorem is also met. Thereby both of the conditions for the applied theorem take place for the system (A.5). That implies existence of a solution $z(t)$ of (A.1) that approaches a given constant C while $t \rightarrow +\infty$ for all C .

Now we prove the uniqueness of such solution. Suppose that for the same C there exist two solutions $u_{1,2}(t)$ for equation

$$u_{tt} - \alpha u_t + f(t, u + C) = 0. \quad (\text{A.9})$$

Consider their difference $\Delta(t) = u_2(t) - u_1(t)$. It satisfies the equation

$$\Delta_{tt} - \alpha \Delta_t + R(t) \Delta = 0, \quad (\text{A.10})$$

and a boundary condition $\Delta \rightarrow 0$ as $t \rightarrow +\infty$. Here

$$R(t) \equiv \frac{f(t, u_2(t) + C) - f(t, u_1(t) + C)}{u_2(t) - u_1(t)}. \quad (\text{A.11})$$

Due to condition (ii) we can apply Theorem 11 from [33, Chapter 3]. It states that there exists a homeomorphism between the bounded solutions of the equation (A.10) and solutions of equation

$$\Delta_{tt} - \alpha \Delta_t = 0, \quad (\text{A.12})$$

moreover (see a note to that theorem in [33]) this homeomorphism is a linear map. It means that only a zero solution of (A.10) satisfies the zero asymptotic at infinity,

i.e. $u_2(t) \equiv u_1(t)$. Thus we have proved the existence of the family of solutions $Z(t, C)$ parametrised by $C \in \mathbb{R}$. Statement (B) is proved.

To prove the statement (C) one can note that the derivative

$$\frac{\partial Z}{\partial C}(t, C) \equiv \Theta(t, C) \quad (\text{A.13})$$

satisfies the equation (A.9) after differentiation with respect to C , moreover $\Theta(t, C) \rightarrow 0$ as $t \rightarrow +\infty$. We have

$$\Theta_{tt} - \alpha \Theta_t + f_z(t, u + C)\Theta + f_z(t, u + C) = 0. \quad (\text{A.14})$$

Here we can use Theorem 11 from [33, Chapter 3] again, and using the condition (iii) we can conclude that there exists a solution of this equation $\Theta(t, C)$ such that $\Theta(t, C) \rightarrow 0$ as $t \rightarrow +\infty$, and function $\Theta(t, C)$ is continuous with respect to the parameter C . That completes the proof of lemma. \square

Appendix B

Solutions of Duffing Equations

B.1. Equation with Positive Nonlinearity

Consider an equation

$$u_{xx} - u + u^3 = 0. \quad (\text{B.1})$$

The first integral of (B.1) is

$$H_0 = (u')^2 - u^2 + \frac{u^4}{2}. \quad (\text{B.2})$$

Equation (B.1) has three equilibria points: $u_* = 0$, and $u_* = \pm 1$. Its general solution can be written in terms of Jacobi elliptic functions as follows

$$u(x) = x_0 \operatorname{cn} \left(\sqrt{x_0^2 - 1} x + x_1, k \right), \quad x_0^2 - 1 \neq 0, \quad (\text{B.3})$$

where k is an elliptic modulus,

$$k = \sqrt{\frac{x_0^2}{2(x_0^2 - 1)}}, \quad (\text{B.4})$$

and x_0, x_1 are determined by initial conditions $u(0) = u_0, u'(0) = u'_0$:

$$\begin{cases} u(0) = u_0 = x_0 \operatorname{cn}(x_1, k); \\ u'(0) = u'_0 = -x_0 \sqrt{x_0^2 - 1} \operatorname{dn}(x_1, k) \operatorname{sn}(x_1, k). \end{cases} \quad (\text{B.5})$$

B.2. Equation with Negative Nonlinearity

Consider an equation

$$u_{xx} - u - u^3 = 0. \quad (\text{B.6})$$

The first integral of (B.6) is

$$H_* = (u')^2 - u^2 - \frac{u^4}{2}. \quad (\text{B.7})$$

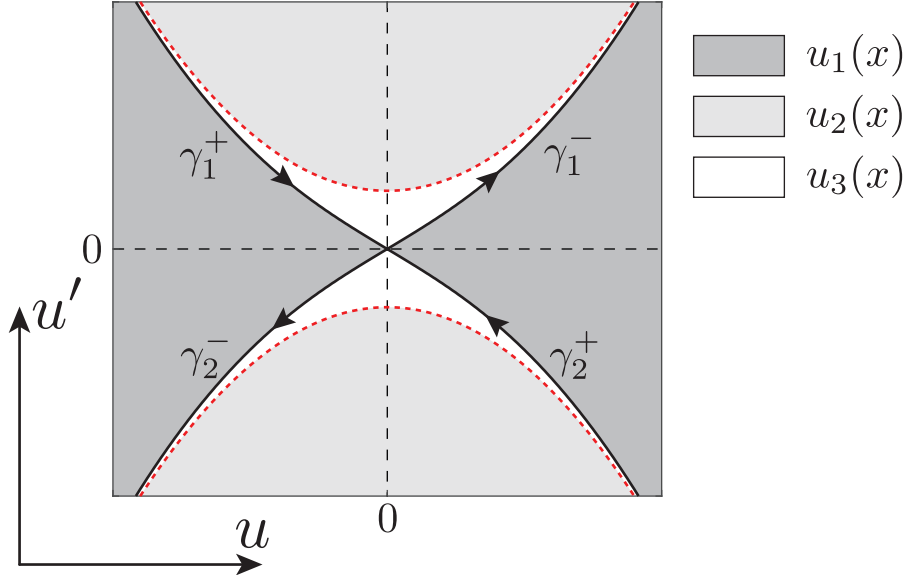


Figure B.1. Illustration to solutions of equation (B.6). Dark-gray, light-gray, and white areas correspond to solutions (B.8), (B.10), and (B.12). Black lines correspond to separatrices (B.9). Red dashed lines correspond to trajectories (B.11), they split areas (2) and (3) of solutions.

Equation (B.6) has one equilibria point: $u_* = 0$. It's convenient to illustrate the solutions of equation (B.6) by the following picture, see Figure B.1.

In dark-gray areas the solutions are

$$u_1(x) = \frac{\sqrt{2}}{\sqrt{2k^2 - 1}} \frac{\operatorname{dn}\left(\frac{x}{\sqrt{2k^2 - 1}}, k\right)}{\operatorname{sn}\left(\frac{x}{\sqrt{2k^2 - 1}}, k\right)}. \quad (\text{B.8})$$

The parameter k changes from $k = 1/\sqrt{2}$ to $k = 1$. When k approaches $1/\sqrt{2}$ the trajectories that correspond to (B.8) become more distant form the origin. When $k \rightarrow 1$ the trajectories approaches the separatrices $\gamma_{1,2}^\pm$

$$u(x) = \pm \frac{\sqrt{2}}{\sinh x}. \quad (\text{B.9})$$

Solutions (B.8) correspond to $H_* > 1/2$.

In white areas the solutions are

$$u_2(x) = \frac{1 - k^2}{\sqrt{k^2 + 1}} \frac{\operatorname{sn}\left(\frac{x}{\sqrt{2k^2 + 2}}, k\right)}{\operatorname{cn}\left(\frac{x}{\sqrt{2k^2 + 2}}, k\right) \operatorname{dn}\left(\frac{x}{\sqrt{2k^2 + 2}}, k\right)}. \quad (\text{B.10})$$

The parameter k changes from 0 to 1. When k approaches 1 the solutions $u_2(x)$

degenerates into zero solution. When k approaches 0 the solution becomes

$$u(x) = \pm \tan \frac{x}{\sqrt{2}}. \quad (\text{B.11})$$

The trajectories corresponding to (B.11) are shown by red dashed lines. For solutions of type (B.10), $0 < H_* < 1/2$.

In the light-gray areas the solutions are

$$u_3(x) = \frac{1}{\sqrt{1-2k^2}} \frac{\operatorname{sn}\left(\frac{x}{\sqrt{2-4k^2}}, k\right) \operatorname{dn}\left(\frac{x}{\sqrt{2-4k^2}}, k\right)}{\operatorname{cn}\left(\frac{x}{\sqrt{2-4k^2}}, k\right)}. \quad (\text{B.12})$$

The parameter k changes from $k = 0$ to $k = 1/\sqrt{2}$. When $k \rightarrow 0$, the solution (B.12) takes form (B.11). When $k \rightarrow 1/\sqrt{2}$ the corresponding trajectories becomes more distant from the origin. For solutions of type (B.12), $H_* < 0$.

Appendix C

Strips Mapping Theorems

Theorem (On h-strips mapping). *Let Poincaré map \mathcal{P} and its inverse \mathcal{P}^{-1} be defined on a complete (see Definition 8) island set $\bigcup_{i \in S} D_i$, where S is a finite or countable set of indices. Let for all $i, j \in S$ the set $V_{ij} = \mathcal{P}^{-1}(D_j) \cap D_i$ is non-empty, \mathcal{P} is defined on a closure $\overline{V_{ij}}$, and one of the following two conditions holds:*

(1) *the borders α_i^\pm of an island D_i are increasing curves, $\forall \mathbf{p} \in \overline{V_{ij}}$ the signs of $\{a_{mn}\}$ in the matrix of the linear operator $D\mathcal{P}_{\mathbf{p}} = (a_{mn})$ have exactly one of the following configurations*:*

$$(a) (+ +), \quad (b) (- -), \quad (c) (+ +), \quad (d) (- -);$$

and at the same time the borders α_j^\pm of D_j are increasing curves for cases (a), (b), and decreasing curves for (c), (d);

(2) *the borders α_i^\pm of an island D_i are decreasing curves, $\forall \mathbf{p} \in \overline{V_{ij}}$ signs of $\{a_{mn}\}$ in the matrix of the linear operator $D\mathcal{P}_{\mathbf{p}} = (a_{mn})$ have exactly one of the following configurations:*

$$(a) (+ -), \quad (b) (- +), \quad (c) (+ -), \quad (d) (- +);$$

and at the same time borders α_j^\pm of D_j are decreasing curves for cases (a), (b), and increasing for (c), (d);

and moreover $\exists \mu > 1$ such that $\forall p \in \overline{V_{ij}}, |a_{11}| \geq \mu$. Then

- (i) *for any h-strip $H \in D_i$, $\mathcal{P}(H) \cap D_j = \tilde{H}_j$ is also an h-strip;*
- (ii) *$d_h(\tilde{H}_j) \leq (1/\mu)d_h(H)$ (here $d_h(\cdot)$ is an h-strip thickness in a sence of Definition 9).*

*By “+” and “-” sign we mean strict inequalities $a_{mn} > 0$, $a_{mn} < 0$ to be held.

Proof. Let's fix indices i, j and prove the theorem for a pair of islands D_i, D_j . Consider the case (1a), other cases can be treated in an analogous way. Denote by $\mathbf{e}_1, \mathbf{e}_2$ the vectors

$$\mathbf{e}_1 = \begin{pmatrix} 1 \\ 0 \end{pmatrix}; \quad \mathbf{e}_2 = \begin{pmatrix} 0 \\ 1 \end{pmatrix}. \quad (\text{C.1})$$

Define the following set of *cones*:

$$\begin{aligned} \mathbb{R}_{++}^2 &= \{\mathbf{v} \mid \mathbf{v} = x\mathbf{e}_1 + y\mathbf{e}_2, x > 0, y > 0\}; \\ \overline{\mathbb{R}}_{++}^2 &= \{\mathbf{v} \mid \mathbf{v} = x\mathbf{e}_1 + y\mathbf{e}_2, x \geq 0, y \geq 0\}; \\ \mathbb{R}_{+-}^2 &= \{\mathbf{v} \mid \mathbf{v} = x\mathbf{e}_1 + y\mathbf{e}_2, x > 0, y < 0\}; \\ \overline{\mathbb{R}}_{+-}^2 &= \{\mathbf{v} \mid \mathbf{v} = x\mathbf{e}_1 + y\mathbf{e}_2, x \geq 0, y \leq 0\}; \\ \mathbb{R}_{-+}^2 &= \{\mathbf{v} \mid \mathbf{v} = x\mathbf{e}_1 + y\mathbf{e}_2, x < 0, y > 0\}; \\ \overline{\mathbb{R}}_{-+}^2 &= \{\mathbf{v} \mid \mathbf{v} = x\mathbf{e}_1 + y\mathbf{e}_2, x \leq 0, y \geq 0\}; \\ \mathbb{R}_{--}^2 &= \{\mathbf{v} \mid \mathbf{v} = x\mathbf{e}_1 + y\mathbf{e}_2, x < 0, y < 0\}; \\ \overline{\mathbb{R}}_{--}^2 &= \{\mathbf{v} \mid \mathbf{v} = x\mathbf{e}_1 + y\mathbf{e}_2, x \leq 0, y \leq 0\}. \end{aligned}$$

As the first step of the proof, we show that the signs of entries of the matrix of linear operator $D\mathcal{P}_{\mathbf{p}} = (a_{mn})$ uniquely determine the mapping of the cones in each point \mathbf{p} of the set $\overline{V_{ij}}$. For the case (a) we have:

$$\forall \mathbf{v} = \begin{pmatrix} x \\ y \end{pmatrix} \in \overline{\mathbb{R}}_{++}^2, \quad D\mathcal{P}_{\mathbf{p}}(\mathbf{v}) = \begin{pmatrix} a_{11} & a_{12} \\ a_{21} & a_{22} \end{pmatrix} \begin{pmatrix} x \\ y \end{pmatrix} = \begin{pmatrix} \tilde{x} > 0 \\ \tilde{y} > 0 \end{pmatrix} \in \mathbb{R}_{++}^2.$$

It is easy to check that in the case (1) $D\mathcal{P}_{\mathbf{p}}$ maps the cones as follows:

- (a) $D\mathcal{P}_{\mathbf{p}}(\overline{\mathbb{R}}_{++}^2) \in \mathbb{R}_{++}^2, \quad D\mathcal{P}_{\mathbf{p}}(\overline{\mathbb{R}}_{--}^2) \in \mathbb{R}_{--}^2;$
- (b) $D\mathcal{P}_{\mathbf{p}}(\overline{\mathbb{R}}_{++}^2) \in \mathbb{R}_{--}^2, \quad D\mathcal{P}_{\mathbf{p}}(\overline{\mathbb{R}}_{--}^2) \in \mathbb{R}_{++}^2;$
- (c) $D\mathcal{P}_{\mathbf{p}}(\overline{\mathbb{R}}_{++}^2) \in \mathbb{R}_{-+}^2, \quad D\mathcal{P}_{\mathbf{p}}(\overline{\mathbb{R}}_{-+}^2) \in \mathbb{R}_{--}^2;$
- (d) $D\mathcal{P}_{\mathbf{p}}(\overline{\mathbb{R}}_{++}^2) \in \mathbb{R}_{-+}^2, \quad D\mathcal{P}_{\mathbf{p}}(\overline{\mathbb{R}}_{-+}^2) \in \mathbb{R}_{--}^2.$

In the case (2) one has:

- (a) $D\mathcal{P}_{\mathbf{p}}(\overline{\mathbb{R}}_{-+}^2) \in \mathbb{R}_{-+}^2, D\mathcal{P}_{\mathbf{p}}(\overline{\mathbb{R}}_{+-}^2) \in \mathbb{R}_{+-}^2;$
- (b) $D\mathcal{P}_{\mathbf{p}}(\overline{\mathbb{R}}_{-+}^2) \in \mathbb{R}_{+-}^2, D\mathcal{P}_{\mathbf{p}}(\overline{\mathbb{R}}_{+-}^2) \in \mathbb{R}_{-+}^2;$
- (c) $D\mathcal{P}_{\mathbf{p}}(\overline{\mathbb{R}}_{-+}^2) \in \mathbb{R}_{--}^2, D\mathcal{P}_{\mathbf{p}}(\overline{\mathbb{R}}_{+-}^2) \in \mathbb{R}_{++}^2;$
- (d) $D\mathcal{P}_{\mathbf{p}}(\overline{\mathbb{R}}_{-+}^2) \in \mathbb{R}_{++}^2, D\mathcal{P}_{\mathbf{p}}(\overline{\mathbb{R}}_{+-}^2) \in \mathbb{R}_{--}^2.$

At a second step we show that this mapping preserves Lipschitz and monotonicity properties for curves from $\overline{V_{ij}}$ under \mathcal{P} action. Let us show that for the case (1a). Note that compactness of $\overline{V_{ij}}$ implies that the supremum exists:

$$\tilde{\gamma}_{ij} = \sup \frac{y}{x}, \begin{pmatrix} x \\ y \end{pmatrix} = D\mathcal{P}_{\mathbf{p}}(\mathbf{v}), \mathbf{p} \in \overline{V_{ij}}, \mathbf{v} \in \overline{\mathbb{R}}_{++}^2.$$

Further, let $\mathbf{p}_1, \mathbf{p}_2 \in \overline{V_{ij}}$, $\mathbf{p}_1 = (\psi_1, \psi'_1)$, $\mathbf{p}_2 = (\psi_2, \psi'_2)$, be two different points such that $\psi_2 \geq \psi_1$, $\psi'_2 \geq \psi'_1$. Let points $\mathbf{q}_1, \mathbf{q}_2$ be the \mathcal{P} -images of the points $\mathbf{p}_1, \mathbf{p}_2$ correspondingly, $\mathcal{P}(\mathbf{p}_1) = \mathbf{q}_1 = (\phi_1, \phi'_1)$, $\mathcal{P}(\mathbf{p}_2) = \mathbf{q}_2 = (\phi_2, \phi'_2)$. Let $D\mathcal{P}_{\mathbf{p}_1}$ be linearization of \mathcal{P} at the point \mathbf{p}_1 . Then the following expansion is valid:

$$\mathbf{q}_2 = \mathcal{P}(\mathbf{p}_2) = \mathbf{q}_1 + D\mathcal{P}_{\mathbf{p}_1}(\mathbf{p}_2 - \mathbf{p}_1) + r(||\mathbf{p}_2 - \mathbf{p}_1||), \quad (\text{C.2})$$

where $r(||\mathbf{p}_2 - \mathbf{p}_1||)/||\mathbf{p}_2 - \mathbf{p}_1|| \rightarrow 0$ as $||\mathbf{p}_2 - \mathbf{p}_1|| \rightarrow 0$ (here $||\cdot||$ is a Euclidean norm). Vector $\mathbf{p}_\Delta = \mathbf{p}_2 - \mathbf{p}_1 \in \overline{\mathbb{R}}_{++}^2$, that means that $D\mathcal{P}_{\mathbf{p}_1}(\mathbf{p}_\Delta) = \mathbf{q}_\Delta \in \mathbb{R}_{++}^2$, and

$$\mathbf{q}_2 - \mathbf{q}_1 = \mathbf{q}_\Delta + r(||\mathbf{p}_2 - \mathbf{p}_1||). \quad (\text{C.3})$$

The expression above implies that for “close enough” points $\mathbf{p}_1, \mathbf{p}_2$ their images satisfy the relation $\mathbf{q}_2 - \mathbf{q}_1 \in \mathbb{R}_{++}^2$, i.e. $\phi_2 > \phi_1, \phi'_2 > \phi'_1$. Moreover one can choose a value $\gamma_{ij} > \widetilde{\gamma}_{ij}$ such that the following inequality holds:

$$0 < \phi'_2 - \phi'_1 < \gamma_{ij}(\phi_2 - \phi_1). \quad (\text{C.4})$$

This ordering is transitive, i.e. (C.4) and the relation for “close enough” point $\mathbf{p}_2, \mathbf{p}_3$,

$$0 < \phi'_3 - \phi'_2 < \gamma_{ij}(\phi_3 - \phi_2), \quad (\text{C.5})$$

imply analogous relation for the points $\mathbf{p}_1, \mathbf{p}_3$ as well. That allows to extend relation (C.4) over all points $\mathbf{p}_1, \mathbf{p}_2 \in \overline{V_{ij}}$ that satisfies the conditions $\psi_2 \geq \psi_1, \psi'_2 \geq \psi'_1$. Other cases (1b)-(1d), (2a)-(2d) can be considered in a similar way.

Thus for the case (1) for all points $\mathbf{p}_1, \mathbf{p}_2 \in \overline{V_{ij}}$, such that $\psi_2 \geq \psi_1, \psi'_2 \geq \psi'_1$, the coordinates of their \mathcal{P} -images $\mathbf{q}_1 = (\phi_1, \phi'_1), \mathbf{q}_2 = (\phi_2, \phi'_2)$ satisfy one of the following inequalities ($\exists \gamma_{ij}$):

$$(a) \quad 0 < \phi'_2 - \phi'_1 < \gamma_{ij}(\phi_2 - \phi_1); \quad (\text{C.6a})$$

$$(b) \quad 0 < \phi'_1 - \phi'_2 < \gamma_{ij}(\phi_1 - \phi_2); \quad (\text{C.6b})$$

$$(c) \quad 0 < \phi'_1 - \phi'_2 < \gamma_{ij}(\phi_2 - \phi_1); \quad (\text{C.6c})$$

$$(d) \quad 0 < \phi'_2 - \phi'_1 < \gamma_{ij}(\phi_1 - \phi_2). \quad (\text{C.6d})$$

Similarly, for the case (2) for all points $\mathbf{p}_1, \mathbf{p}_2 \in \overline{V_{ij}}$, such that $\psi_2 \leq \psi_1, \psi'_2 \geq \psi'_1$, the \mathcal{P} -images obey one of the following inequalities:

$$(a) \quad 0 < \phi'_2 - \phi'_1 < \gamma_{ij}(\phi_1 - \phi_2); \quad (\text{C.7a})$$

$$(b) \quad 0 < \phi'_1 - \phi'_2 < \gamma_{ij}(\phi_2 - \phi_1); \quad (\text{C.7b})$$

$$(c) \quad 0 < \phi'_1 - \phi'_2 < \gamma_{ij}(\phi_1 - \phi_2); \quad (\text{C.7c})$$

$$(d) \quad 0 < \phi'_2 - \phi'_1 < \gamma_{ij}(\phi_2 - \phi_1). \quad (\text{C.7d})$$

As the third step we show that for any h-strip $H \in D_i$ its image $\mathcal{P}H \cap D_j = \tilde{H}_j$ is also an h-strip. Let an h-strip $H \in D_i$ be situated between two monotonic h-curves $\tilde{\alpha}_i^\pm$. The endpoints of the $\tilde{\alpha}_i^\pm$ belong to the boundaries β_i^\pm of the island D_i , so H is a curvilinear quadrangle bounded by the curves $\tilde{\alpha}_i^\pm$ and segments of the curves β_i^\pm . For the case (1a) of the theorem the curves $\tilde{\alpha}_i^\pm$ are increasing. Let's consider \mathcal{P} -image of the curve $\tilde{\alpha}_i^+$. According to the definition of complete island set $\mathcal{P}(\tilde{\alpha}_i^+)$ crosses each of the boundaries β_j^\pm of island D_j at least once. At the same time $\mathcal{P}(\tilde{\alpha}_i^+)$ cannot cross the boundaries α_j^\pm because they consist of points which tends to infinity under the action of \mathcal{P}^{-1} .

Let $\mathcal{P}(\tilde{\alpha}_i^+)$ cross one of the boundaries β_j^\pm of the island D_j twice. Denote those intersection points by $\mathbf{q}_1 = \mathcal{P}(\mathbf{p}_1), \mathbf{q}_2 = \mathcal{P}(\mathbf{p}_2)$. For the case (1a) the boundaries α_j^\pm

are increasing curves, and β_j^\pm are decreasing ones, hence the points $\mathbf{q}_1, \mathbf{q}_2$ belong to a decreasing curve. From the other side points $\mathbf{p}_1, \mathbf{p}_2 \in \overline{V_{ij}}$ belong to increasing curve $\tilde{\alpha}_i^+$, and hence for their \mathcal{P} -images $\mathbf{q}_1 = (\phi_1, \phi'_1), \mathbf{q}_2 = (\phi_2, \phi'_2)$ inequality (C.6a) holds. This inequality imples that points $\mathbf{q}_1, \mathbf{q}_2$ cannot belong to a decreasing curve, and $\mathcal{P}(\tilde{\alpha}_i^+)$ cross each boundary β_j^\pm only once. Similar statement is valid also for $\mathcal{P}(\tilde{\alpha}_i^-)$. Thereby $\mathcal{P}(\tilde{\alpha}_i^\pm) \cap D_j$ are monotonic curves. Their type of monotonicity coincides with the type of monotonicity of corresponding boundaries of the island D_j , moreover these curves bound the set $\mathcal{P}H \cap D_j$, hence $\mathcal{P}H \cap D_j = \tilde{H}_j$ is an h-strip. Other cases can be considered in a similar way using the corresponding inequalities (C.6b) – (C.6d), (C.7a) – (C.7d).

Finally, at the fourth step of this proof we show that under the given constraint on the entry a_{11} , for all h-strip $H \in D_i$, $\rho(\tilde{H}_j) \leq \mu\rho(H)$, so that thickness of \mathcal{P} -image of an h-strip within the island D_j is less than thickness of an original h-strip inside the island D_i . To prove that first assume that h-strips H and \tilde{H}_j are well-measured in a sense on Definition 10. Let the thickness of the h-strip \tilde{H}_j be measured along the vertical curve connecting points $\mathbf{q}_1 = (\phi_1, \phi'_1), \mathbf{q}_2 = (\phi_2, \phi'_2)$, $\phi'_1 < \phi'_2$. Consider a parametrization of that curve $\mathbf{q}(t) = (0, \phi'(t))$, where

$$\phi'(t) = t\phi'_2 + (1-t)\phi'_1, \quad 0 \leq t \leq 1. \quad (\text{C.8})$$

Strip \tilde{H}_j is well-measurable, so the curve $\mathbf{q}(t)$ entirely belongs to \tilde{H}_j . Since $\tilde{H}_j = \mathcal{P}H \cap D_j$ there exists a pre-image $\mathbf{p}(t) = \mathcal{P}^{-1}(\mathbf{q}(t)) = (\psi(t), \psi'(t)), \mathbf{p}(t) \subset H$ and $\mathbf{q}(t) = \mathcal{P}(\mathbf{p}(t))$. For the case (1a) let's demonstrate that in (u, u') coordinates $\mathbf{p}(t)$ is a decreasing curve connecting point from the opposite boundaries $\tilde{\alpha}_i^\pm$ of the strip H inside D_i . The curve $\mathbf{q}(t)$ belongs to some set which is a \mathcal{P} -image of a part of the set $\overline{V_{ij}}$. The signs of the entries of the matrix of $D\mathcal{P}_{\mathbf{p}}$, $\mathbf{p} \in \overline{V_{ij}}$ have the form $(\pm\pm)$, so the signs of the entries of the linearized inverse map $D\mathcal{P}_{\mathbf{q}}^{-1}$ have a configuration $(\pm\mp)$ on the curve $\mathbf{q}(t)$. This allows to conclude that the mapping of corresponding cones satisfies the conditions:

$$D\mathcal{P}_{\mathbf{q}(t)}^{-1}(\overline{\mathbb{R}}_{-+}^2) \in \mathbb{R}_{-+}^2, \quad D\mathcal{P}_{\mathbf{q}(t)}^{-1}(\overline{\mathbb{R}}_{+-}^2) \in \mathbb{R}_{+-}^2. \quad (\text{C.9})$$

Therefore the monotonicity property (C.7a) takes place. It immediately follows from (C.7a) that the vertical curve $\mathbf{q}(t)$ is mapped to the decreasing curve $\mathbf{p}(t)$. Moreover the inequality $\phi'_1 < \phi'_2$ provides that $\psi'(t) > 0$.

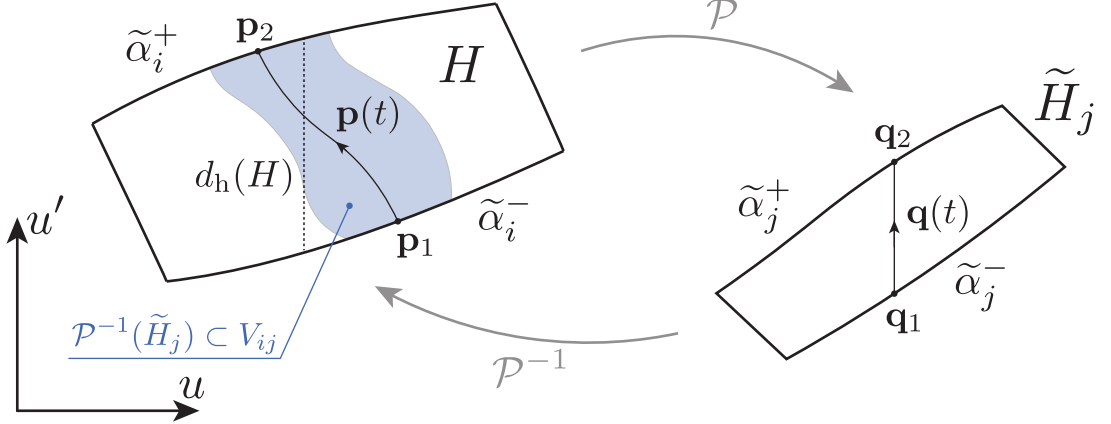


Figure C.1. Illustration to the proof of the point (ii) for the case when both h-strips H and \tilde{H}_j are well-measurable. Thickness of H is measured along the vertical dotted line, thickness of \tilde{H}_j is measured along the vertical line $\mathbf{q}(t)$. Arrows indicate the direction of motion along the curves while t changes from 0 to 1. Pre-image of \tilde{H}_j strip is colored gray.

Consider tangent vectors to $\mathbf{p}(t)$ and $\mathbf{q}(t)$ (upper dot means the derivative with respect to t):

$$\dot{\mathbf{p}}(t) = (\dot{\psi}(t), \dot{\psi}'(t)); \quad (\text{C.10})$$

$$\dot{\mathbf{q}}(t) = (0, \dot{\phi}'(t)). \quad (\text{C.11})$$

In each point t they are connected by the $D\mathcal{P}_{\mathbf{p}(t)}$ operator

$$\dot{\mathbf{q}}(t) = D\mathcal{P}_{\mathbf{p}(t)}(\dot{\mathbf{p}}(t)). \quad (\text{C.12})$$

Rewrite this relation in a matrix form:

$$\begin{pmatrix} a_{11}(t) & a_{12}(t) \\ a_{21}(t) & a_{22}(t) \end{pmatrix} \begin{pmatrix} \dot{\psi}(t) \\ \dot{\psi}'(t) \end{pmatrix} = \begin{pmatrix} 0 \\ \dot{\phi}'(t) \end{pmatrix}. \quad (\text{C.13})$$

We take into account that matrix (a_{mn}) is a linearization of Poincaré map therefore its determinant $a_{11}(t)a_{22}(t) - a_{12}(t)a_{21}(t) = 1$ in each point t . From the relations above and the conditions of theorem on values of $a_{11}(t)$ it follows that

$$\dot{\phi}'(t) = \frac{1}{a_{11}(t)}\dot{\psi}'(t) \leq \frac{1}{\mu}\dot{\psi}'(t). \quad (\text{C.14})$$

Integration of (C.14) with limits $0 \leq t \leq 1$ gives:

$$d_h(\tilde{H}_j) = \phi'_2 - \phi'_1 = \int_0^1 \dot{\phi}'(t) dt \leq \frac{1}{\mu} \int_0^1 \dot{\psi}'(t) dt = \frac{1}{\mu} (\psi'_2 - \psi'_1). \quad (\text{C.15})$$

Curve $\mathbf{p}(t)$ is decreasing and boundaries of H are increasing curves, so it follows from geometric considerations that $\psi'_2 - \psi'_1 \leq d_h(H)$, i.e. $d_h(\tilde{H}_j) \leq (1/\mu)d_h(H)$. That gives the final statement of the theorem for well-measurable strips.

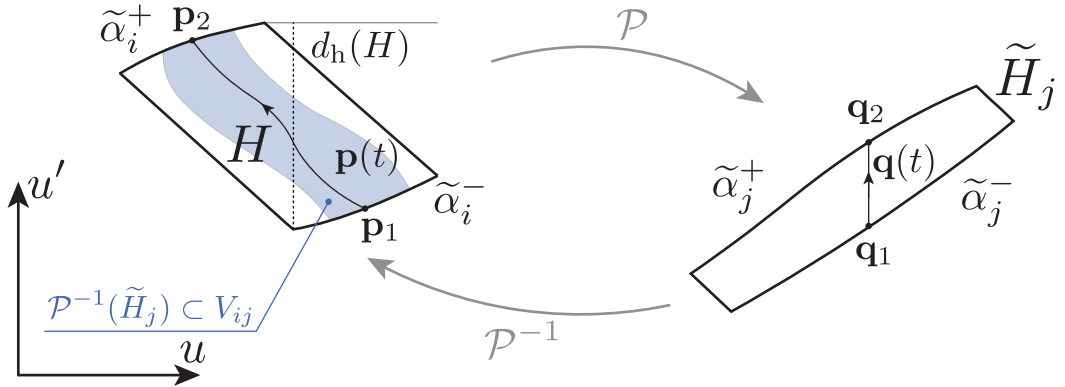


Figure C.2. Illustration to the proof of the point (ii) for the case when h-strip H is not well-measurable. Its thickness is measured along the vertical dotted line. One endpoint of that line does not belong to the strip boundary $\tilde{\alpha}_i^+$. Pre-image of \tilde{H}_j strip is colored with gray.

The proof above can be easily generalized to the cases when h-strips H and \tilde{H}_j are not well-measurable. If strip H is not well-measurable, the inequality $\psi'_2 - \psi'_1 \leq d_h(H)$ in (C.15) takes place also. This fact is illustrated on Figure C.2. Vertical distance between points $\mathbf{p}_1, \mathbf{p}_2$ turns out to be certainly less than the width of H strip.

In the case when h-strip \tilde{H}_j is not well-measurable, one should choose corner points $\mathbf{q}_1, \mathbf{q}_2$ in a such way that the vertical distance between them is equal to the thickness of \tilde{H}_j , and then connect $\mathbf{q}_1, \mathbf{q}_2$ with a monotonic decreasing curve $\mathbf{q}(t)$, see Fig. C.3. This is always possible due to the geometric properties of not well-measurable h-strip. According to the choice of points $\mathbf{q}_1, \mathbf{q}_2$, $d_h(\tilde{H}_j) = \phi_2 - \phi_1$, and all the steps above remain valid since the corresponding cones mapping with all the consequences can be also applied for the decreasing curves $\mathbf{p}(t)$ and $\mathbf{q}(t)$.

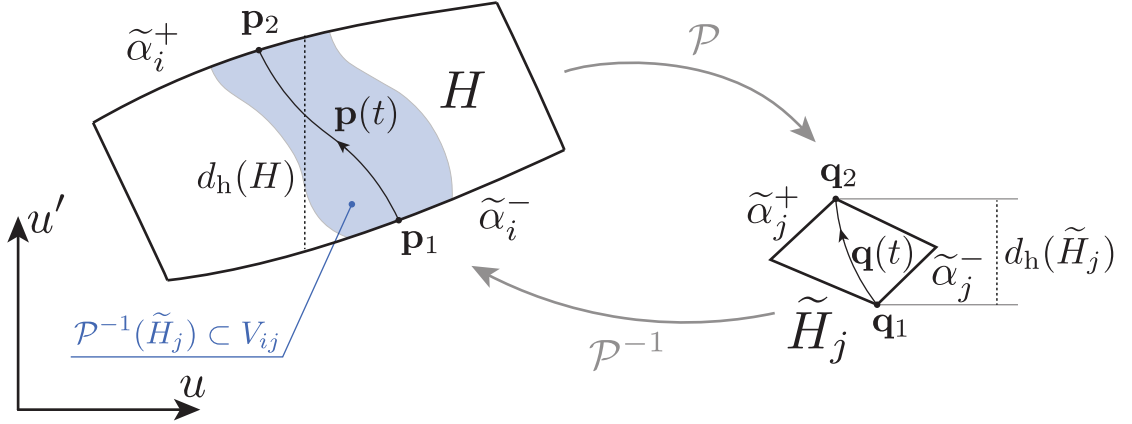


Figure C.3. Illustration to the proof of the point (ii) for the case when h-strip \tilde{H}_j is not well-measurable. Thickness of H and \tilde{H}_j are measured along the dotted lines. Pre-image of \tilde{H}_j strip is colored with gray.

If both h-strips H and \tilde{H}_j are not well-measurable then the two above mentioned technics should be combined together. The consideration of all other cases of the theorem is similar and the same reasoning can be applied with minor adjustments. Theorem is proved. \square

Theorem (On v-strips mapping). *Let Poincaré map \mathcal{P} and its inverse \mathcal{P}^{-1} be defined on a complete (see Definition 8) island set $\bigcup_{i \in S} D_i$, where S is a finite or countable set of indices. Let for all $i, j \in S$ the set $H_{ij} = \mathcal{P}(D_i) \cap D_j$ is non-empty, \mathcal{P}^{-1} is defined on a closure $\overline{H_{ij}}$, and one of the following two conditions holds:*

(1) *the borders β_j^\pm of an island D_j are increasing curves, $\forall \mathbf{q} \in \overline{H_{ij}}$ the signs of $\{b_{mn}\}$ in the matrix of the linear operator $D\mathcal{P}_{\mathbf{q}}^{-1} = (b_{mn})$ have exactly one of the following configurations:*

$$(a) (+ +), \quad (b) (- -), \quad (c) (+ -), \quad (d) (- +);$$

and at the same time the borders β_i^\pm of D_i are increasing curves for cases (a), (b), and decreasing curves for (c), (d);

(2) *the borders β_j^\pm of an island D_j are decreasing curves, $\forall \mathbf{q} \in \overline{H_{ij}}$ the signs of $\{b_{mn}\}$ in the matrix of the linear operator $D\mathcal{P}_{\mathbf{q}}^{-1} = (b_{mn})$ have exactly one of the following configurations:*

$$(a) (+ -), \quad (b) (- +), \quad (c) (+ -), \quad (d) (- +);$$

and at the same time borders β_i^\pm of D_i are decreasing curves for cases (a), (b), and increasing for (c), (d);

and moreover $\exists \nu > 1$ such that $\forall q \in \overline{H_{ij}}, |b_{22}| \geq \nu$. Then

- (i) *for any v-strip $V \in D_j$, $\mathcal{P}^{-1}(V) \cap D_i = \tilde{V}_i$ is also a v-strip;*
- (ii) *$d_v(\tilde{V}_i) \leq (1/\nu)d_v(V)$ (here $d_v(\cdot)$ is an v-strip thickness in a sence of Definition 11).*

Proof. Completely analogous to the proof of the h-strips mapping theorem. \square

Bibliography

1. *Pollack S. E., Dries D., Junker M., Chen Y. P., Corcovilos T. A., Hulet R. G.* Extreme Tunability of Interactions in a ${}^7\text{Li}$ Bose-Einstein Condensate // Phys. Rev. Lett. — 2009. — Mar. — Vol. 102, issue 9. — P. 090402.
2. *Chin C., Grimm R., Julienne P., Tiesinga E.* Feshbach resonances in ultracold gases // Rev. Mod. Phys. — 2010. — Apr. — Vol. 82, issue 2. — P. 1225–1286.
3. *Bauer D. M., Lettner M., Vo C., Rempe G., Dürr S.* Combination of a magnetic Feshbach resonance and an optical bound-to-bound transition // Phys. Rev. A. — 2009. — June. — Vol. 79, issue 6. — P. 062713.
4. *Hukriede J., Runde D., Kip D.* Fabrication and application of holographic Bragg gratings in lithium niobate channel waveguides. — 01/2003.
5. *Pachpatte B. G.* Inequalities for Differential and Integral Equations. Vol. 197. — Mathematics in Science, Engineering, 1998.
6. *Alfimov G. L., Zezyulin D. A.* Nonlinear modes for the Gross–Pitaevskii – a demonstrative computation approach // Nonlinearity. — 2007. — Vol. 20, no. 9. — P. 2075–2092.
7. *Alfimov G. L., Lebedev M. E.* On regular and singular solutions for equation $u_{xx} + Q(x)u + P(x)u^3$ // Ufa Mathematical Journal. — 2015. — Vol. 7, no. 2. — P. 3–16.
8. *Alfimov G. L., Avramenko A. I.* Coding of nonlinear states for the Gross–Pitaevskii equation with periodic potential // Physica D: Nonlinear Phenomena. — 2013. — Vol. 254. — P. 29–45. — ISSN 0167-2789.
9. *Guckenheimer J., Holmes P.* Nonlinear Oscillations, Dynamical Systems, and Bifurcations of Vector Fields. Vol. 42. — Springer-Verlag New York, 1983. — (Applied Mathematical Sciences).

10. Šil'nikov L. P. On a Poincaré–Birkhoff problem // Mathematics of the USSR-Sbornik. —.
11. Alekseev V. M. Final motions in the three-body problem and symbolic dynamics // Russian Mathematical Surveys. — 1981. — Aug. — Vol. 36, no. 4. — P. 181–200.
12. Alfimov G. L., Kizin P. P., Zezyulin D. A. Gap solitons for the repulsive Gross-Pitaevskii equation with periodic potential: Coding and method for computation // Discrete & Continuous Dynamical Systems - B. — 2017. — Vol. 22, no. 4. — P. 1207–1229.
13. Wiggins S. Introduction To Applied Nonlinear Dynamical Systems And Chaos. Vol. 4. — 2003. — ISBN 0-387-00177-8.
14. Arnold V. I. Ordinary Differential Equations. — Springer Berlin Heidelberg, 1992. — (Springer Textbook).
15. Yamazaki R., Taie S., Sugawa S., Takahashi Y. Submicron Spatial Modulation of an Interatomic Interaction in a Bose-Einstein Condensate // Phys. Rev. Lett. — 2010. — July. — Vol. 105, issue 5. — P. 050405.
16. Alfimov G. L., Konotop V. V., Salerno M. Matter solitons in Bose-Einstein condensates with optical lattices // Europhys. Lett. — 2002. — Vol. 58, no. 1. — P. 7–13.
17. Sakaguchi H., Malomed B. A. Matter-wave solitons in nonlinear optical lattices // Phys. Rev. E. — 2005. — Oct. — Vol. 72, issue 4. — P. 046610.
18. Lebedev M. E., Alfimov G. L., Malomed B. A. Stable dipole solitons and soliton complexes in the nonlinear Schrödinger equation with periodically modulated nonlinearity // Chaos. — 2016. — Vol. 26. — P. 073110.
19. Mayteevarunyoo T., Malomed B. A. Stability limits for gap solitons in a Bose-Einstein condensate trapped in a time-modulated optical lattice // Phys. Rev. A. — 2006. — Sept. — Vol. 74, issue 3. — P. 033616.

20. *Wang D. L., Yan X. H., Liu W. M.* Localized gap-soliton trains of Bose-Einstein condensates in an optical lattice // Phys. Rev. E. — 2008. — Aug. — Vol. 78, issue 2. — P. 026606.
21. *Mayteevarunyoo T., Malomed B., Baizakov B., Salerno M.* Matter-wave vortices and solitons in anisotropic optical lattices // Physica D: Nonlinear Phenomena. — 2009. — Vol. 238. — P. 1439–1448.
22. *Cuevas J., Malomed B. A., Kevrekidis P. G., Frantzeskakis D. J.* Solitons in quasi-one-dimensional Bose-Einstein condensates with competing dipolar and local interactions // Phys. Rev. A. — 2009. — May. — Vol. 79, issue 5. — P. 053608.
23. *Yang J.* Nonlinear Waves in Integrable and Nonintegrable Systems. — Philadelphia, SIAM, 2010. — (Mathematical modeling and computation).
24. *Trofimov V., Peskov N.* Comparison of finite-difference schemes for the Gross-Pitaevskii equation // Mathematical Modelling and Analysis. — 2009. — Mar. — Vol. 14. — P. 109–126.
25. *Sakaguchi H., Malomed B. A.* Solitons in combined linear and nonlinear lattice potentials // Phys. Rev. A. — 2010. — Jan. — Vol. 81, issue 1. — P. 013624.
26. *D'Agosta R., Malomed B. A., Presilla C.* Stationary states of Bose-Einstein condensates in single- and multi-well trapping potentials // Laser Physics. — 2002. — Vol. 12. — P. 37–42.
27. *D'Agosta R., Presilla C.* States without a linear counterpart in Bose-Einstein condensates // Phys. Rev. A. — 2002. — Mar. — Vol. 65, issue 4. — P. 043609.
28. *Zezyulin D. A., Alfimov G. L., Konotop V. V., Perez-Garcia V. M.* Control of nonlinear modes by scattering-length management in Bose-Einstein condensates // Phys. Rev. A. — 2007. — July. — Vol. 76, issue 1. — P. 013621.

29. *Zezyulin D. A., Alfimov G. L., Konotop V. V., Perez-Garcia V. M.* Stability of excited states of a Bose-Einstein condensate in an anharmonic trap // Phys. Rev. A. — 2008. — July. — Vol. 78, issue 1. — P. 013606.
30. *Abdullaev F. K., Caputo J. G., Kraenkel R. A., Malomed B. A.* Controlling collapse in Bose-Einstein condensates by temporal modulation of the scattering length // Phys. Rev. A. — 2003. — Jan. — Vol. 67, issue 1. — P. 013605.
31. *Alfimov G. L., Gegel L. A., Lebedev M. E., Malomed B. A., Zezyulin D. A.* Localized modes in the Gross-Pitaevskii equation with a parabolic trapping potential and a nonlinear lattice pseudopotential // Communications in Nonlinear Science and Numerical Simulation. — 2019. — Vol. 66. — P. 194–207. — ISSN 1007-5704.
32. *Hartman P.* Ordinary Differential Equations. — New York: John Wiley, Sons, 1964.
33. *Coppel W. A.* Stability and Asymptotic Behaviour of Differential Equations. — Boston: Heath, Co., 1965.